Quantum emitters in diamond and nitrides semiconductors

by

Yanzhao Guo

A Thesis submitted to Cardiff University
for the degree of Doctor of Philosophy

October 22 2024

Abstract

Quantum emitters in semiconductors are important candidates for the realization of quantum technology. Their discrete internal energy levels are the natural hosts for holding quantum information. For example, the single photon generation from these quantum emitters is the important building block for quantum photonics circuits. Additionally, spin-based quantum sensing paves a promising way to high-sensitivity and high-resolution sensing in real-life applications. However, due to the complex coupling to the solid-state environment, it is still a challenge to fabricate quantum emitters with both excellent optical and spin coherence properties. One solution is to use the photonics structures and advanced fabrication to improve these properties of the well-understood quantum emitters, such as negatively charged nitrogen-vacancy centres. Another path is to keep looking for and identifying novel quantum emitters with superior properties in semiconductors with better growth processes and commercial availability.

In this thesis, I introduced the basic knowledge of quantum information and reviewed the recent progress on quantum emitters in semiconductors in chapter 1, described experimental method used in this thesis in Chapter 2. Chapters 3-7 are the research chapters. I investigated the laser-written waveguide-integrated negatively charged nitrogen-vacancy centres with excellent spin coherence properties in diamond in Chapter 3, developed an enhanced quantum sensor based on a laser-written integrated photonic diamond chip in Chapter 4. I demonstrated the photodynamics between multiple internal energy levels of quantum emitters in aluminium nitrides in Chapter 5. I reported the germanium-related and iron-related quantum emitters in free-standing gallium nitrides in Chapter 6, and fabricated the quantum emitters in gallium nitrides via laser writing in Chapter 7. The studies listed in this thesis would expand knowledge of quantum emitters in semiconductors and improve the understanding of the quantum technology based on the quantum emitters in semiconductors.

Publications

First author publications

Yanzhao Guo, John P. Hadden, Federico Gorrini, Giulio Coccia, Vibhav Bharadwaj, Vinaya Kumar Kavatamane, Mohammad Sahnawaz Alam, Roberta Ramponi, Paul E. Barclay, Andrea Chiappini, Maurizio Ferrari, Alexander Kubanek, Angelo Bifone, Shane M. Eaton, and Anthony J. Bennett*. Laser-written waveguide-integrated coherent spins in diamond, APL Photonics 9, 076103 (2024).

Yanzhao Guo, John P. Hadden, Rachel N. Clark, Samuel G. Bishop, and Anthony J. Bennett*. Emission dynamics of optically driven aluminum nitride quantum emitters, Physical Review B 110, 014109 (2024).

Yanzhao Guo*, Giulio Coccia, Vinaya Kumar Kavatamane, Argyro N. Giakoumaki, Anton N. Vetlugin, Roberta Ramponi, Cesare Soci, Paul E. Barclay, John P. Hadden, Anthony J. Bennett*, and Shane M. Eaton. Enhanced quantum magnetometry with a laser-written integrated photonic diamond chip, arXiv:2502.02478.

Co-author publications

M Sahnawaz Alam*, Federico Gorrini*, Michał Gawełczyk*, Daniel Wigger, Giulio Coccia, Yanzhao Guo, Sajedeh Shahbazi, Vibhav Bharadwaj, Alexander Kubanek, Roberta Ramponi, Paul E Barclay, Anthony J Bennett, John P Hadden, Angelo Bifone, Shane M Eaton, Paweł Machnikowski. Determining strain components in a diamond waveguide from zero-field optically detected magnetic resonance spectra of negatively charged nitrogen-vacancy-center ensembles, Physical Review Applied, 22(2), 024055 (2024).

Contents

List of Tables

List of Figures

"Thanks all! I made it!"

Acknowledgements

Funding Bodies and Affiliations

YanzhaoGuo acknowledges the financial support provided by EPSRC via Grant No. EP/T017813/1 and EP/03982X/1 and the European Union's H2020 Marie Curie ITN project LasIonDef (GA No. 956387).

Personal Thanks

This three-year PhD journey is an unforgettable memory in my whole life. There are so many thanks to the people around me. In particular, I want to thank my main supervisor Anthony J Bennett for your kind patience, support, brilliant leadership, and lots of help. I also want to thank my co-supervisor John P Hadden who always gives me thoughtful advice, close help and a positive attitude to academic and non-academic things. Special thanks must go to Shane Eadton who is the amazing coordinator of the Laslondef project, and also an important and reliable collaborator on laser fabrication during my PhD. I can not get my PhD done without all your help and support.

I really appreciate every colleague and collaborator I have met in the last three years. Thanks to the members of the QLab, Petros Androvitsaneas, Sherif Ibrahim, Sam Bishop, Reza Hekmati, Rachel Clark, Annie Mathew, Cobi Maynard, Joseph Cannon, Matthew Jordan, Bilge Yagci, Davey Armstrong, Miguel Alvarez Perez, Katie Eggleton, Demininggus Pekei and Olivia Kiely. It's a pleasure to work with you. I also want to thank the people at TRH for building this warm and nice workplace. They are Qiang Li (my unofficial mentor), Bo Hou, Zhao Yao, and Diyar Othman. I want to thank the staff in ICS who gave me lots of help in the clean room. The next thanks are to all the other early-stage researchers and team leaders in the European Union's Horizon 2020 Marie Skłodowska-Curie Actions LasIonDef project. It is a great honour to have the opportunity to work with you guys. Particularly, thanks to the groups at Politecnico di MILANO where I got my laser writing training and sample fabricated with Roberta Ramponi, Giulio Coccia, Vibhav Bharadwa, Argyro N. Giakoumaki, etc. Moreover, I thank the groups at Ulm University where I had a chance to use the cryostat to investigate the PL emission of quantum emitters at low temperature with Alexander Kubanek, Selene Sachero, Sajedeh Shahbazi, etc. Next thanks are extended to other collaborators at the University of Calgary (Vinaya Kumar Kavatamane and Paul E. Barclay), the University of Turin (Federico Gorrini and Angelo Bifone) and Nanyang Technological University (Anton N. Vetlugin and Cesare Soci) who inspired the interesting fabrications, characterizations and discussions on our published papers.

Last but not least, I want to thank my family and friends who gave me unconditional support, unwavering confidence and understanding. Might be one day you happen to read this.

Chapter 1

Introduction

This chapter will introduce the basic knowledge of quantum information, such as quantum computation, quantum sensing, and quantum information processing realization platforms. Particularly I will give a detailed review of quantum emitters in wide bandgap semiconductors such as diamond, hexagonal boron nitride, aluminum nitrides, and gallium nitrides which align with the topic of this thesis.

1.1 Quantum information

Quantum information is the study of the information processing tasks that can be accomplished using a quantum mechanical system[1]. This concept was introduced by Richard Feynman[2]. With years of development, it has led to many subjects for different quantum applications. In this thesis, I will briefly introduce three relevant subjects: quantum computation, quantum sensing, and quantum platform realization.

1.1.1 Quantum computation

From DiVincenzo's criteria, the quantum computer should be initialised, manipulated, and measured (readout), with coherence properties and scalability[3]. In analogy to the traditional computer, the initialisation is normally the first step of computing to initialize the system to pure initial states from the mixed states. Manipulation is the computation operation achieved via universal gates. The readout is the process of measuring the computation results. The scalability is the ability to expand the well-characterized bits. In contrast, quantum coherence is the unique merit of quantum

computation, which preserves the superposition and phase relationships between different quantum states. Compared to classical computation, for example, the superposition quantum state allows quantum parallelism, which could accelerate some computations such as Shor's Algorithm [4] for factoring large numbers.

Qubit and quantum state

The qubit is the simplest unit in quantum information programming[1]. The state of a qubit includes all the possible states in a two-energy level quantum system. In the mathematical demonstration, the quantum state of a qubit is in fact a vector in a 2-dimensional Hilbert space, such as

$$|\psi\rangle = \sin\frac{\theta}{2}|0\rangle + e^{i\varphi}\cos\frac{\theta}{2}|1\rangle, \tag{1.1}$$

where the $|1\rangle$ and $|0\rangle$ are basis vectors for the qubit, θ is the population information of qubit represented by qubit vector projection along quantization z-axis, and φ is the phase information of qubit relation to quantum state $|1\rangle$ and $|0\rangle$ respectively as shown in Fig. 1.1.

Bloch sphere and quantum logic gate

In Fig. 1.1, the north and south poles of the Bloch sphere correspond to the $|0\rangle$ and $|1\rangle$ eigenstates of two energy level systems, and the population information and phase information of the state are noted by the latitude and longitude of the Bloch sphere. The modulo (R) of the vector of the quantum state denotes the purity of a quantum state and provides insight into how much a quantum system deviates from a pure state due to decoherence or noise. In Fig. 1.1(a), every pure state in two energy levels could be represented by the vector which reaches the surface of the Bloch sphere with R=1. In contrast, for a mixed state, the modulo of the vector of the state R is less than 1 due to decay off-diagonal terms of the qubit density matrix from decoherence, as shown in Fig. 1.1(b). In analogy to logic gates in classical computers, to program a qubit, it is necessary to manipulate the quantum state of a qubit by the quantum gate. In mathematic concepts, quantum gates are a series of reversible unitary matrices in Hibbert space. A single qubit gate can be represented visually in the Bloch sphere. Fig. 1.2 illustrates three single-qubit gate operations in the Bloch sphere, including the Hadamard gate H in Fig. 1.2(a), Pauli-X in Fig. 1.2(b), and Phase shift $R_z(\theta)$ gate in Fig. 1.2(b). Additionally, other two rotation gates along the x-axis $R_x(\theta)$, and y-axis $R_y(\theta)$ are given by[1]

$$R_x(\theta) \equiv e^{\frac{i\theta\sigma_x}{2}} = \begin{pmatrix} \cos\frac{\theta}{2} & -i\sin\frac{\theta}{2} \\ -i\sin\frac{\theta}{2} & \cos\frac{\theta}{2} \end{pmatrix}, \tag{1.2}$$

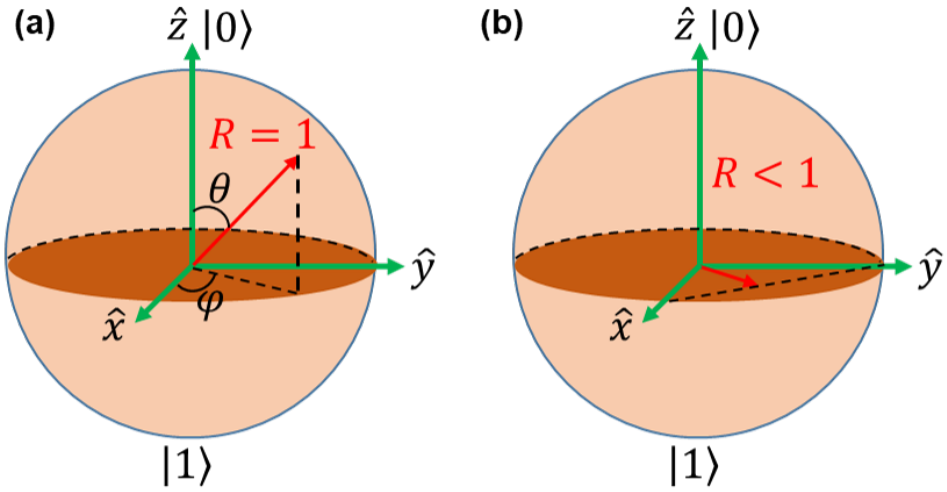

Figure 1.1. The single qubit representation in Bloch sphere (a) pure state (b) mixed state.

$$R_y(\theta) \equiv e^{\frac{i\theta\sigma_y}{2}} = \begin{pmatrix} \cos\frac{\theta}{2} & -\sin\frac{\theta}{2} \\ -\sin\frac{\theta}{2} & \cos\frac{\theta}{2} \end{pmatrix}. \tag{1.3}$$

The two-qubit gate is another element in quantum computing. Fig. 1.3 shows two common two-qubit gates: controlled-NOT(CNOT) gate and SWAP gate. In Fig. 1.3(a), the CNOT gate could be used to realize the entanglement state preparation: the first qubit state (encoded in the first 2 columns) determines if the second qubit (encoded in the last 2 columns) is or is not rotated by the π pulse. If the system state was the superposition state $\frac{1}{\sqrt{2}}(|00\rangle + |10\rangle)$, after a CNOT gate operation the system would evolve to $\frac{1}{\sqrt{2}}(|00\rangle + |11\rangle)$ which is the maximum entanglement state in the two-qubit system. In Fig. 1.3(b), SWAP could realize the quantum state switch between the two qubits.

In general, single-qubit gates could prepare the single-qubit in any arbitrary quantum state. And two-qubit gates introduce interactions between qubits, allowing for entanglement. Thus, in quantum information theory, the combination of single-qubit gates and two-qubit gates could prepare the quantum system into any target state[5].

Decoherence mechanisms

As mentioned earlier, quantum coherence is the phase relationship between the different components in the superposition state of the quantum system, which is the fundamental requirement in quantum computing[1]. However, since the completely isolated system doesn't exist[6], inevitably, the coupling between the ambient environment and the quantum system results in the uncontrollable evolution of the quantum state: decoherence. This decoherence process would describe how a quantum state

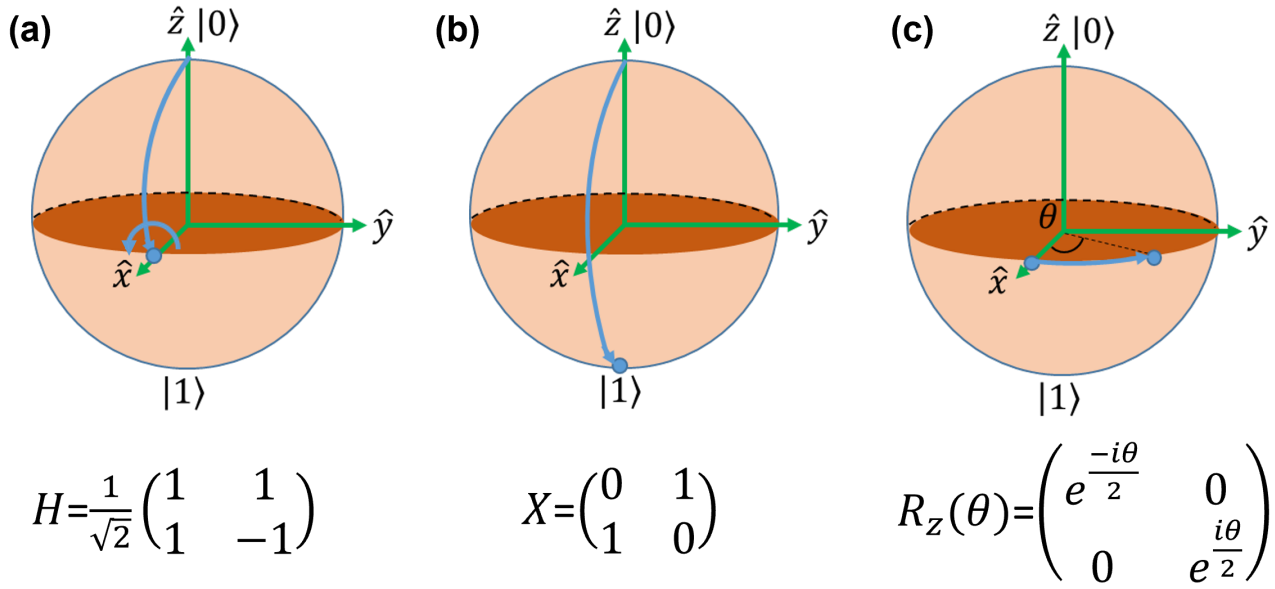

Figure 1.2. The single qubit gate. (a) Hadamard gate H corresponds $\pi/2$ rotation along the y axis and followed π rotation along x axis. (b) Pauli-X gate corresponds π rotation along the Y axis. And (c) Phase shift gate $R_z(\theta)$ corresponds θ rotation along the z-axis.

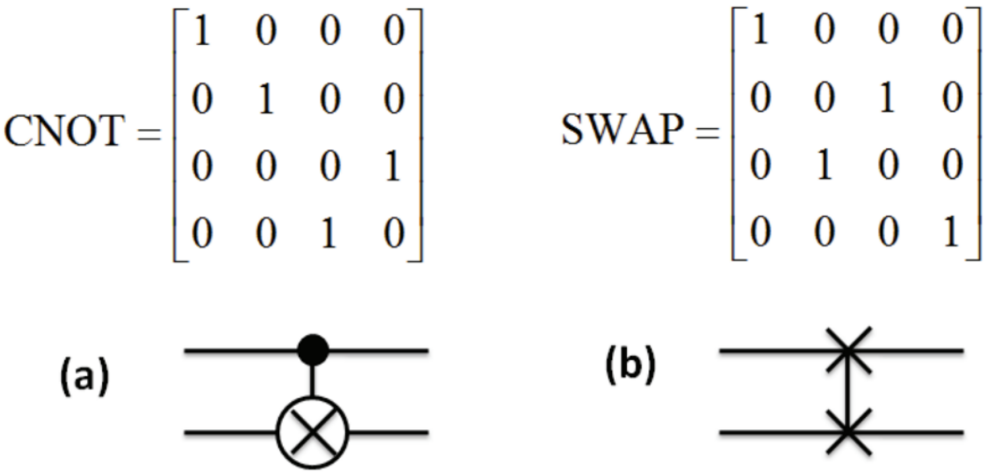

Figure 1.3. The matrix and quantum circuit representation of two-qubit gate (a) CNOT gate (b) SWAP gate, where columns of 1 and 2 show components in qubit1, and columns of 3 and 4 are for qubit2.

transitions from a coherent superposition to a classical system. On the other hand, current quantum operations are inevitably processed with noise. The noise could originate from the imperfect quantum gate, uncontrollable hardware errors, or fluctuations in experimental parameters. These random and unwanted noises would introduce errors in quantum computation. Eventually, the noise would contribute to the decoherence process, leaking coherent quantum information to the classical system. Therefore, currently, on the quantum computing side[7], the main challenge is to find a quantum system with ultra-long coherence time and high-speed and high-fidelity operation. The key is to achieve fault-tolerant quantum computing to protect quantum information against noise. First of all, coherence properties should be good enough to perform the required quantum gate operations before decoherence occurs. Specifically, longitudinal relaxation times T_1, which represent the coherence time to preserve the population information, the phase decoherence time T_2 for storing phase information, and the inhomogeneous dephasing time T_2^*, which is sensitivity to external static signal fields. The full introduction and measurement protocol for these coherence times is detailed in the section 2.3.2 with the negatively charged nitrogen vacancy centres in diamond as an example. Here, I will take the most progressing quantum platform superconductor circuit as an example to give a clear idea about the requirements for fault-tolerant quantum computing. Specificity, T_2 are expected to be over $1\,\mathrm{ms}$, the single qubit quantum gates are expected to be less than $10\,\mathrm{ns}$ with over 99.99% fidelity, the two-qubit quantum gates is less than $100\,\mathrm{ns}$ with over 99.9% fidelity [8, 9].

1.1.2 Quantum sensing

Quantum sensing is the use of a quantum system, properties, or quantum phenomenon to perform a measurement of a physical quantity (classical or quantum)[10]. Quantum sensing focuses on the central weakness of quantum systems, their susceptibility to external influences. Compared to the classical, quantum systems are increasingly investigated at the single-atom level, and entanglement is used as a resource for increasing the sensitivity. Specifically, the entanglement-enhanced quantum sensing could suppress the standard quantum limit (or decrease the statistical error) or shot noise limit to, potentially, achieve the Heisenberg limit[11, 12]. A detailed discussion of sensitivity is placed in the below sensitivity subsection.

In 2017, Degen et al. concluded the definition of quantum sensing and quantum sensors. In analogy to the DiVincenzo criteria for quantum computation[3], the quantum sensor is expected to exhibit discrete energy levels, such as the simple two-energy level as shown in Fig. 1.4, which can be initialised, manipulated and read out. Moreover, as a sensor, its quantum system should be able to interact with a relevant physical quantity, such as a magnetic field or temperature. The interaction or transduction parameter between external physical quantity and the quantum system of the sensor is highly dependent on the experiment realization[13]. For example, the spin-based sensor

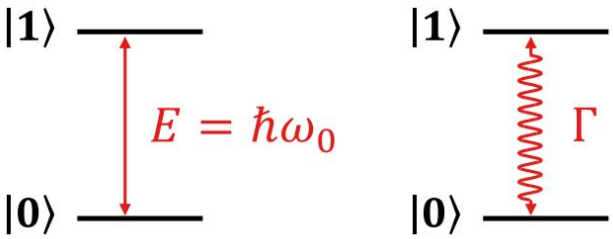

Figure 1.4. A two-state quantum system which consists of a lower energy state $|0\rangle$ and a higher energy state $|1\rangle$. The external signal V will affect its transition frequency ω_0 and transition rate Γ[10].

will respond to the magnetic fields because of the Zeeman effect.

Quantum sensing protocol

Quantum sensing experiments typically follow a generic quantum coherent control sequence of sensor initialisation, interaction with the physical quantity, sensor readout, and signal estimation. Then the quantum sensor can be demonstrated by the Hamiltonian[10]:

$$H(t) = H_{Internal} + H_V(t) + H_{control}(t). \tag{1.4}$$

The $H_{Internal}$ is the internal Hamiltonian of the quantum sensor, $H_V(t)$ is the Hamiltonian associated with an external signal $V(t)$, and $H_{control}(t)$ is the control Hamiltonian which can be intentionally designed to manipulate or tune the quantum sensor in a controlled manner. The target of quantum sensing is to measure $V(t)$ from the interaction with the quantum sensor via its Hamiltonian $H_V(t)$, usually by a tailored $H_{control}(t)$.

For example, the Ramsey interference protocol is the typical way to measure the static energy splitting ω_0 in the quantum system. The sequence is detailed below.

(1) The quantum sensor is initialised into a known basis state $|0\rangle$. (2) A $\pi/2$ pulse is used to prepare the quantum sensor into the superposition state

$$|\psi_0\rangle = \frac{1}{\sqrt{2}}(|0\rangle + |1\rangle) \tag{1.5}$$

(3) After an evolution time t, a phase $\phi = \omega_0 t$ containing the static energy splitting is accumulated in this superposition state.

$$|\psi(t)\rangle = \frac{1}{\sqrt{2}}(|0\rangle + e^{i\omega_0 t}|1\rangle), \tag{1.6}$$

(4) A second $\pi/2$ pulse is used to convert the phase information of the state $|\psi(t)\rangle$ to the measurable

population information.

$$|\alpha\rangle = \frac{1}{2}(1 + e^{i\omega_0 t})\,|0\rangle + \frac{1}{2}(1 - e^{i\omega_0 t})\,|1\rangle\,. \tag{1.7}$$

(5) The population information of the state is read out by calculating the transition probability

$$p = 1 - |\langle 0|\alpha\rangle|^2 = \sin^2(\omega/2) = \frac{1}{2}[1 - \cos(\omega_0 t)]. \tag{1.8}$$

Ramsey fringes with an oscillation frequency ω_0 are recorded p as a function of time t. Thus, the energy splitting ω_0 can be directly extracted by the Ramsey measurement.

Sensitivity

Sensitivity η is the signal magnitude that yields a unit signal-to-noise ratio (SNR), suggesting the minimal detectable physical quantity per unit time for the quantum sensor[10, 14]. Experimental detection of the transition probability p in equation 1.8 will inevitably exhibit a nonzero error σ_p resulting in an error for the signal estimation. To calculate sensitivity, it is therefore important to analyze the noise sources for σ_p.

The first noise is from the quantum projection noise which represents the most fundamental limit of uncertainty in quantum sensing. This is because the projective readout can not directly provide the fractional probability. To estimate p, the experiment has to be repeated N times to obtain the fractional probability[10]. The second noise source is the decoherence and relaxation of the quantum sensor, resulting in a reduction of the observed probability δp with increasing sensing time[14, 15]. This is a key performance metric of the qubit, shaped by the noise process, as it limits the maximum evolution time t that can be used for sensing. The third part is the imperfect initialisation and manipulation in the quantum sensing protocol. Errors in the manipulation can produce multiple effects, but they typically result in a decrease in δp[10]. On the other hand, the optimal initialisation and manipulation would greatly save the sensing protocol overhead time and enhance the sensitivity. The last noise source is the classical readout noise. There are two different readout regimes. In the single-shot readout regime, the classical noise added during the readout process is small[15]. It depends on the specific readout fidelity and selection criteria of the threshold value. The second averaged readout regime features the inefficiency of quantum state readout, resulting in the lowest readout fidelity and becoming the primary source of error[16]. Thus, the sensitivity is inherently defined by its quantum projection limitation, quantum dephasing time and readout fidelity.

1.1.3 Quantum information processing platform

With consistent and tremendous efforts, a few quantum information processing platform systems have been developed, such as atoms[17, 18, 19, 20, 21], ions[22], photons[23], spins[24], or a superconductivity circuit[25, 26] system. The different quantum realization approaches exhibit distinct advantages on the specific quantum application. For example, a superconductor circuit shows its promising future for computation with a larger number of qubits due to its excellent scalability[25, 23, 26]. Moreover, spins in semiconductors are a very promising nanoprobe[27] and quantum register due to their high coherence time at room temperature[24]. The photon is the optimum platform for quantum communication due to its ability to transmit quantum information over long distances[28, 29].

Overall, it's still hard to predict which platform would be the top candidate in computation, sensing, or network. The future quantum system is also expected to be connected with different quantum platforms[30]. In this distributed quantum system, any task can be divided into a series of small tasks dispensed to different preferred platforms.

1.2 Quantum emitters in semiconductors

In this thesis, I will focus on quantum emitters (QEs) in wide bandgap semiconductors which are leading candidates for room-temperature quantum information processing platforms. Most QEs exhibit single-photon emission at room temperature, and some of them feature excellent optical and spin coherence properties, which is crucial for quantum networks and quantum sensing. For example, the negatively charged nitrogen-vacancy centre in diamond is the most understood QE, which is a very promising sensor with nanoscale resolution and outstanding sensitivity. Meanwhile, it is important to discover, identify and reproduce the new QEs with analogous or superior properties in material systems with well-established growth or commercial availability such as nitride semiconductors. In this section, I will give a review of the recent progress on the QEs in diamond and nitride semiconductors as the background for further research chapters.

1.2.1 Quantum emitters in diamond

Diamond is a wide bandgap ($5.5\,\mathrm{eV}$) semiconductor hosting hundreds of different emitters[31]. These emitters are the trap centres capturing the electrons leading to poor electrical performance[32], however, exhibiting favourable photoluminescence (PL) emission for quantum

applications. In this section, I will introduce two groups of QEs, negatively charged nitrogen-vacancy centres and negatively charged group IV centres, with attractive properties for quantum applications.

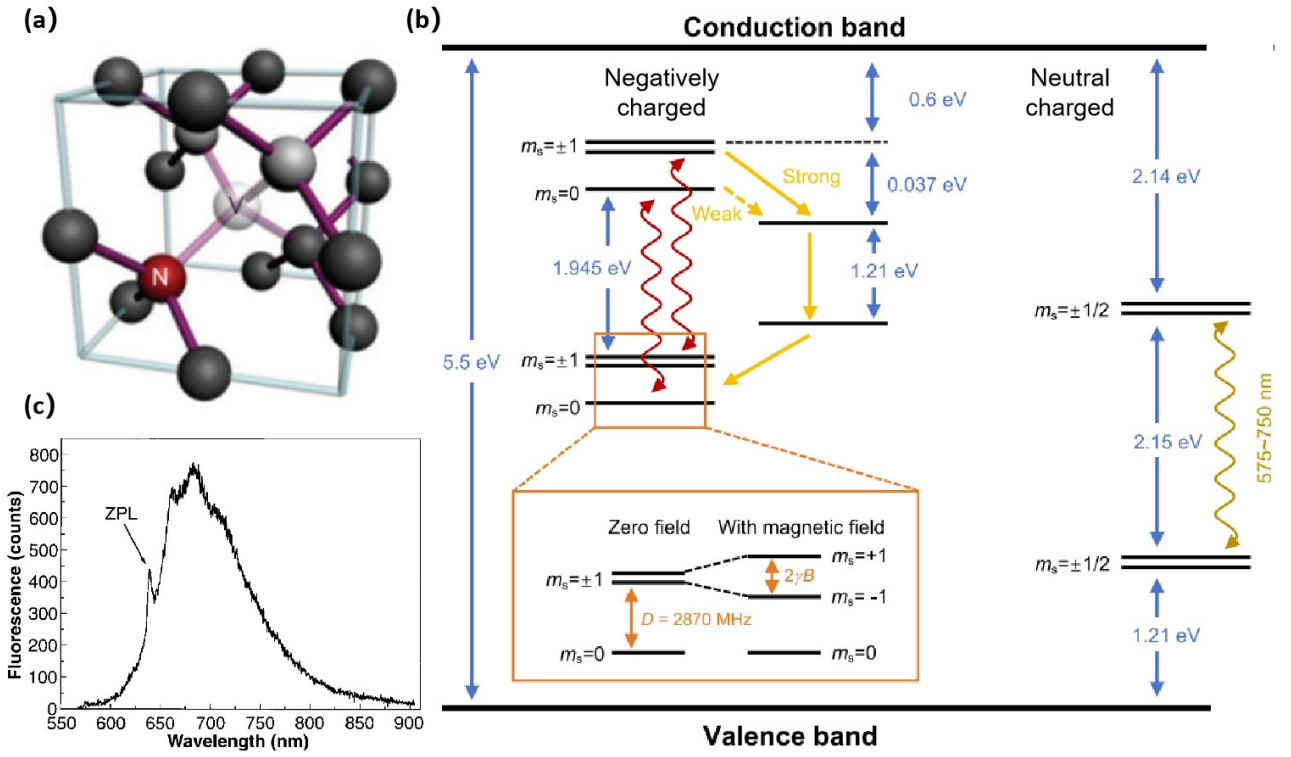

Figure 1.5. The background of NV (a) Atomic structure of NVs[14]. (b) The energy level of NVs[13]. (c) PL emission of NVs from[15].

Since 1997 the discovery of optically detected magnetic resonance (ODMR) on negatively charged nitrogen-vacancy centres[33], it has become a rapidly growing field. Researchers have investigated its detailed energy structure, developed a mature quantum control protocol, and improved its material processing in the last 27 years[15, 13, 14].

Negatively charged nitrogen-vacancy centres consist of a substitutional nitrogen atom paired with a nearby lattice vacancy that captures an electron as shown in Fig. 1.5(a). Meanwhile, the negatively charged nitrogen-vacancy centre could be converted to a neutrally charged state by losing an electron. Their energy structures are detailed in Fig. 1.5. Since the negatively charged nitrogen-vacancy centre is the most important target in this thesis, I will refer to the negatively charged nitrogen-vacancy centre as NV and the neutrally charged nitrogen-vacancy centre as NV^0. The NVs feature the C_{3v} symmetry with the diamond <111> axis as the quantization axis. Due to its asymmetric atomic structure[34], NVs are highly sensitive to weak external influences like temperature[35], pressure[36, 37], electric field[38] and magnetic field [14, 39]. As shown in Fig. 1.5(b), the NV is an $S = 1$ electron spin with triple ground and excitation states. The Hamiltonian of the ground state for NVs is given by[13],

$$
\begin{aligned}
H = & \underbrace{DS_z^2 + \gamma_{NV}\, \boldsymbol{B} \cdot \boldsymbol{S}}_{H_0} \\
& + \underbrace{A_{\parallel} S_z I_{z,N} + A_{\perp}(S_x I_{x,N} + S_y I_{z,N}) + Q_N I_Z^2 - \gamma_N (B_0 \cdot I_N)}_{H_{Nuclear}} \\
& + \underbrace{d_{\parallel}(E_Z + \delta_z)(S_z^2 - 2/3) + d_{\perp}(E_x + \delta_x)(S_y^2 - S_x^2) + d_{\perp}(E_y + \delta)(S_x S_y + S_y S_x)}_{H_{Strain|Electical}}
\end{aligned}
\tag{1.9}
$$

The first part is H_0 including the axial zero-field splitting parameter, $D \sim 2.87\,\mathrm{GHz}$, from the spin-spin interaction and Zeeman splitting $\gamma_{NV}\, \boldsymbol{B} \cdot \boldsymbol{S}$ from the interaction between the electron spin and external magnetic field $\boldsymbol{B}$. The $\gamma_{NV} \sim 28.04\,\mathrm{GHz/T}$ is the gyromagnetic ratio of the NV electron spin. The second part is the interaction between the NV electron spin and nitrogen nuclear spins (I_N=1 for ^{14}N, and I_N=1 for ^{15}N). The $A_{\parallel}$ and $A_{\perp}$ are the axial and transverse magnetic hyperfine coupling coefficients, respectively. The Q_N represents the nuclear electric quadrupole coupling. The γ_N denotes the gyromagnetic ratio of the respective nitrogen nuclear isotope. The third part indicates the strain and electric field interaction. The $d_{\parallel}$ and $d_{\perp}$ represent the ground-state components of the electric dipole moment. $S = (S_x, S_y, S_z)$ is the NV spin operator, $I_N = (I_{x,N}, I_{y,N}, I_{z,N})$ is the nitrogen nuclear spin operator, $E = (E_x, E_y, E_z)$ is the electrical field vector, $\delta = (\delta_x, \delta_y, \delta_z)$ is the strain field vector[13].

Due to its spin selective transition, the triplet ground state can be initialised to the preferred ground state $m_s = 0$ via a $532\,\mathrm{nm}$ green pump. Meanwhile, the original ground state could be read out by detecting its PL emission. As shown in Fig. 1.5(c), NVs feature a weak zero phonon line (ZPL) at $637\,\mathrm{nm}$ with a broad phonon sideband (PSB) emission extending to $800\,\mathrm{nm}$ at room temperature. This low ratio of the ZPL intensity and that of the total emission indicates a low Debye-Waller (DW) factor of ∼4%. The detailed ODMR protocol will be discussed in 2.3.2.

The long spin coherence time at room temperature allows NVs to measure this local environment with high sensitivity. Another benefit is that NVs as a sub-nanoscale defect could be probed at the nanoscale. However, due to the optical diffraction limitation, the NVs couldn't be directly used for nanosensing with conventional confocal microscopy. Therefore, it is an important topic to integrate the NVs into a scanning configuration with nanometre resolution, such as atomic force microscopy (AFM). One solution is demonstrated in Fig. 1.6 (a)[27]. A scanning beam with a single NV-integrated nanopillar is used as a nanotip in AFM to realise high sensitivity and high-resolution sensing. Compared to the complex nanofabrication for nanopillar, another commercial solution is simply attaching the nanodiamond containing the NVs on the tip of AFM as shown in Fig. 1.6(b). In both cases, the main challenge is that the spin transverse relaxation time (T_2) of NVs is

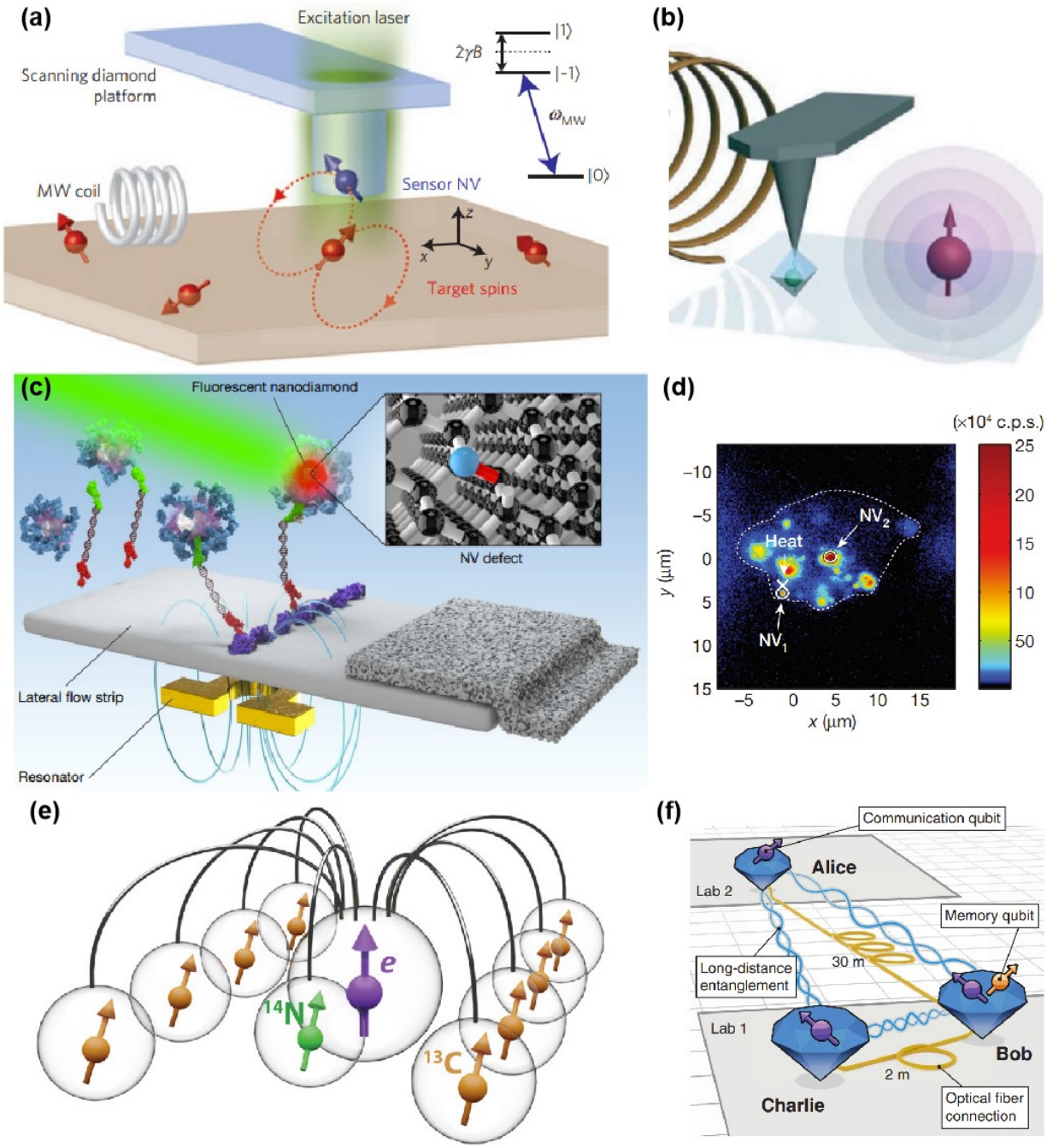

Figure 1.6. Quantum applications based on NVs. (a) High-resolution sensing with a single NV integration in a nanopillar[27]. (b) Nanodiamond attached on AFM tip as a nano-probe[39]. (c) Illustration of the concept of using fluorescent nanodiamonds in lateral flow assays for virus detection [40]. (d) Temperature sensing via nanodiamonds in a living cell[41]. (e) Ten qubit quantum register with NVs and its coupling nuclear spins[24]. (f) Realization of a multinode quantum network of remote solid-state qubits[42].

limited to a few μs due to the electric noise and strain during the fabrication. Another important field is to use NVs in nanodiamond as a non-invasive nano-probe, especially in a biological system. The nanodiamond could easily be functionalized with an intermediate targeted precursor which can transfer various biological signals to the magnetic field or electric field[43]. Basically, biological systems, such as cells and viruses, show weak interaction with NVs system but could be active with the intermediate precursor coated on the nanodiamond surface for magnetic field or electric field signal transformation[44, 45, 46, 47]. In this case, nanodiamonds with low cost could easily in vitro probe the target objective. For example, as shown in Fig. 1.6(c)[40], nanodiamonds are used as the ultrasensitive fluorescent labels in paper microfluidic lateral flow assays for in vitro diagnostics[40]. Moreover, thanks to the bio-compatibility of nanodiamonds, intercell sensing is also achieved by putting nanodiamonds in a living cell, for example, in vivo temperature sensing in Fig. 1.6. Overall, NVs-based sensing is a promising and huge topic and still a growing field. The completed introduction can be found in these review papers [15, 14].

NV electron spin and its coupled nuclear spins in diamonds provide promising qubits for quantum-information processing and quantum networks. However, due to inevitable cross-talk noise and decoherence during the quantum operation, NV-based quantum computing is implemented with limited qubits. In 2008, maximally entangled states such as the Greenberger-Horne-Zeilinger states were achieved in NV electron spin and two couplings nuclear spin [48]. In 2019, the progress on novel decoherence-protected gates extended the number of Qubit to 10, containing an NV electron spin and 9 coupling nuclear spins as shown in Fig. 1.6(e)[24]. This multiple-qubit register exhibits quantum memory for up to one minute. Combining the demonstrated long-range optical entanglement, this quantum register provides a way for the realization of node quantum networks. These quantum network nodes should feature the communication qubits (NVs) efficiently interfaced with optical photons, the local processing qubits (nuclear spins) manipulated with a high fidelity and coherence time, and the memory qubits (nuclear spins) storing the quantum information for quantum error correction, which also employs a quantum repeater for releasing communication qubit in the multiple-node networks. The two-node quantum network was achieved by Hanson's group in 2017, which realized entanglement distillation on a quantum network primitive of distant electron-nuclear two-qubit nodes.[49]. They established the three-node quantum network in 2022[42], as shown in Fig. 1.6(f). There is a NV electronic spin as a communication qubit in each node. An additional nuclear spin as memory qubit is in the middle node which allows the swap of the entangled state between two interconnect nodes to the long-lived nuclear spin. In this case, a distributing three-partite GHZ state across the three nodes can be achieved. The completed introduction to diamond-based quantum communication can be found in these reference papers[49, 50, 28, 51].

Another interesting type of QEs in diamond is negatively charged group IV QEs, including the silicon-vacancy centre (SiV), germanium-vacancy (GeV), tin-vacancy (SnV), and lead-vacancy

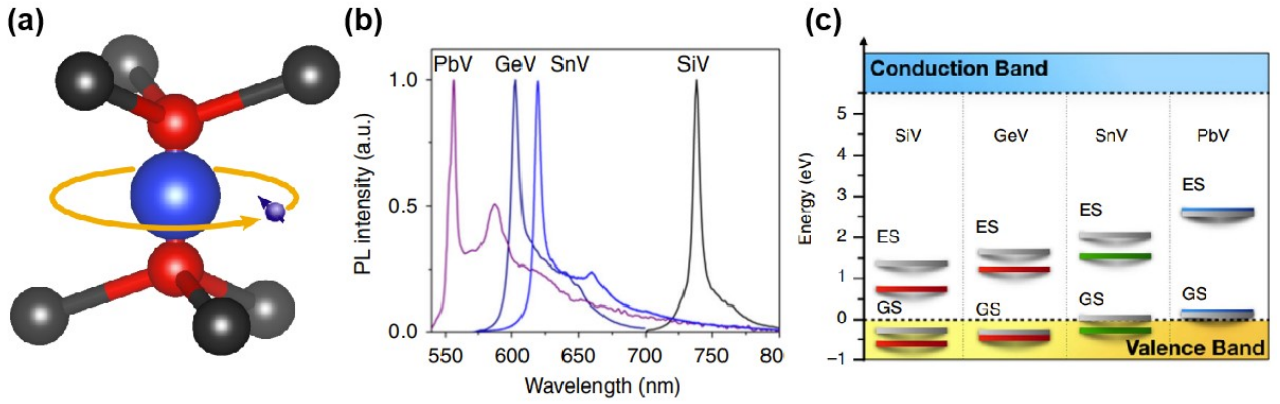

Figure 1.7. Diagram of a group-IV QEs (a) Atomic structure, where the blue group-IV dopant (blue) at a split-vacancy position in the diamond lattice (carbon atoms shown in black, vacancies in red) from [53]. (b) and (c) are the energy structures and PL spectra for group IV QEs of SiV, GeV, SnV, and PbV from [54].

(PbV). As shown in Fig. 1.7(a), the group IV QEs composed of a group IV dopant lying between two nearest-neighbours missing carbon atoms in the diamond lattice. Compared to the NVs, their inversion symmetry atomic structure protects the optical transition from local electric field fluctuations, resulting in lifetime-broadened optical emission. Another superior optical property is the high WD factor of group IV QEs as shown in Fig. 1.7(b), enhancing the coherence of emitted photons for quantum communication. These superior optical properties would lead to better photon throughput which is crucial for the quantum repeater application. As shown in Fig. 1.7(c), group IV QEs normally exhibit four energy levels. Due to the strong phonon coupling, the energy gap in the ground state determines the spin coherence time which is much shorter than NVs at room temperature. In this case, the most interesting study with group IV QEs is at cryogenic temperatures. The strained environment might increase the energy gap in the ground state, reduce the phonon coupling, and raise the quantum operation temperature[52, 53].

As mentioned before, for any quantum application based on QEs in diamond, it is a significant task to enhance its optical properties and protect its spin coherent properties. It is instructive to integrate the QEs photonics devices to improve optical properties. The conventional fabrication methods for photonics structure, such as ion implantation, and electron irradiation will inevitably degrade the coherence properties of QEs. To make my contribution to the diamond community, in this thesis, I investigated single and ensemble levels of highly coherent NVs in waveguides via laser writing in chapter 3 and chapter 4.

1.2.2 Quantum emitters in hexagonal boron nitride

Among the nitride semiconductors, hexagonal boron nitride (hBN) is the first extensively studied material for hosting the QEs[55]. It is also a (two-dimensional) 2D material that has been found to host the room-temperature single-photon QEs. In 2016, room-temperature single-photon QEs were observed in hBN. These QEs exhibit polarised and ultrabright PL rate of $4\,\mathrm{MHz}$ and high DW factor (84%) under continuous-wave (CW) $532\,\mathrm{nm}$ laser excitation as demonstrated in Fig. 1.8(a-b). hBN as a 2D material could be easily transferred to various photonics devices, paving the way for the realization of the integrated quantum photonic circuit. Then, a variety of QEs in hBN was found in the following few years[56]. Moreover, these outstanding optical properties allow the resonant excitation of the QEs, which is crucial to realising the optical control of QEs for quantum processing[57]. In 2018, spectral line widths of QEs in hBN were observed narrower than 1 GHz while the emitter experienced spectral diffusion[58] as illustrated in Fig. 1.8(c). In 2020[59], some groups observed the Fourier transform limited lines in photoluminescence excitation (sub-100-MHz linewidths) from 3 to 300 K as shown in Fig. 1.8(d). The Fourier transform (FT) limited lines are achieved by suppressing all the incoherent processes with interaction with the environment. The researcher claims that the centre's decoupling from phonons is a fundamental consequence of the material's low dimensionality[59]. Although theoretical work indicates these QEs could be carbon-related defects, the full nature of these QEs remains under debate. The future study should focus on combining the theoretical prediction, experimental properties, and fabrication reproduction of QEs together to test and identify exact the structure of these QEs. The identification of these QEs would also help to address the charge induced blinking of PL spectrum to obtain stable QEs.

Until 2019, researchers identified the negatively charged boron vacancy (V_B) in hBN and discovered its ODMR signal, and then extensive studies followed. As shown in Fig. 1.9(a), V_B consists of boron vacancy and captured electron. In Fig. 1.9(b), the magnetic field-dependent ODMR suggests V_B is the $S = 1$ electron spin with axial zero-field splitting parameter D of $3.48\,\mathrm{GHz}$. The hyperfine structure shown in Fig. 1.9 confirms its nature is V_B with $2nI + 1 = 7$ nuclear hyperfine transitions. Based on its experiment results and theoretical results, researchers predict V_B as an $S = 1$ electron spin like NVs exhibiting the triplet ground state and excitation state. Similarly, the spin selective relaxation explains the ODMR contracts in the ground state. V_B also exhibits a broad PL emission at 750 -$1000\,\mathrm{nm}$ without the clear ZPL. The lifetime of the excitation state is $1.2\,\mathrm{ns}$ which is comparable to other QEs in hBN. Due to the complex inhomogeneous spin environment, the spin coherence of V_B is limited. The spin-lattice relaxation T_1 is around 5-$20\,\mu\mathrm{s}$ which depends on the hBN material quality. Understanding the domain decoherence source is the key to protecting the coherence time. Recently, several papers investigated the nuclear spin environments of V_B[64, 65], and demonstrated a way to extend the coherence time which might be comparable to the

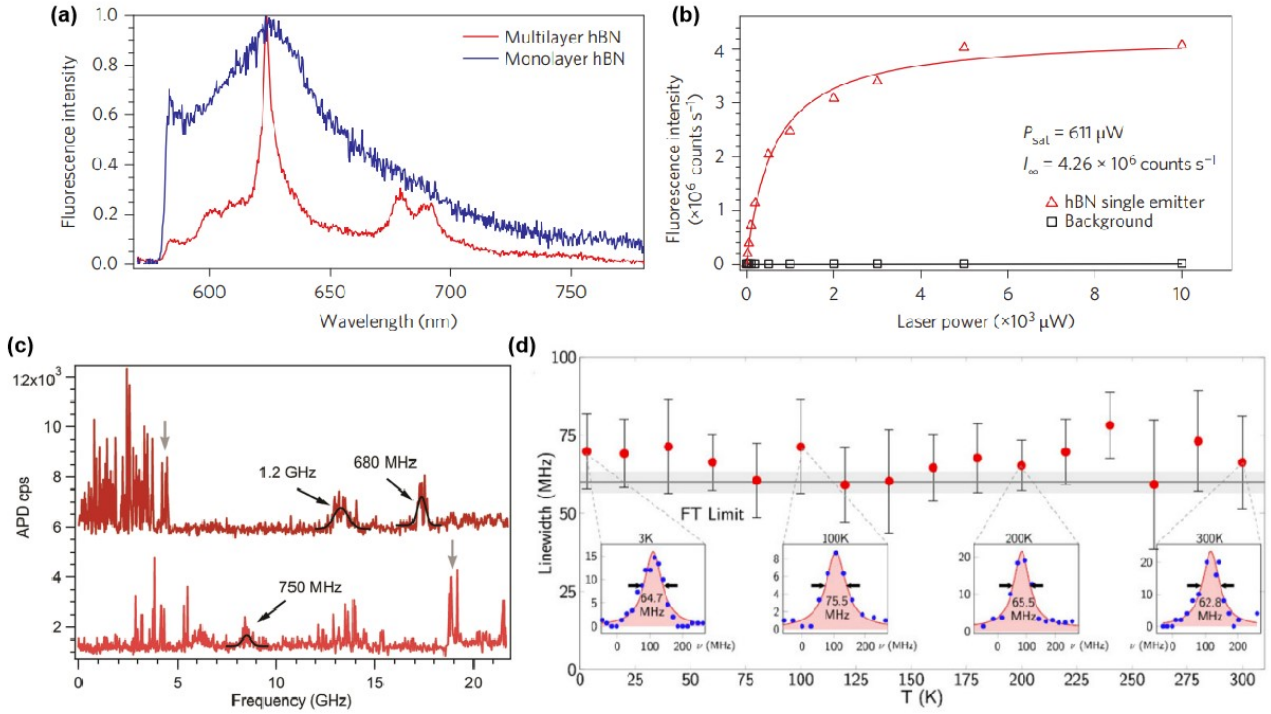

Figure 1.8. The optical properties of QEs in hBN. (a) The PL emission spectrum of QEs in hBN[55]. The power-dependent PL saturation behaviour of QEs in (a)[55]. (c) Photoluminescence excitation (PLE) of QEs in hBN[58]. (d) Fourier transform limited lines in photoluminescence excitation from 3 to 300 K[59].

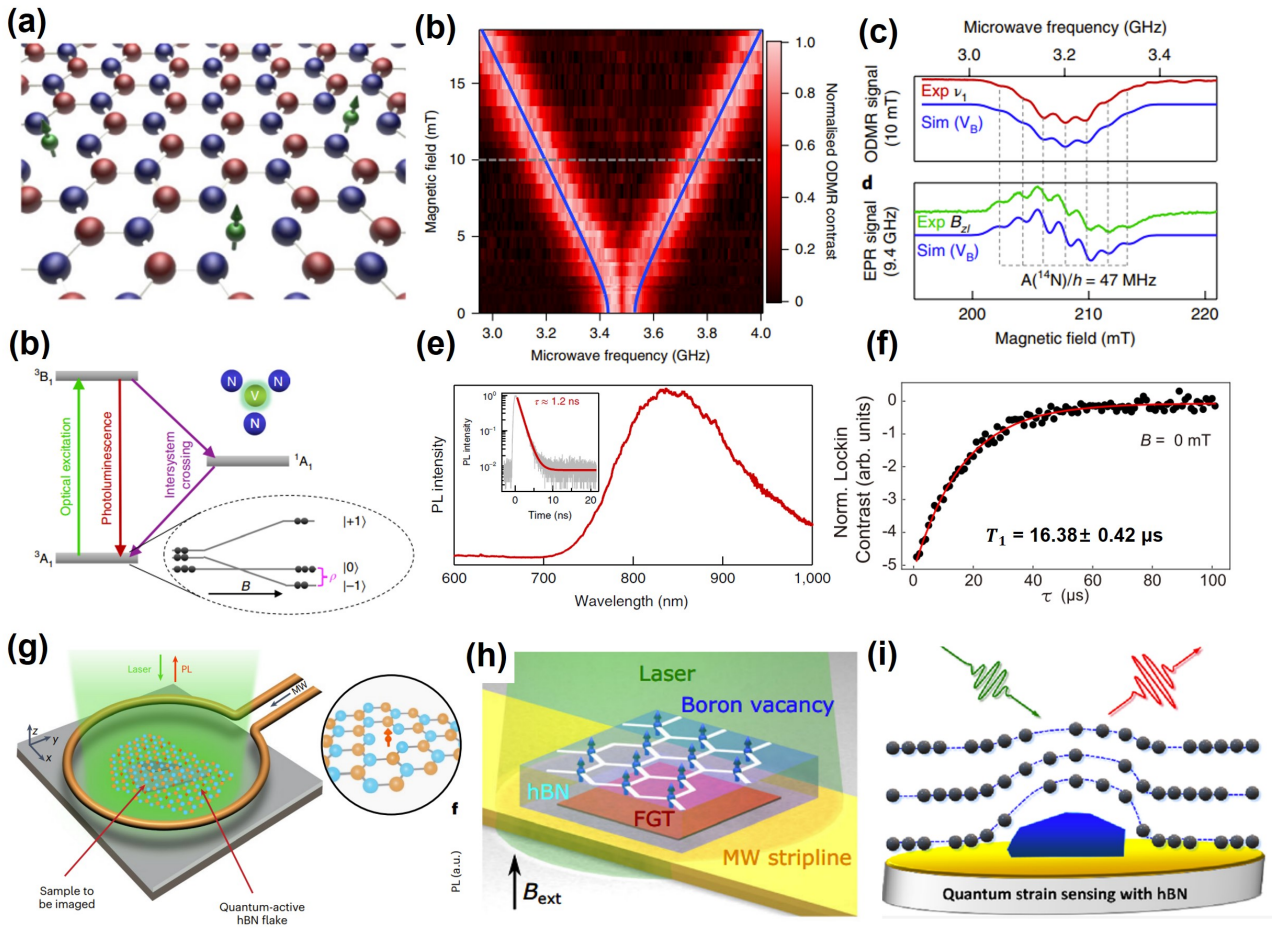

Figure 1.9. (a) Atomic structure of V_B. (b) The PL spectrum of V_B[60]. (c) The energy level of V_B. (g) Quantum microscopy with van der Waals heterostructures[61]. (h)Wide field imaging of van der Waals ferromagnet Fe_3GeTe_2 with V_B. [62]. (i) Strain quantum sensing with V_B[63].

nanodiamond[66, 67].

Notably, its resonance frequency shift in ODMR is not only sensitive to static magnetic fields but also to temperature and pressure changes [68]. The coupling coefficient between zero-field ODMR and temperature in the temperature range 50–350 K is eight times larger than the corresponding factor for NVs in diamond, which is interesting for temperature sensing under cryogenic conditions[69]. In the last three years, V_B has emerged as an important probe for 2D material wide-view magnetic field, temperature and straining sensing in Fig. 1.9(g-i). Compared to NVs in the bulk diamond, V_B as a natural atomic scale sensor, could be very close to the surface of the target object to improve the sensing resolution. Consequently, the hBN, as a 2D material, can be easily transferred to another material system. This would expand the already large suite of unique features displayed by 2D materials.

The big drawback of V_B is the difficulty of reliably engineering the single-level V_B. This is because the single V_B feature poor optical properties, such as weak PL emission, strong non-radiative trasition, and photobleaching. Therefore, V_B is not suitable for the quantum light source. More recently, ODMR signal has been found in some QEs at a single level but not V_B and the origin of the QEs is not agreed. In 2021, Jörg Wrachtrup's group found the ODMR with single-photon QEs at cryogenic temperature[70]. They observed the negative and positive ODMR contrast on these QEs. The defect spins show an isotropic Landé g factor of $\sim$2 and axial zero-field splitting D below $10\,\mathrm{MHz}$. Combined with the theoretical work, they predict these QEs are carbon-related defects. Spin coherence properties of spin-lattice coherence time T_1=17$\pm$4 μs and inhomogeneous dephasing time T_2^*=57$\pm$10 ns for QEs with positive ODMR contrast, and T_1=13$\pm$3 μs and T_2^*=41$\pm$3 ns for QEs with negative ODMR contrast are extracted from their ODMR spectrum. In 2022, Stern et al reported the room-temperature ODMR of single-photon QE in hBN[71]. Similarly, these QEs display positive and negative ODMR contrasts. The QEs exhibit an angle-dependent doublet resonance, which is consistent with a $S > 1/2$ system with modest zero-field splitting. However, there is no spin coherence information from these QEs. They claim these QEs are carbon-related defects. In 2023, Guang-Can Guo's group developed an efficient way to fabricate ultra-bright ($3.7\,\mathrm{MHz}$) QEs in hBN[72], where these QEs show the ODMR signal with positive contrast. These QEs seem a $S = 1/2$ system from its magnetic field-dependent ODMR where the resonance frequency is linear splitting with Landé g factor of $\sim$1.94. They also successfully coherently manipulated these QEs, and investigated coherence properties of T_1=16.17$\pm$1.55 μs and T_2=2.45 $\pm$0.41 μs. Most recently, in 2024, Hannah L. Stern's group discovered a $S = 1$ QEs exhibiting a similar energy level as NVs in diamond and V_B in hBN. They have an axial zero-field splitting parameter D of $1.96\,\mathrm{GHz}$ and a transverse zero-field splitting parameter E of $60\,\mathrm{MHz}$. Microwave-based Ramsey interferometry reveals an inhomogeneous dephasing time $T_2^*$of $\sim$100 ns. Interestingly, the continuously driven spin Rabi coherence time $T_{\rho,\mathrm{Rabi}}$ is prolonged beyond $1\,\mu\mathrm{s}$ at room temperature with no magnetic field.

Standard dynamical decoupling pulse protocols yield a spin-echo coherence time T_2 of $\sim 200\,\mathrm{ns}$, which exceeds $\sim 1\,\mu\mathrm{s}$ with ten refocusing pulses. A better spin-lattice coherence time T_1 is also found around $200\,\mu\mathrm{s}$ which is much better than V_B.

1.2.3 Quantum emitters in aluminium nitride

In the last five years, there has been some progress on QEs in another nitride semiconductor, aluminium nitride (AlN). In 2019, researchers found single-photon QEs in AlN at room temperature as shown in Fig. 1.10(a-b). In Fig. 1.10(b), the power-dependent photon emission correlation spectrum $g^{(2)}(\tau)$ indicates that there are at least three energy levels. AlN is a suitable substrate for on-chip photonic devices. Some studies report the integration of QEs in the photonics device in 1.10(c). These QEs have high PL emissions and low multiple photon rates as shown in Fig. 1.10(d-e). More recently, researchers have created an array of QEs in free-standing AlN via femtosecond laser writing technology as shown in Fig. 1.10(f). These QEs exhibit a high DW factor (>65%) with a ZPL of $609\,\mathrm{nm}$ in Fig. 1.10(g). The first-principles calculations predict the nature of this QE is $N_{Al}O_N$ in Fig. 1.10(i).

AlN is a much better commercially available semiconductor than the previously introduced materials. Its growth and doping process are also well-developed, which would benefit the creation process for QEs . The study on QEs in AlN is still at an early stage. There are still many interesting sciences that need to be explored. For example, the detailed shelving process is still unclear. Understanding its photodynamics is fundamentally important for unlocking new technology and applications. Building on that, in this thesis, I will discuss my recent publication 'Emission dynamics of optically driven aluminum nitride quantum emitters' in Chapter 5.

1.2.4 Quantum emitters in gallium nitride

Another interesting host of QEs is gallium nitride (GaN): the most commercially successful third-generation semiconductor. Similarly, GaN has a mature industrial material market. Around 10 years ago, researchers found the QEs in GaN at room temperature, and there are many following works. Especially, in 2018, some groups discovered that single-photon QEs with telecom range ($1100\,\mathrm{nm}$ to $1300\,\mathrm{nm}$) in Fig. 1.11(a-b)[76]. Moreover, its CW excitation saturation PL rate could be enhanced over $1\,\mathrm{MHz}$ within an optical structure. This work paves the way for the quantum communication based on GaN. In 2018, another interesting work is the realization of the resonance excitation of QEs in GaN. The QEs are stable under non-resonant excitation and exhibit nearly Fourier-transform-limited lines of $\sim 250\,\mathrm{MHz}$ under coherent excitation[77]. This built the foundation

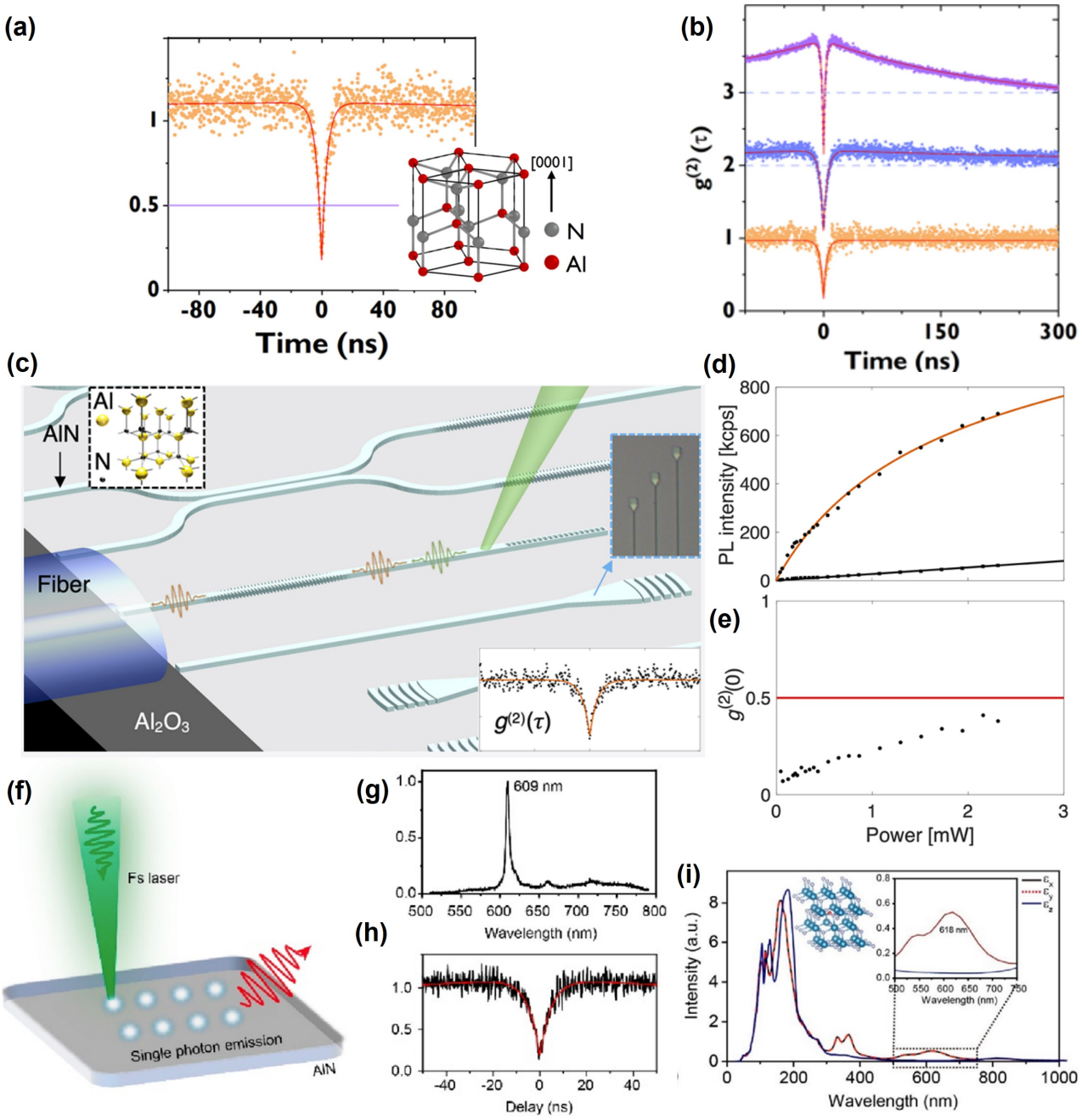

Figure 1.10. Recent progress on QEs in AlN. (a) Single-photon QEs in AlN (The insert is the Wurtzite lattice structure of AlN) and its (b) power dependent $g^{(2)}(\tau)$ from [73]. (c-e) from [74] shows (a) the diagram of photonics integration QEs in AlN, power-dependent PL emission and $g^{(2)}(0)$. (f-i) from [75] display (f) the diagram laser writing QEs on freestanding AlN, (g) the PL emission spectrum of laser-written QEs, (h) $g^{(2)}(\tau)$, and (i) the PL spectrum from first principle calculation where the insert figure is the lattice structures of the point defect $N_{Al}O_N$.

for the generation of indistinguishable photons, entanglement, and realization of optical coherent control of the emitters' quantum states More recently, in 2024, Gregory D. Fuchs' group reported the

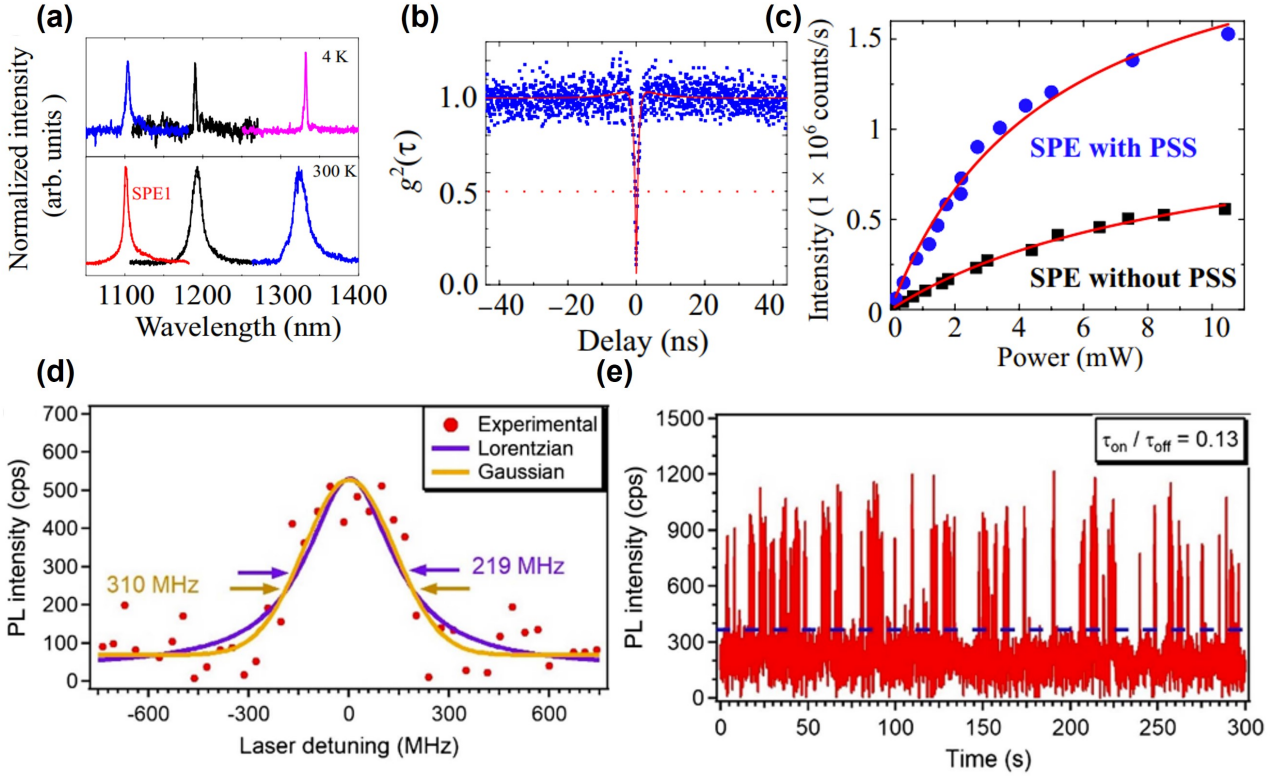

Figure 1.11. Optical properties of typical QEs in GaN. The figures in the first row are (a) PL emission spectrum in the telecom range, (b) $g^{(2)}(\tau)$, and (c) laser power-dependent PL saturation of QEs from [76]. The figures in the second row are (d) resonant PL excitation measurements, and (e) PL emission histogram under fixed coherent excitation from[77] where the dashed line is the threshold used for the on-off ratio of 0.13.

ODMR signal with the QEs in GaN at room temperature[78]. They fabricated the solid immersion lens (SIL) on the GaN substrate to enhance the PL emission as shown in the insert image in Fig. 1.12(a). $800\,\mathrm{kHz}$ PL rate is achieved in a SIL at a saturation laser power of $\sim 1\,\mathrm{mW}$. The QEs show narrower ZPL around the $620\,\mathrm{nm}$ with the DW factors of >0.5 in Fig. 1.12(a), and $g^{(2)}(\tau)$ confirm they are single-photon QEs in Fig. 1.12(b). Two different types of QEs are clarified based on their ODMR responses and photodynamics. The group I QEs exhibit similar energy levels and spin selective photodynamics as NVs in Fig. 1.12(c), while the group II QEs shows the ODMR contrast is from its shelving state instead of ground state in Fig. 1.12(d). Moreover, the group I QEs display two resonances dip with 2% negative ODMR contrasts as shown in Fig. 1.12(e), in contrast, group II QEs show three peaks with > 5% positive ODMR contrast in Fig. 1.12(f) where the contrast of middle-frequency resonance is up to 30% positive contrast. From the Rabi oscillation, the QEs could be manipulated by microwave (MW) at room temperature in Fig. 1.12(g). The lower-frequency and higher-frequency transitions have a Rabi spin coherence time of $T_{Rabi} = 108 \pm 4\,\mathrm{ns}$ and $113 \pm 5\,\mathrm{ns}$,

respectively, whereas the intermediate-frequency resonance has $T_{Rabi} = 41 \pm 4\,\mathrm{ns}$.

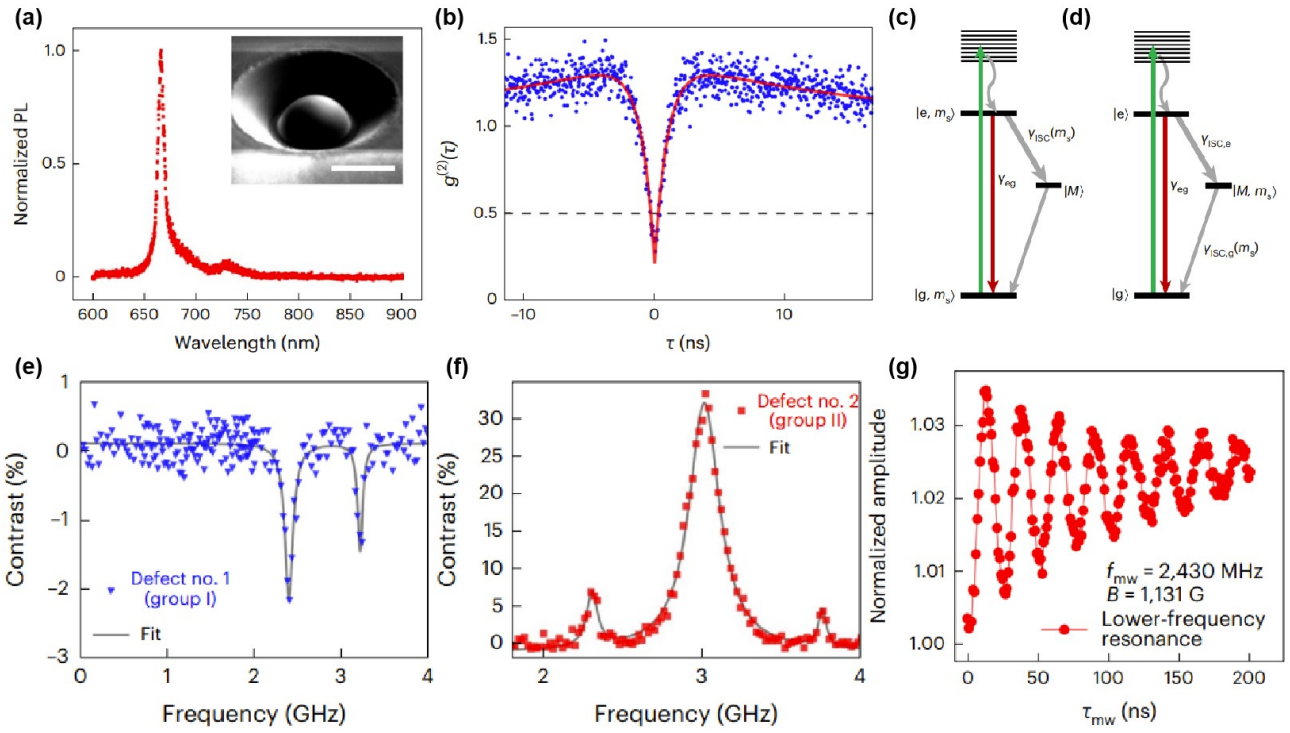

Figure 1.12. QEs in GaN with ODMR signal[78]. (a) is the PL emission spectrum of QEs where the insert is a solid immersion lens on the GaN surface to enhance the PL emission collection efficiency. (b) is the $g^{(2)}(\tau)$ of QEs. (c) and (d) are the predicted energy levels for QEs of group 1 and group 2, respectively. (e) and (f) are the ODMR spectrum for QEs of group 1 and group 2. (g) is the Rabi oscillation of lower-frequency resonance in (f).

QEs in GaN is a very promising field. And there are many important questions which haven't been answered. For example, the nature of these QEs in GaN is unknown, and the creation process for QEs hasn't been well-established. This encourages my study on the creation of QEs in GaN which is listed in Chapter 6 and Chapter 7.

Chapter 2

Experiment method

In this chapter, I will introduce the experiment sample, experiment setup, and experiment approach used in this thesis. In this thesis, QEs in diamond, AlN, and GaN are formed as part of the growth process, or fabricated through ion implantation or femtosecond laser writing followed by high-temperature annealing. These QEs are investigated for their photo-dynamics, spectral, and spin coherence properties by the home-built ODMR setup.

2.1 Experiment sample

2.1.1 Diamond sample

In this thesis, I investigated three types of waveguide integrated NVs (WGINVs) in three different types of free-standing single-crystal diamonds with (100) orientation purchased from element six. The high-quality chemical vapour deposition (CVD) electronics-grade (EG) diamond is used to fabricate the single WGINV. This type of diamond contains less than 5 ppb nitrogen impurities and 0.001-0.1 ppb NVs density. The so-called Ib high-pressure high-temperature (HPHT) diamond, with abundant (over 200 ppm) nitrogen impurities but much less (0.001-1 ppb) native NVs density, is used to fabricate the ensemble WGINVs by laser writing and subsequent annealing. The last type of diamond is an NVs-rich CVD diamond (DNV-B14) containing over 4.5 ppm native NVs with T_2^* of $0.5\,\mu\mathrm{s}$. The high-quality waveguides are fabricated by direct laser writing without any post-annealing process to activate the laser-formed NVs.

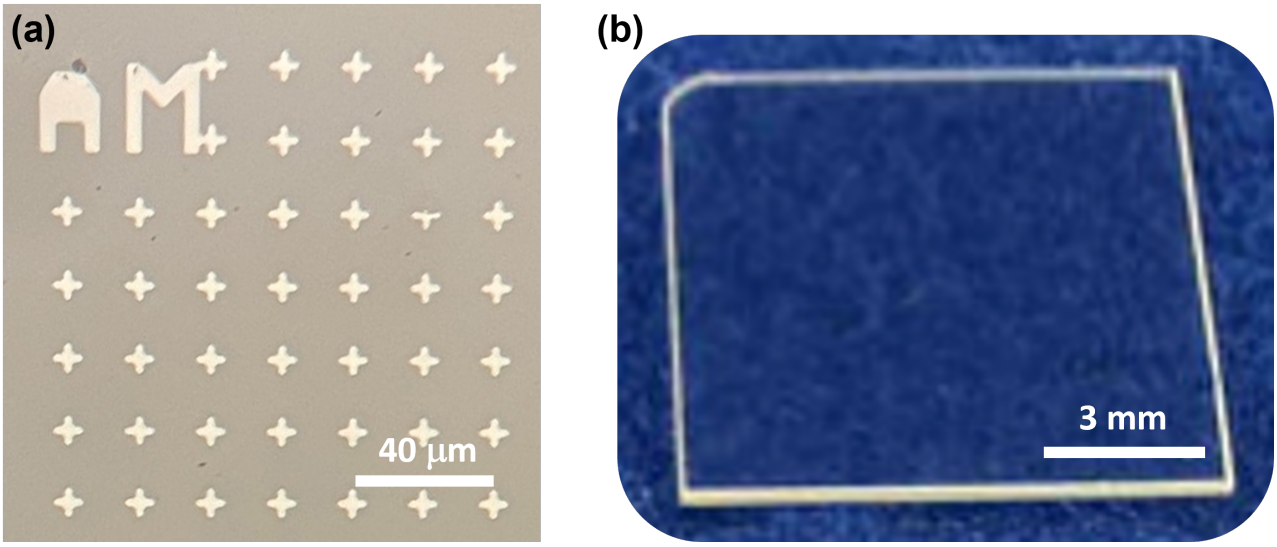

Figure 2.1. (a) AlN films with the marks by optical-lithography. (b) Free-standing GaN.

2.1.2 Aluminium nitride sample

I investigated the native quantum emitters in commercial c-plane $1\,\mu m$ AlN film with the sapphire substrate purchased from Dowa. As shown in Fig. 2.1(a), the surface of AlN has been marked with gold crosses by optical lithography. In this case, the QEs could be positioned by these coordinate systems.

2.1.3 Gallium nitride sample

I studied four single-crystal free-standing GaN with (0001) C plane purchased by MSE Supplies which are nominally undoped, silicon-doped (Si-doped), germanium-doped (Ge-doped), and iron-doped (Fe-doped), respectively. As shown in Fig. 2.1(b), the sample is $10 \times 10 \times 0.5\ mm^3$.

2.2 Experiment setup

2.2.1 Confocal ODMR setup

The confocal ODMR setup consists of the optical part, timing control part, and MW part. The optical part consists of a pulse excitation optical path and a PL collection path. In the pulse excitation optical path Fig. 2.2(a), a 532 laser travels from the laser source (Diode Pumped Green 532 nm Crystal Laser), optical polarised by the linear polariser LPVIS100-A (LP), aligned by

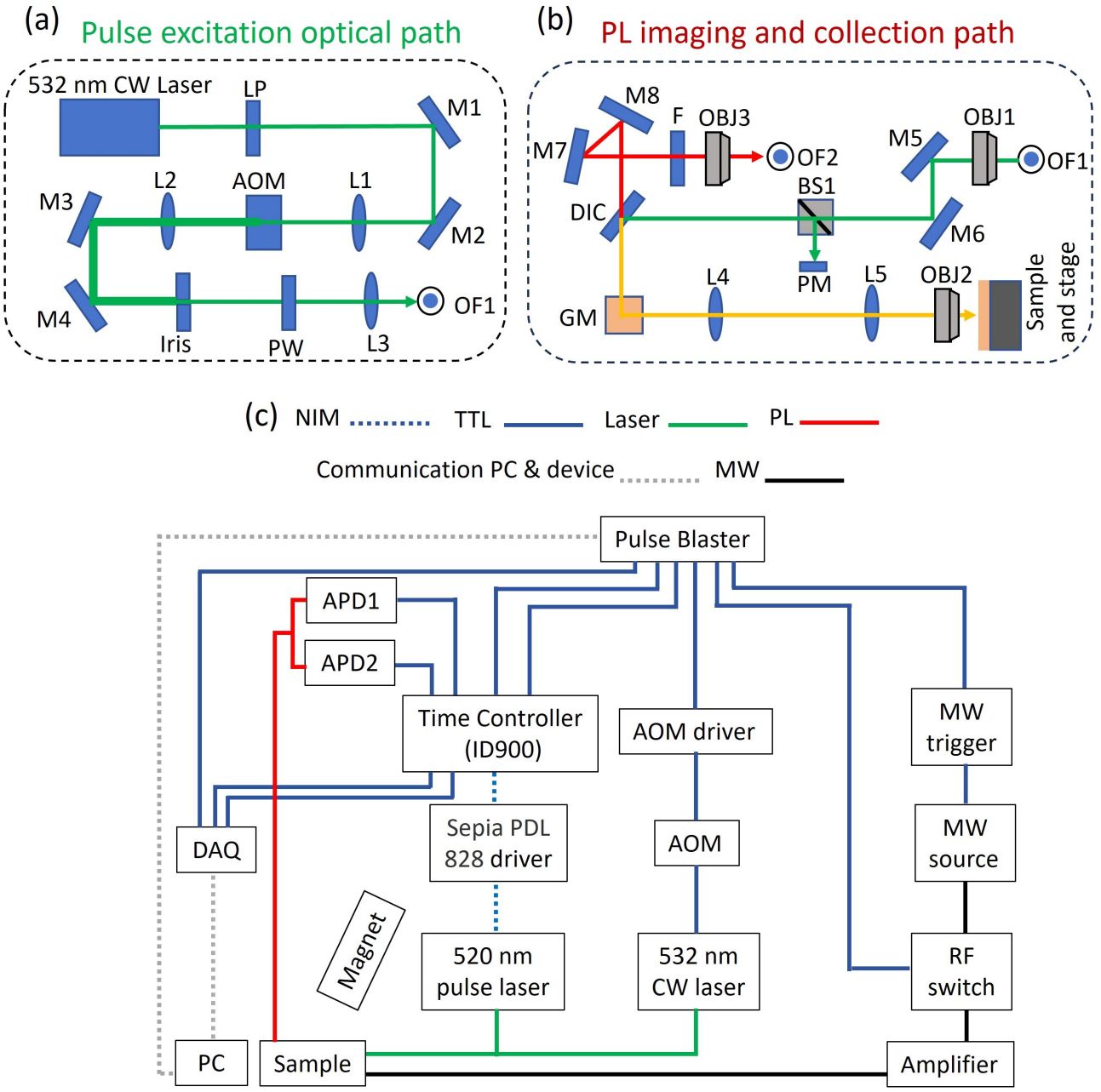

Figure 2.2. Confocal setup. (a) Pulse excitation optical path. (b) PL imaging and collection path. (c) The diagram of electronic devices and their connections.

a pair of plan mirrors BB1-E02 (M1 and M2), coupled into acoustic-optic modulator (AOM) by a pair of optical lenses AC254-125-A (L1 and L2), realigned by a pair of plane mirrors BB1-E02 (M3 and M4), and laser diffraction spot selection by diagram iris, filtered by power wheel FW102 (PW), finally coupled into an angled optical fibre P5 488 PM FC-1 (OF1) by reflective Collimator (RC04FC-P01). The AOM (ISOMET 553F-2) feature $< 10\,\mathrm{ns}$ rise and fall time, can be modulated by an RF signal from the timing control part. The laser is divided into different order lasers by AOM, and the first-order diffraction laser is selected by the following diagram iris. The ratio of first-order laser power between AOM OFF and ON is around 2.3E-4.

In the PL imaging and collection path Fig. 2.2(b), the excitation laser comes out from angled optical fibre (OF1) by a Zeiss objective (OBJ1) with numerical aperture (NA) of 0.25, then is realigned by a pair of mirrors BB1-E02 (M5 and M6), divided by the beam splitter BS025 (BS1), reflected by the dichroic-mirror (DIC), coupled into a 2-axis Galvo mirror GVS002 (GM), sent to a 4-f imaging system with two optical lenses AC254-150-A (L4 and L5), focused into QEs in the sample by a Nikon 100$\times$ objective (OBJ2) with NA 0.9. Meanwhile, the PL from the sample goes through the same objective, 4f imaging system, and 2-axis Galvo mirror but passes through the dichroic mirror, realigned by a pair of mirrors BB1-E02 (M7 and M8), goes through the optical filters (F) to remove the laser reflection and Raman, and finally is coupled into an optical fibre P1-SMF28-FC-2 (OF2) by a Zeiss objective (OBJ3) with NA=0.25 which is connected to SPCMAQRH silicon avalanche photodiodes (APDs) or an ANDOR spectrometer (Shamrock 750) with a silicon CCD. The optional neutral density (ND) filter is also used to keep the PL rate within the APD working range ($2\,\mathrm{MHz}$). The beam splitter BS1 before the dichroic mirror offers a path for a laser power meter PM100D (PM) to monitor the laser power.

As mentioned in the chapter 1, a repetitive measurement is required here to estimate the qubit state. A repetitive sequence is operated by a timing control which is based on the Pulse Blaster ESR PRO 500 with a 500 MHz internal clock and 21-bit high-frequency output channel. As illustrated in Fig. 2.2(c), a customized labview software developed in the computer (PC) is used to control the Pulse Blaster which generates the pulse to gate the time controller ID900 for the pulse laser, AOM, RF switch, MW external trigger, and NI-DAQ based on the designed sequence. In this case, the PL collection count, MW source, and laser source could be synchronously triggered which can generate the standard sequence for quantum coherence measurements, such as Rabi oscillation, free induction decay, Hahn echo, and T_1 measurements [14].

As shown in Fig. 2.2(a), the MW field is generated by a MW source (E4438B), modulated by an RF switch (ZASWA-2-50DRA+) and amplified by a MW amplifier (ZHL-42W+), eventually transmitted to the sample by a planar ring antenna on a printed circuit board (PCB). In Fig. 2.3(a), the antenna is designed in Altium Designer by taking reference from previous studies[79]. As shown in Fig. 2.3(b), this PCB is fabricated on the single-sided copper clad board FR4 purchased from RS.

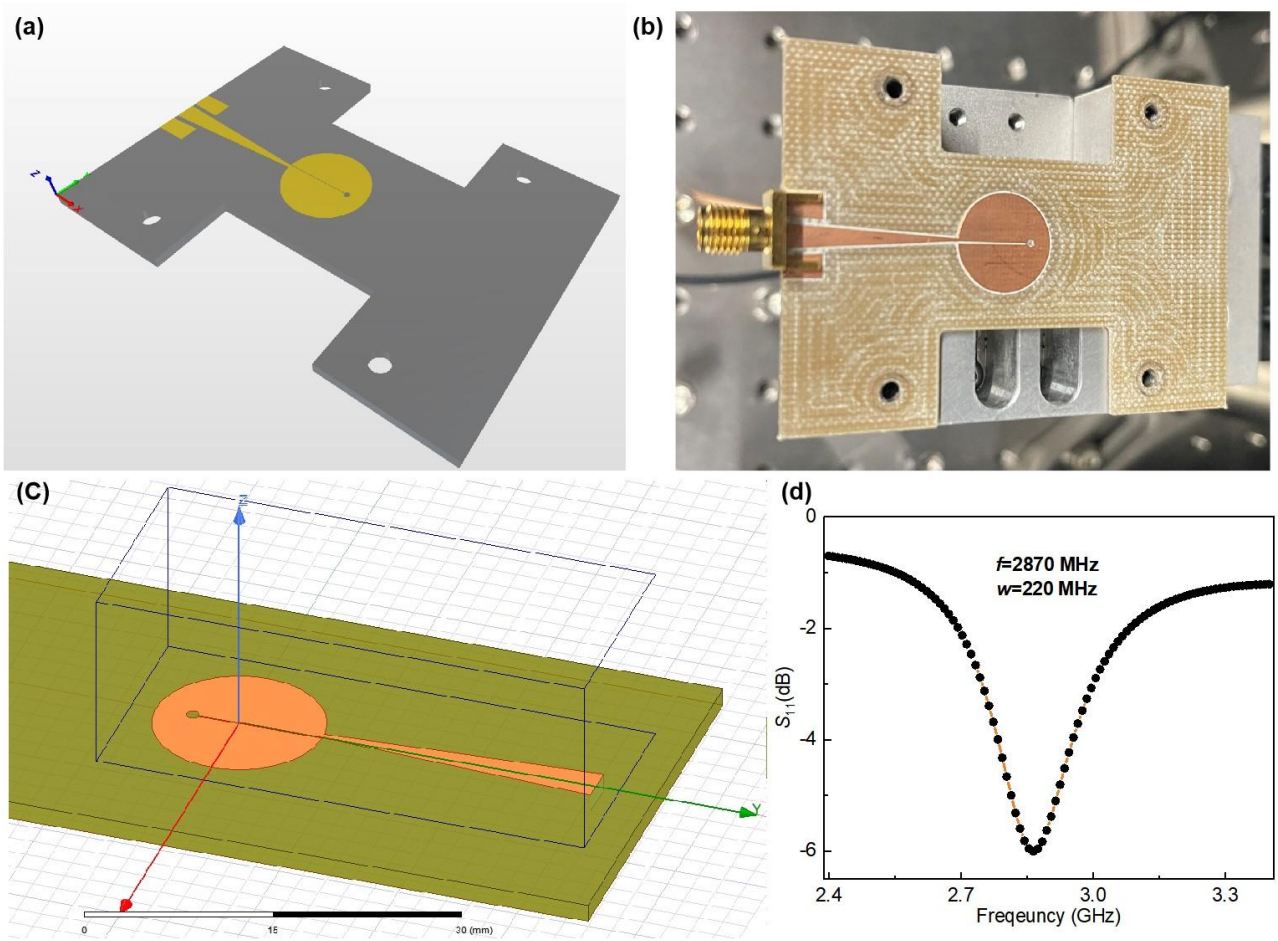

Figure 2.3. The planar ring antenna. (a) The three-dimensional (3D) antenna on the PCB from the Altium Designer. (b) The photo of the PCB and the patch antenna. (c) The 3D antenna model in Ansys HFSS (d) The simulation S_{11} parameter for the antenna in (a).

In Fig. 2.3(c), I used the Ansys high-frequency structural simulator (HFSS) software to simulate the antenna in (a). From its S_{11} parameter in Ansys HFSS simulation, this ring resonator exhibits the $2.87\,\mathrm{GHz}$ resonance frequency with a linewidth of $220\,\mathrm{MHz}$ in Fig. 2.3(d). This working frequency range is sufficient for the ODMR studies for NVs in this thesis where the applied magnetic field is less than $10\,\mathrm{mT}$.

2.2.2 Fibre-waveguide-fibre ODMR setup

In the fibre-waveguide-fibre configuration, the laser from the pulse excitation optical path in Fig. 2.2(a) is coupled into a fibre polarisation controller for polarisation tuning, then connected to SMF-28 single-mode fibre, coupled into waveguide in diamond by a 3-dimension stage. The green laser would excite the NVs along the waveguide which transmit the PL emission and the green laser along the waveguide. Another SMF-28 single-mode fibre, as output fibre, would extract the

waveguide mode of PL emission and green laser into the fibre space again where the PL emission and green laser are separated by the $532\,\mathrm{nm}$ and $650\,\mathrm{nm}$ long pass filters in free space. The APD and optional neutral density filters are used to read out the PL emission.

2.3 Experimental protocol

2.3.1 Photo-dynamics of quantum emitters

QEs arise from defects in semiconductors, exhibiting atomic-like energy structures. Understanding the photodynamics of QEs would reveal the key information for their coherent spin and optical properties and thus comprise foundational elements in quantum information science. Photodynamics includes the study of the radiative and non-radiative transition between internal electronic levels which includes electron-phonon interactions, intersystem crossings between different spin manifolds, and ionization or recombination events[80]. These dynamic processes are crucial to control and harness their quantum properties.

Inspired by quantum dots and QEs in diamond, the photodynamics study has been expanded to various QE systems, such as QEs in hBN, GaN and AlN. Although these novel QEs feature excellent spin and optical properties, most of them haven't been identified with thier atomic structure. This significantly hinders its possibility to deterministically create, and integrate them into photonics devices, and weakens its reproducibility [81]. Thus the photodynamics study explores the QEs' electronic structures, providing important information to assist theoretical work in the identification of these novel QEs's nature. In this thesis, I used the photo emission correlation spectrum (PECS), time-resolved PL (TRPL) spectrum, and photodynamic simulation to investigate the photodynamics of QEs in diamond, AlN and GaN.

Photon emission correlation spectrum

PECS is a valuable technique for probing the optical and spin dynamics of a quantum emitter. PECS involves analysing photon time correlations in the PL emission from the atomic-like internal energy structure as shown in Fig. 2.4. It is widely used to verify single-photon emission associated with QEs through the observation of photon antibunching.

As shown in Fig. 2.4, PECS was recorded using the ID900 time-tagging mode, with photon arrival times acquired from two detectors in a Hanbury-Brown and Twiss interferometer. Custom software numerically correlates each photon detection on one detector with all the other registered photons on the second detector within a specified time window.

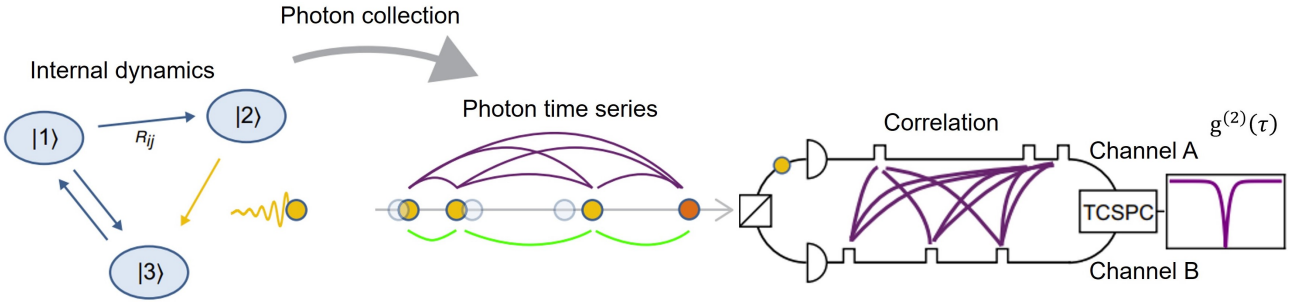

Figure 2.4. The process of PECS[82]. From the left, a laser source pumps the system into internal dynamics where photons emit during the radiative transition. The emitted photons (yellow circles) are collected into a photon time series, which also includes experimental noise, such as timing errors (light grey circles), and background photons (orange circles). A beam splitter then splits the photon stream into two separate detectors (empty semicircles), corresponding to two different channels. A time-correlated single-photon counter (TCSPC) records the arrival times of photons at each channel, and time correlations between all photons are calculated to create the PECS.

For the photon-statistics definition, the autocorrelation function is given by

$$g^{(2)}(\tau) = \frac{\langle I(t)I(t+\tau)\rangle}{\langle I(t)\rangle^2} \tag{2.1}$$

where I(t) is the intensity at time t, τ is the time delay between two intensity measurements and represents the time average of the enclosed quantity. The $g^{(2)}(\tau)$<1 represents a decreased probability of detecting two photons separated by τ. This phenomenon is referred to as antibunching and corresponds to a quantum source with a sub-Poissonian photon distribution. In contrast, $g^{(2)}(\tau)$>1 represents increased detection probability, is referred to as bunching and corresponds to a super-Poissonian photon distribution. Any region where $g^{(2)}(\tau)$=1 corresponds to uncorrelated Poissonian light.

For an ideal single-photon emission, the probability of detecting two photons with zero delay, $g^{(2)}(0)$, should be zero. For a multiply(n)-photon emission

$$g^{(2)}(0) = 1 - \frac{1}{n} \tag{2.2}$$

Using this relationship, it is apparent that $g^{(2)}(0) = 0$ for $n = 1$ and that $g^{(2)}(0) \geq 0.5$ for $n \geq 2$. Hence, it has become common practice to check single-photon emission whether its measured $g^{(2)}(0)$ is less than 0.5. I note that this assumption is based on the QEs exhibiting the same (or similar) emission rates.

Time-resolved PL spectrum

The TRPL spectrum directly records the PL histogram of emitters with an ID900 time controller, as shown in Fig. 2.2(c). By using an ultrafast picosecond pulse laser, the lifetime ($>1\,\mathrm{ns}$) of the excitation state could be measured by tracking its TRPL after the excitation pulse. For the lifetime measurements in this thesis, the QEs are excited by a $520\,\mathrm{nm}$ pulse laser (P-C-520M, PicoQuant) with $130\,\mathrm{ps}$ of pulse-width and $20\,\mathrm{MHz}$ of repetition frequency. The ID900 time controller records the PL histogram of QEs with a time bin of $13\,\mathrm{ps}$.

On another hand, the TRPL could be developed by designing the train of laser pulses to explore the complex dynamics of internal energy levels. Understanding the PL histogram is a prerequisite for designing the quantum control protocol. For example, double laser excitation is used to identify the lifetime of the singlet shelving state of NVs[83], as shown in Fig. 2.5. The PL recovery in Fig. 2.5 (a-b) indicates the population in the singlet shelving state decays to the ground state. Fitting the PL recovery would infer the lifetime of the single shelving state in Fig. 2.5(c). It is important to understand the nonradioactive internal energy levels. As shown in Fig. 2.5(d), the temperature-dependent singlet shelving state lifetime suggests the double singlet shelving states with ΔE $=16.6\,\mathrm{meV}$. Moreover, the TRPL study is also very important to designing initialisation and readout protocols for optical addressing spin which will be discussed in detail in 2.3.2.

In this thesis, for the double-pulse laser excitation and single-pulse TRPL, QEs are excited by the CW $532\,\mathrm{nm}$ laser modulated by the AOM. The PL histogram of QEs was binned with $1\,\mathrm{ns}$ resolution. The spacing between each laser pulse train is $50\,\mu\mathrm{s}$ to reset the ground state population of QEs. I note the timing jitters in this thesis will lead to an instrument response time of around half ns which includes the electronic device jitters of ID900, APD response time and pulse-width of the pulse laser.

Photodynamics simulation

For any *N*-level electronic structure, the full optical dynamics are calculated by a system of *N*-coupled differential equations [82].

$$\frac{dP}{dt} = G \cdot P \tag{2.3}$$

where *P* is a vector of state occupation probabilities and *G* is the transition rate matrix, where the G_{ij} represents the transition rate from *i* state to *j* state ($i \neq j$). Each diagonal element G_{ii} corresponds to the sum of all transition rates out of state i. The time-dependent state populations of a given model would provide the population dynamics in the internal energy level. By setting different initial parameters, such as the number of energy levels and transition rates, and the boundary condition,

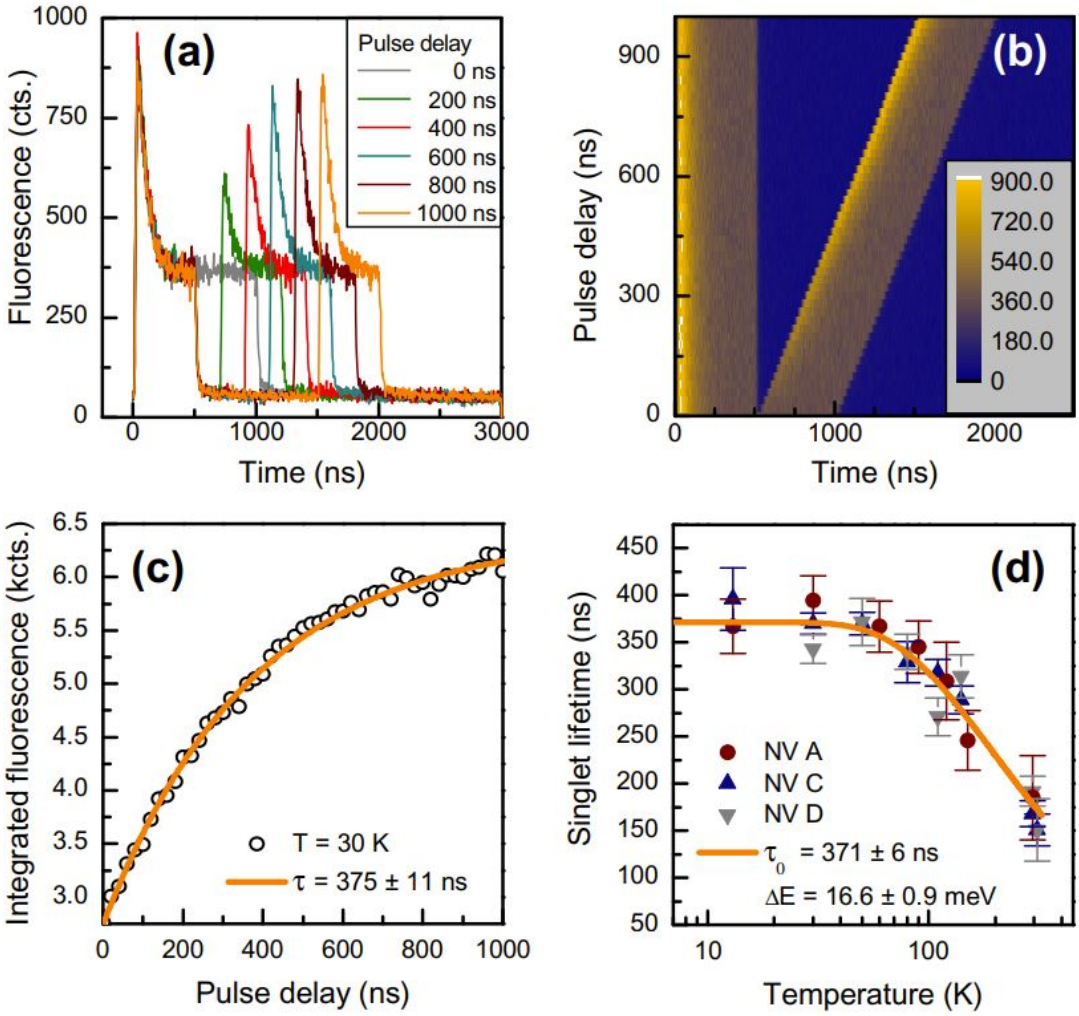

Figure 2.5. Example for measuring the lifetime of shelving state of NVs via TRPL under double pulse excitation[83]. Decay of the population from shelving states to ground state leads to the recovery of PL: (a) TRPL histogram under double pulse excitation with viable pulse delay and (b) the full histogram of PL with two excitation pulses and variable pulse delay. (c) PL counts integrated over the first 30 ns of the second pulse as a function of pulse delay in (a). The exponential increase is caused by decay out of the shelving state. (d) Temperature dependence of shelving state lifetime. The fit suggests a phonon-assisted transition between shelving states with $\Delta E = 16.6\,\mathrm{meV}$.

the TRPL and PECS could be fully demonstrated.

The TRPL is the PL intensity in the time domain, calculated by

$$I(\tau) = G_{eg} \cdot P_e \tag{2.4}$$

where the $I(\tau)$ is the time-dependent PL intensity, G_{eg} is the transition rate from the excitation state to the ground state and P_e is the population of the excitation state.

The autocorrelation function is proportional to the population of the radiative state, $P_2(t_2)$, given the system started in the ground state P_1 following the detection of a photon at t_1, and then normalised by the steady-state population of $P_2(\infty)$ [84]. This is given by

$$g^{(2)}(\tau) = \frac{P_2(t_2|P(t_1))}{P_2(\infty)} \tag{2.5}$$

where $\tau = t_2$ - t_1 is the time delay of $g^{(2)}(\tau)$.

2.3.2 ODMR experimental protocol

Initialisation, manipulation and readout

ODMR is a useful tool for harnessing spin-based quantum information based on the optically addressable QEs in diamond, silicon carbide (SiC), hBN, and GaN. Because, it paves a convenient way to realize the initialisation, manipulation and readout of QEs which are three indispensable parts of the quantum information processing platform. I will take NVs in diamond as an example to introduce the ODMR experimental protocol used in this thesis.

At room temperature, the thermal excitation leads to a mixed ground state of NVs where the population is identical in the $m_s = 0$ and $m_s = \pm 1$. The first step therefore is using a $532\,\mathrm{nm}$ green laser to initialise its ground state. Specifically, once optically excited in the triple excitation state, the NV electron spin can relax either through the same radiative transition producing a broadband red PL or through a secondary path involving non-radiative intersystem crossing (ISC) to single states as shown in Fig. 1.5. Indeed, optically addressable properties of the NV ground state are dependent on the spin-dependent transition:

(1) Spin-dependent ISC into the singlet states (long time lifetime) from the excited states occurs with greater probability out of $m_s = \pm 1$ than $m_s = 0$ out of the excited state, as the yellow lines in Fig. 1.5(b).

(2) Further, the NV defect decays preferentially from the lowest singlet state towards the ground state $m_s = 0$ sublevel, preparing the system in the ground state to $m_s = 0$.

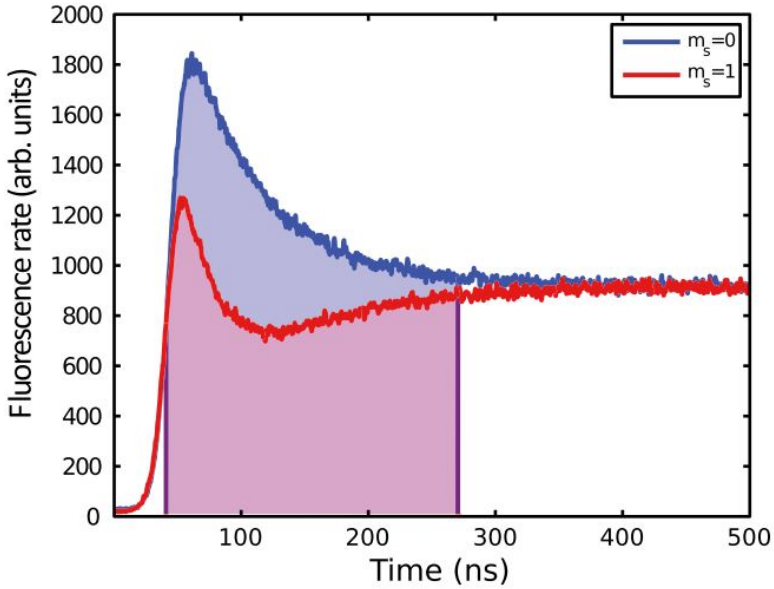

Figure 2.6. TRPL for different NVs spin states. NVs prepared in the $m_s = 0$ states feature higher PL rate than NVs prepared in the $m_s = \pm 1$ states. This spin-dependent PL behaviour is the basis of conventional repetitive optical NVs readout.

In this case, the triplet ground state of the NV electron spin could be initialised from a mixed state to a preferred ground state $m_s = 0$ via a pump laser. Due to the detection-sensitive region of the detector, the relaxation process via single-state is the nonradiative transition that leads to weak PL intensity. Thus, the electron spin originating from $m_s = \pm 1$ has a higher probability of suffering a non-radiation relaxation pathway which weakens its PL emission. This readout mechanism is demonstrated by thier TRPL during a readout laser pulse for NVs initially prepared either in state m_s=0 or $m_s = \pm 1$ as shown in Fig. 2.6. Basically, when the initial state is $m_s = 0$, a high PL emission is initially observed, then decays to a steady-state value due to residual ISC nonradiation transition to the metastable state from the ms = 0 excited state. For the initial state $m_s = \pm 1$, the PL signal rapidly decays to a low level due to faster ISC to the metastable state. Because the metastable state preferentially decays to the $m_s = 0$ state, the low PL level then recovers toward the steady-state value within the metastable state lifetime[16]. Therefore, the population information could be read out via detected PL intensity. However, the limited lifetime of the metastable state and differences in $m_s = \pm 1$ and m_s =0 decay behaviour allow for only probabilistic determination of the NV initial spin state. Therefore a repetitive readout loop as mentioned in 2.2.1 is needed to get a good signal-to-noise ratio. There is another way to read out the ground state which is the photoelectric readout of spin states in diamond[85]. As shown in Fig. 1.5 (b), the NV could be ionized to NV^0 by pumping the NV to the conduction band with an electron released. By choosing

suitable laser power and wavelength, the spin information can be converted to a charge state which can be read out by its current. Particularly, as discussed in 1.1.2, the single-shot readout would greatly increase the readout fidelity[86]. This spin-to-charge conversion method can be used to realize the high-fidelity single-shot readout[87, 88, 89]. However, I will aim for a standard ODMR setup which could easily work on the ODMR with single and ensemble QEs.

As shown in Fig. 1.5, an external magnetic field could further lift the degeneracy of $m_s = \pm 1$ in the ground state sublet. Therefore, the qubit can be defined in a two-energy level system between m_s =0 to $m_s = 1$ or m_s =0 to $m_s = -1$ in the ground state. Then the manipulation is very straightforward via the related MW with resonance frequency[90].

Continuous-wave optically detected magnetic resonance

Continuous-wave optically detected magnetic resonance (CW-ODMR) is a simple, widely used method for quantum sensing based on the NVs. The CW-ODMR spectrum is not only for magnetic field sensing but also the temperature, pressure, and electric field sensing. The measurement protocol consists of the MW driving and the optical initialisation, and the readout occurs simultaneously. Laser excitation continuously initialises NV into the more fluorescent $m_s = 0$ ground state, while MWs tuned near resonance with one of the $m_s = 0 \leftrightarrow m_s = 1$ and $m_s = 0 \leftrightarrow m_s = -1$ transitions drive the NV population into the less PL $m_s = \pm 1$ state, reducing the emitted light. When the local environment changes, such as a local magnetic field, or electric field, this causes a shift in the electron spin resonance frequency, which may be read out through changes in the detected PL at specific MW drive frequencies.

In the simplest CW-ODMR implementation, the MW frequency is swept across the entire NV resonance spectrum, allowing all resonance line centres to be determined. A practical improved version of ODMR adds a reference signal which collects the PL rate as a reference with MW off and laser on as shown in Fig. 2.7.(a). This reference signal is useful to cancel the background noise from setup system instabilities e.g. temperature and laser fluctuations, and improve the signal-to-noise ratio as illustrated in Fig. 2.7(b-c). Specifically, when the background suffers non-MW-related PL fluctuations, the fast-modulating MW would protect the signal against noise. Alternatively, another improved way is that MW frequency may be tuned to a specific resonance feature's maximal slope so that incremental changes in the magnetic field result in maximal changes in PL. The sensitivity of this latter approach can be further improved by modulating the MW frequency to combat noise.

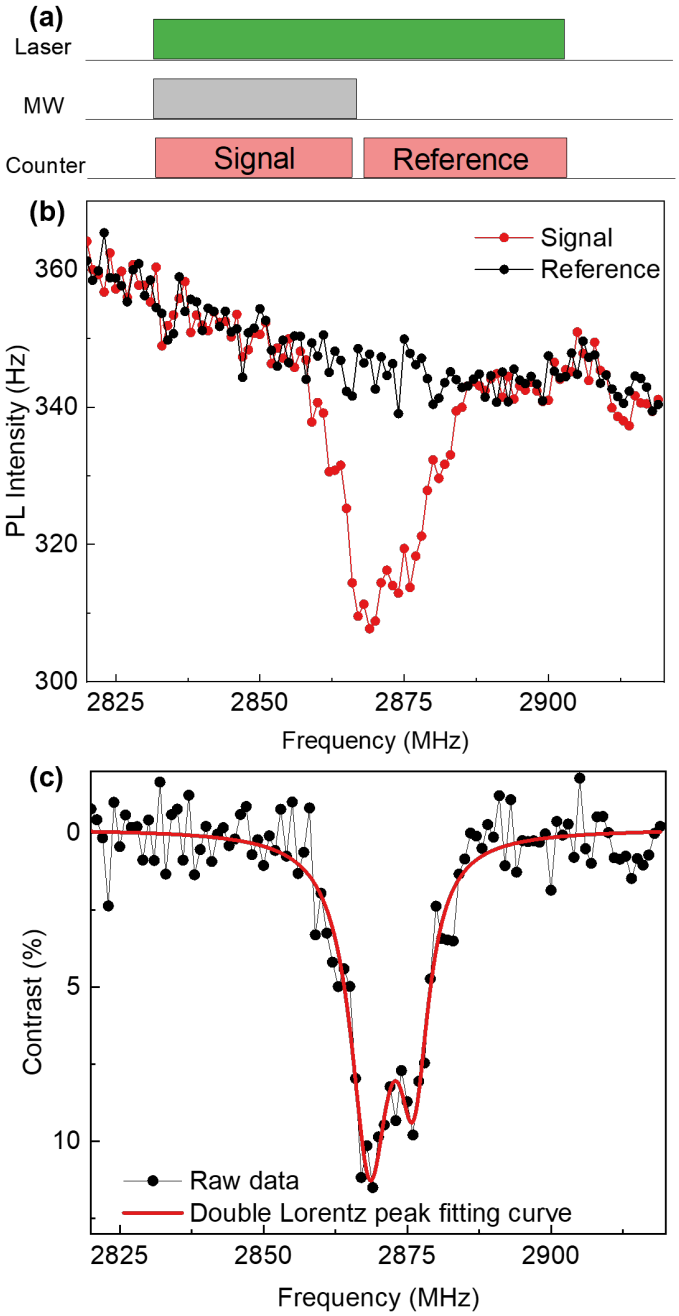

Figure 2.7. The zero field CW ODMR for ensemble NVs. (a) The CW-ODMR sequence. (b) The Non-normalized ODMR spectrum (c) ODMR spectrum is normalized by the signal and reference in (b).

Rabi oscillation

Rabi oscillation is the direct evidence for the coherent manipulation of a qubit, which is the precondition for the quantum information operation. The Rabi measurement protocol of NVs is detailed in Fig. 2.8. Firstly, a green laser pulse is used to initialise the quantum system to the preferred state m_s. Then, a resonance frequency MW pulse with variable duration time τ is delivered to drive the electron spin due to the coherent interaction of the spin with the MW magnetic field. This causes a coherent rotation of the electron spin states between spin levels. Next, the second laser pulse is used to read out the quantum state via PL intensity[90]. The Rabi oscillation can be fitted by the equation,

$$C = Ae^{-\tau/T_{\rho,\text{Rabi}}}\cos(\omega\tau + \phi) + B. \tag{2.6}$$

The C is the Rabi oscillation signal, the A is the Rabi oscillation amplitude, the $T_{\rho,\text{Rabi}}$ is the coherence time in Rabi oscillation, the ω is the Rabi oscillation frequency, ϕ is the phase offset, and B is the Rabi oscillation amplitude offset. Therefore, the MW pulse duration time for π and $\pi/2$ pulse can be calculated by π/w and $\pi/2w$. As shown in Fig. 2.8(b). The Rabi oscillation frequency ω could be tuned by changing the applied MW power, as a result of the magnetic field of MW increasing linearly with the square root of MW power[90]. A linear scaling is observed between Rabi oscillation frequency and the square root of MW power as illustrated in 2.8(c).

Pulsed optically detected magnetic resonance

The biggest drawback of CW-ODMR is the power-broadening linewidth which arises from the laser used for spin initialisation and from the resonant MW field used for spin rotation.[16]. In contrast, a pulsed ODMR would avoid that by separating the MW and laser pulse in the time domain as illustrated in Fig. 2.9. First, the quantum system is initialised from the mixed ground state to the pure $m_s = 0$ by a laser pulse. Second, a near-resonant MW π pulse is followed to prepare the quantum system to $m_s = -1$ or $m_s = 1$. Third, a second laser is sent to read out the PL rate after the MW pulse. Pulsed ODMR spectra were then recorded by continuously repeating the sequence while sweeping the π pulse frequency and recording the PL intensity. By employing this measurement protocol, ODMR can effectively eliminate the laser power broadening effect while achieving optimal contrast. This is because the pulse ODMR protocol efficiently preparation and readout the sublevel m_s of the ground state. As shown in Fig. 2.9, τ_π has a big impact on its linewidth and contrast of pulsed ODMR. The longer τ_π leads to the narrower linewidth. However, the ODMR contacts are not significantly changed until the $\tau_\pi \sim T_2^*$. When the $\tau > T_2^*$, the ODMR contrast will start to reduce due to the dephasing mechanism[16].

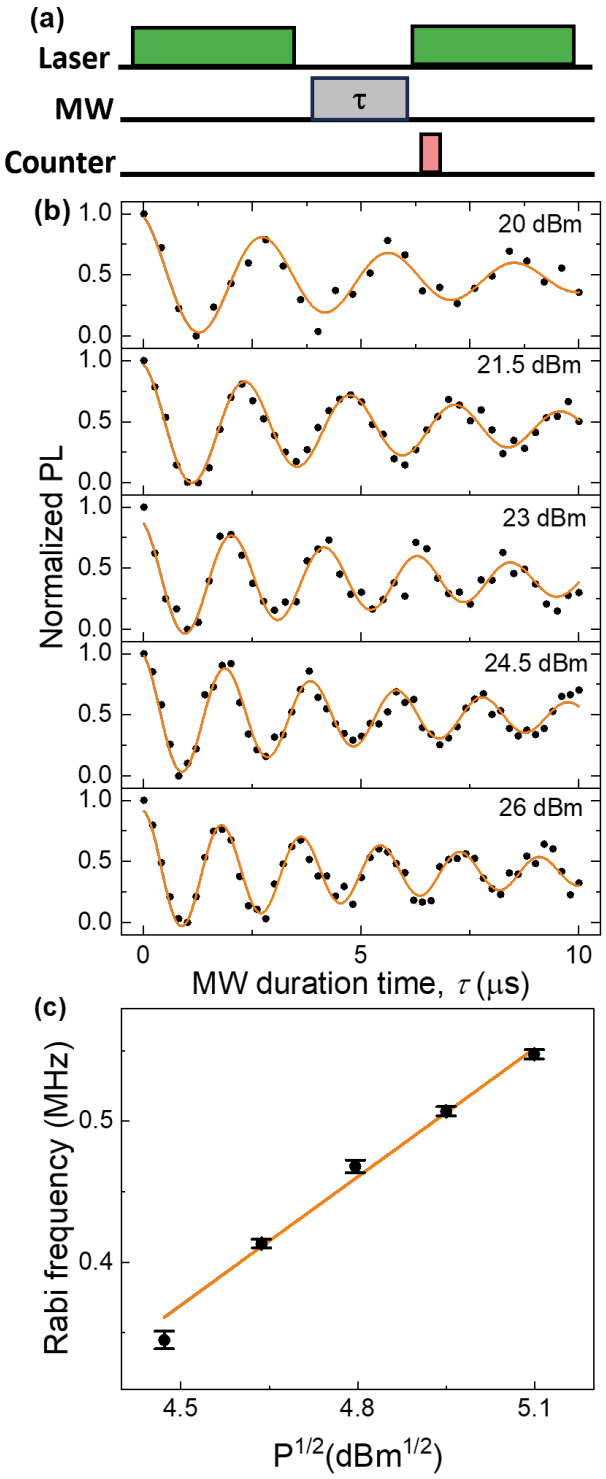

Figure 2.8. Rabi oscillation is driven by MW for NVs. (a) Rabi oscillation measurement sequence. (b) MW power-dependent Rabi oscillations for NV. (c) The linear scaling of Rabi frequency and the square root of MW power.

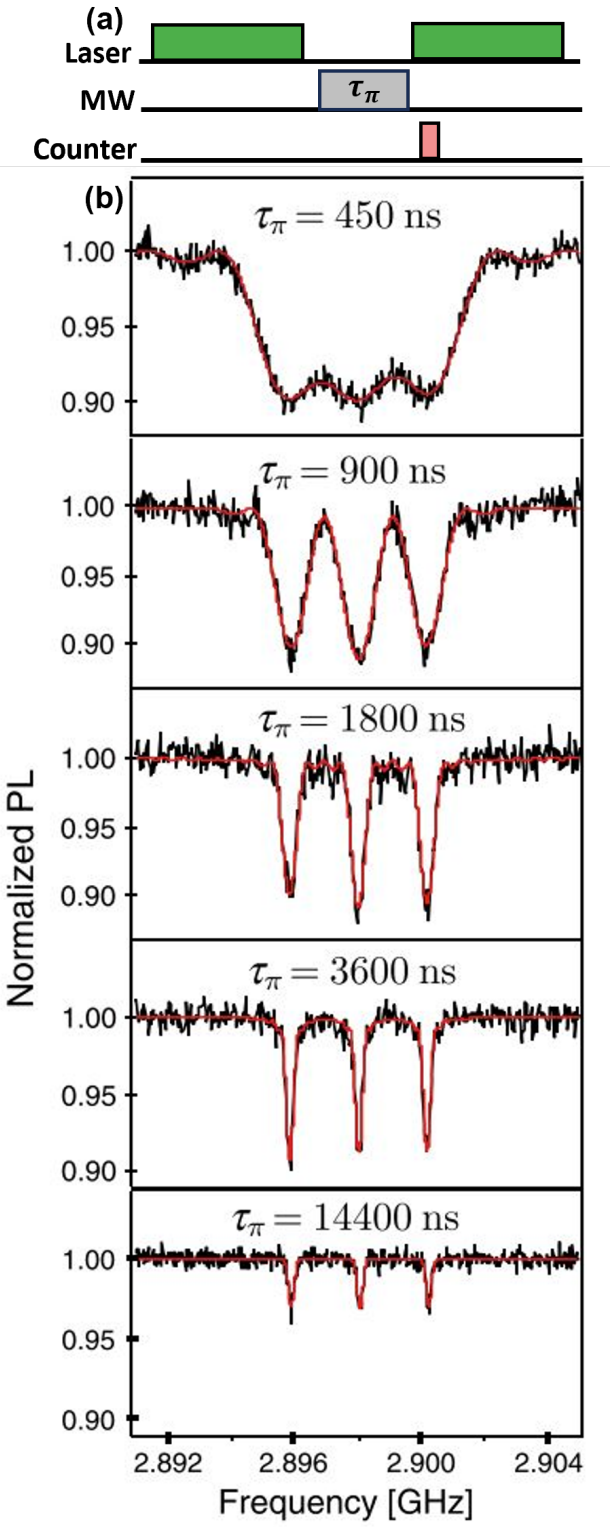

Figure 2.9. (a) Pulse ODMR experimental sequence. (b) Pulsed-ODMR spectra were recorded for different values of the π pulse duration τ_π. The three resonances correspond to the three hyperfine components associated with the ^{14}N nuclear spin[16].

Ramsey interference measurement

Similar to what was discussed before in 1.1.2, the Ramsey interference sequence is sensitive to static energy splitting and, therefore also used to evaluate the inhomogeneous dephasing coherence properties T_2^*. In general, the slow fluctuations of the magnetic field, electric field and strain would introduce phase noise during the free evolution period in Fig. 2.10, limiting the T_2^* of NVs in diamond. The domain decoherence source and origin of NVs are highly dependent on the fabrication protocol of NVs and the diamond crystal quality. For example, the native NVs in IIa diamond exhibit the $T_2^* \sim 2\,\mu s$ which is limited mainly by the dipolar interactions with ^{13}C nuclear spin bath. In contrast, the engineered NVs, for example, the ion implantation created NVs, in IIa diamond are mainly affected, or decohered by the residual fabrication damage, such as the introduced impurities and strain. For NVs in Ib diamond, over $200\,ppm$ impurities are the dominant decoherence mechanism due to the spin noise from the impurities.

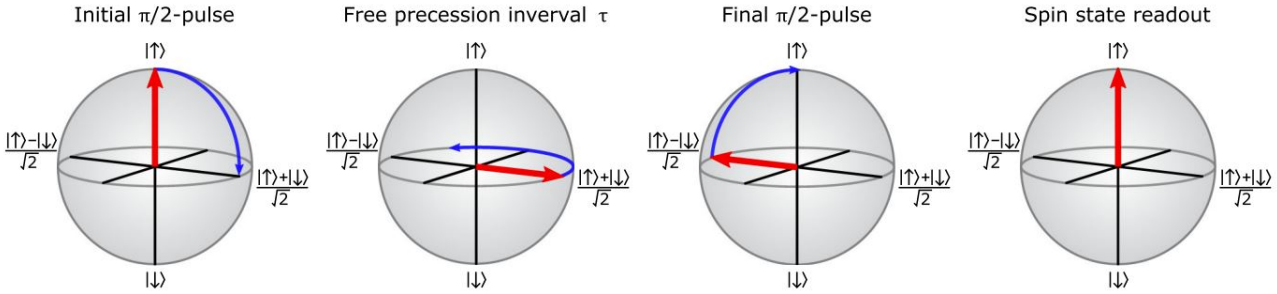

Figure 2.10. Bloch sphere depiction of Ramsey interference sequence[15].

Another decoherence source especially for the ensemble NVs is the spatially inhomogeneous probe conditions (Initialisation, manipulation and readout) and environment (magnetic fields, electric fields, strain, or g factors). In this case, the T_2^* of ensemble is not equal to the most common value of T_2^* for an individual single within the ensemble. Overall, the T_2^* for ensemble NVs can be expressed as[15]

$$\begin{aligned}\frac{1}{T_2^*} \approx & \frac{1}{T_2^*\{\text{electronic spin bath}\}} + \frac{1}{T_2^*\{\text{nuclear spin bath}\}} + \frac{1}{T_2^*\{\text{strain gradients}\}} \\ & + \frac{1}{T_2^*\{\text{electric field noise}\}} + \frac{1}{T_2^*\{\text{magnetic field gradients}\}} + \frac{1}{T_2^*\{\text{temperature variation}\}} \\ & + \frac{1}{T_2^*\{\text{unknown}\}} + \frac{1}{2T_1},\end{aligned} \tag{2.7}$$

Where the $T_2^*\{X\}$ represents the hypothetical decoherence mechanism for T_2^*, $T_2^*\{\text{unknown}\}$ represents the decoherence mechanism which hasn't been included in this equation, and the part of $\frac{1}{2T_1}$ is

the fundamental limitation from spin-lattice coherence time T_1[91].

Hahn echo experimental protocol

As illustrated in Fig. 2.11, dephasing caused by static or slowly varying field over the first $\tau/2$ free evolution duration can be mitigated by applying a π pulse halfway through an additional $\tau/2$ free evolution interval[15]. In this way[92], the π pulse reverses the direction of spin precession, causing the phase accumulated due to static fields during the second half of the sequence to cancel out the phase accumulated during the first half. Consequently, spins in nonuniform fields rephase, generating a recovered signal known as a "spin echo", as shown in Fig. 2.11. The decay of this echo signal, resulting from field fluctuations during the measurement sequence, defines the spin coherence time T_2, also called the transverse or spin-spin relaxation time. In general, T_2 can exceed T_2^* by orders of magnitude. However, when the decoherence source isn't static over the free evolution, this reinforced mechanism will fail. In this case, more π pulses are needed to faster flip the spin against the fast fluctuation which is well-developed dynamical decoupling[93]. With the increased complexity of the MW pulse sequence, the MW pulse error would be accumulated, and the thermal effect of the MW device would be non-negligible, which also stimulates some improved dynamical decoupling protocols[93, 24]

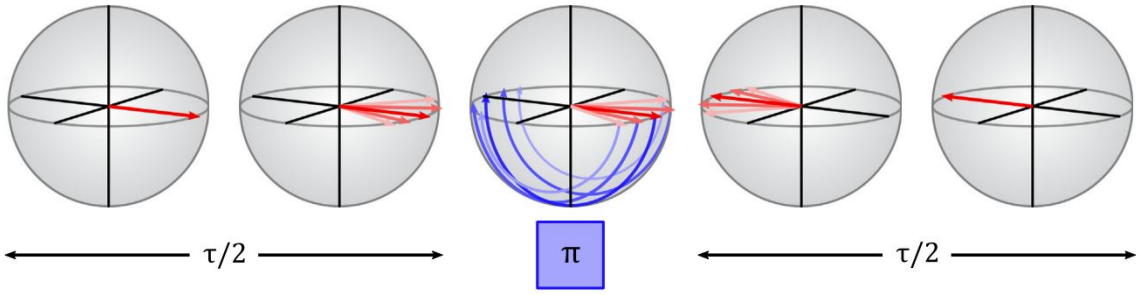

Figure 2.11. Recovery of spin phase coherence with central π pulse.

Spin-lattice relaxometry experimental protocol

In the spin-lattice relaxometry protocol, a green laser pulse initialises the quantum system, then a second laser pulse reads out the quantum state after the variable time interval until the quantum system loses the population information, as illustrated in Fig. 2.12(a).

As discussed in 1.2.1, the spin-lattice relaxation (or spin-phonon relaxation) is limited by interactions between electronic spin and phonons in the surrounding crystal lattice. Compared to

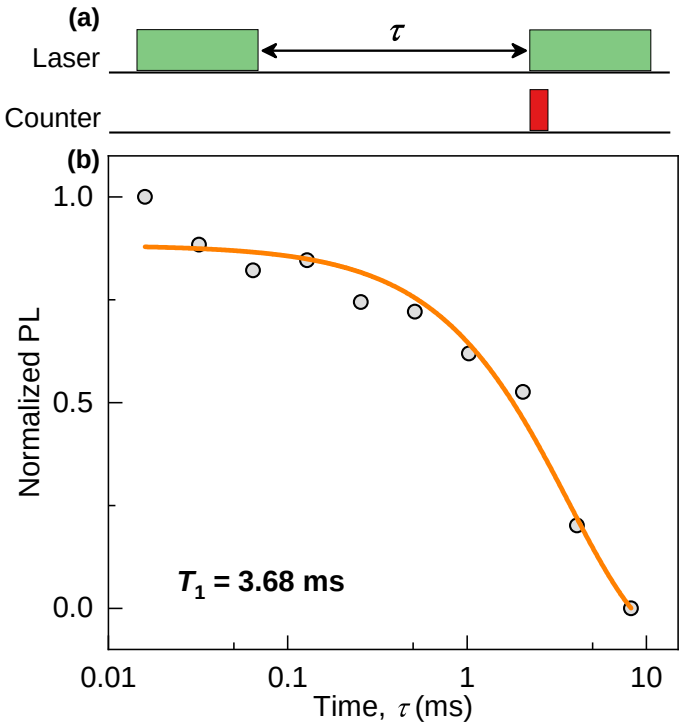

Figure 2.12. (a) Spin-lattice relazometry measurement sequence. (b) A typical spin-lattice relaxometry decay for the NVs in diamond. The grey points are the experimental raw data which is fitted by a single exponent decay equation (orange line).

group IV QEs, NVs feature less phonon coupling, exhibiting a much longer spin-lattice time (or longitudinal electron-spin relaxation time) $T_1 \sim 4\,\mathrm{ms}$ at room temperature as shown in Fig. 2.12(b).

Chapter 3

Laser-written waveguide-integrated coherent spins in diamond

3.1 Statement of authorship of paper(s) included in Chapter 3

Chapter 3 of the thesis is based on the following published paper: Yanzhao Guo, John P. Hadden, Federico Gorrini, Giulio Coccia, Vibhav Bharadwaj, Vinaya Kumar Kavatamane, Mohammad Sahnawaz Alam, Roberta Ramponi, Paul E. Barclay, Andrea Chiappini, Maurizio Ferrari, Alexander Kubanek, Angelo Bifone, Shane M. Eaton, and Anthony J. Bennett, "Laser-written waveguide-integrated coherent spins in diamond," APL Photonics 9, 076103 (2024).[94].

The corresponding author identified the following author contributions, using the CRediT Contributor Roles Taxonomy standard:

Yanzhao Guo: Conceptualization; Investigation; Methodology; Software; Writing – original draft; Writing – Review and editing. John P. Hadden: Conceptualization; Funding acquisition; Methodology; Supervision; Writing – Review and editing. Federico Gorrini: Validation; Writing – Review and editing. Giulio Coccia: Validation; Writing – Review and editing. Vibhav Bharadwaj: Investigation; Writing – Review and editing. Vinaya Kumar Kavatamane: Validation; Writing – Review and editing. Mohammad Sahnawaz Alam: Writing – Review and editing. Roberta Ramponi: Funding acquisition; Supervision; Writing – Review and editing. Paul E. Barclay: Supervision; Writing – Review and editing. Andrea Chiappini: Supervision; Writing - Review and editing. Maurizio Ferrari: Supervision; Writing – Review and editing. Alexander Kubanek: Funding acquisition; Supervision; Writing – Review and editing. Angelo Bifone: Funding acquisition; Resources; Supervision; Writing – Review and editing. Shane M. Eaton: Conceptualization; Funding acquisition; Methodology;

Resources; Supervision; Writing – Review and editing. Anthony J. Bennett: Conceptualization; Funding acquisition; Methodology; Supervision; Writing – Review and editing.

3.1.1 Highlight

QEs, such as the NVs in diamond, are attractive for quantum technologies such as nano-sensing, quantum information processing, and as a non-classical light source. However, it is still challenging to position individual emitters in photonic structures whilst preserving the spin coherence properties of the defect. In this paper, I investigate single and ensemble waveguide-integrated nitrogen-vacancy centres (WGINVs) in diamond fabricated by femtosecond laser writing followed by thermal annealing. Their spin coherence properties are systematically investigated and are shown to be comparable to native NVs in diamond. This method paves the way for the fabrication of coherent spins integrated within photonic devices.

3.2 Introduction

NVs in diamond are attractive for quantum technologies such as nano-sensing, quantum information processing, and as a non-classical light source. Although the spin coherence properties of NVs can reach up to microseconds at ambient temperature[95], the relatively low brightness and low DW factor hinder its application for quantum technologies[14]. Therefore, NVs are normally coupled into a photonic structure such as a SIL [96], nanopillar [97, 98], optical waveguide[99], or cavity[100] to improve their efficiency. However, due to diamond's extreme hardness and chemical resistance, conventional methods such as plasma etching[97], ion implantation[81], or focused-ion beam[96] have inevitably degraded their coherence and spectral properties.

Recently, femtosecond laser writing has emerged as a versatile approach for the creation of photonic circuits[81] with integrated quantum emitters. As femtosecond laser writing is a highly controllable fabrication process[101], it is a promising method for scalably preparing quantum emitters in wide bandgap semiconductors, such as diamond[81, 102, 103, 104, 105], hBN[106, 107] and SiC[108, 109]. In particular, laser-written NVs in diamond are of great interest due to the existence of mature and precise electron spin control protocols [15]. Compared with conventional approaches such as ion implantation[81], laser writing can place NVs deterministically [103, 110] and within photonic structures inscribed in the bulk of diamond[111, 112]. More recently, WGINVs have been demonstrated by femtosecond laser writing[113, 114, 111, 81]. However, there have been few studies on their spin coherence[104, 115], and even fewer on WGINVs. These studies are crucial if the system is to be used for quantum applications such as quantum information processing or remote sensing.

In this chapter, I characterize the spectral and spin coherence properties of single WGINVs in electronic grade (EG) CVD diamond and ensemble WGINVs in type Ib HPHT diamond, which are fabricated by femtosecond laser writing and subsequent thermal annealing. The home-built confocal ODMR setup described in 2.2.1 is used to coherently manipulate WGINVs, and characterize their spin coherence properties including the inhomogeneous dephasing time T_2^*, spin transverse relaxation time T_2 and longitudinal relaxation times T_1, via standard measurement protocols illustrated in 2.3.2 [15, 14]. Single WGINVs in type EG diamond show excellent single-photon purity, and spin coherence properties comparable to native NVs. Additionally, I demonstrate coherent coupling with nuclear spins which could be used as a register for a hybrid quantum photonic circuit. In the type Ib diamond, I demonstrate the creation of ensemble WGINVs with up to 900 times intensity enhancement compared to the pristine diamond, as a result of increased NV density. This all-optical fabrication process therefore provides a cost-effective way to prepare ensemble NVs and realize photonically-integrated quantum sensing devices based on economical type Ib diamond with sub $26\,\mathrm{nT}\cdot\mathrm{Hz}^{-1/2}$ DC magnetic field sensitivity.

3.3 Fabrication protocol for WGINVs

As shown in Fig. 3.1, the WGINVs were created by femtosecond laser writing and subsequent annealing in Politecnico di MILANO and the University of Turin. A commercial femtosecond laser (Menlo Systems BlueCut) that produces linearly polarised pulses with a wavelength of $515\,\mathrm{nm}$ (second harmonic), repetition rate of $500\,\mathrm{kHz}$ and a duration of $300\,\mathrm{fs}$ was used for femtosecond laser writing. The laser pulse was focused using an oil immersion objective lens (NA=1.25) with immersion oil refractive index $n_d = 1.515$ beneath the surface of synthetic diamond samples to write waveguides and NVs. The bulk diamond samples were mounted on precision translation stages for 3D control. The pulse energy was controlled using a combination of a motorized half-wave plate and a fixed linear polariser. The laser writing fabrication parameters are shown in Table 3.1. Annealing of the diamond samples was performed in a tubular horizontal furnace Lenton LTF15/50/450. The samples were placed in a quartz boat and covered with diamond grit to protect the surface. In order to purge the furnace chamber, oxygen was extracted using a diaphragm pump and a nitrogen flow for 1 h. Thermal treatments were carried out in a nitrogen atmosphere following three steps: first, the temperature was ramped from room temperature to 1000°C over the course of 3 hours and then kept at 1000°C for another 3 hours, and the furnace was finally switched off and allowed to cool down to room temperature.

Parallel modification lines separated by $13\,\mu\mathrm{m}$ were written to define the optical waveguides. These modification lines have dimensions of approximately $2\,\mu\mathrm{m}$ in width and $15\,\mu\mathrm{m}$ in height, and have previously been shown to contain amorphous, and graphitic carbon phases [113]. In the case of

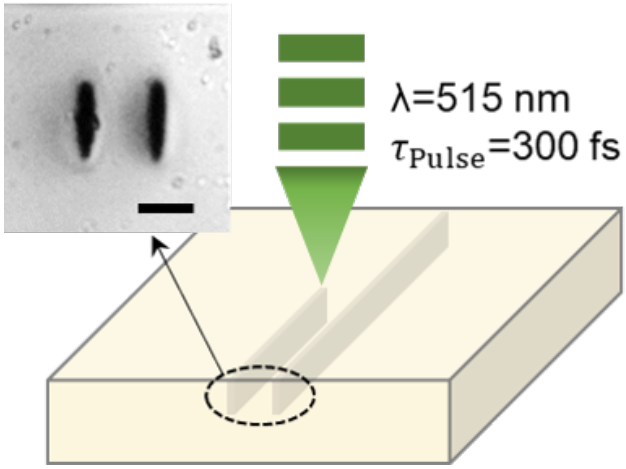

Figure 3.1. Laser writing waveguide schematic diagram, where the light yellow box is the diamond and the grey stripes are the modification lines. The insert in the left corner is the cross-section image of the laser-written waveguide, where the black scale bar represents 10 µm.

Table 3.1. Experimental parameters for laser fabrication

Diamond	Laser exposure	Scan speed (mm/s)	Pulse energy (nJ)	Depth (µm)
EG(WG)	500 kHz	0.5	60	35.0
EG(NVs)	single pulse	N/A	28	22.5
Ib (WG & NVs)	500 kHz	0.5	100	25.0

nitrogen-rich type Ib diamond samples, thermal annealing drives the diffusion of vacancies that were generated within the laser-modified sidewalls defining the optical waveguides. These vacancies are captured by substitutional nitrogen atoms to form ensemble WGINVs. Conversely, for lower nitrogen content type EG diamond, additional low energy static exposures were used to form vacancies localized near the centre of within the approximately cubic micrometre-sized laser focal volume, and well aligned with the centre of the previously laser-formed waveguides. Due to the lower background nitrogen, thermal annealing causes the diffusion of these vacancies which can yield single NVs near the centre of the waveguide cross-section. In this chapter, I used two static exposures to produce single NVs at different longitudinal positions along the waveguide, which I labelled single WGINV A and WGINV B. [111]

3.4 PL study on WGINVs

I use the confocal setup described in 2.2.1 to investigate the PL behavior of these WGINVs. A 532 nm and 650 nm optical filters are used to remove the laser reflection and Raman from the diamond substrate except for measuring the PL emission spectrum. In Fig. 3.2(a), the two bright strips are the waveguide modification lines which host a high density of laser-written vacancies[81].

Static single pulse exposures were observed to have formed isolated single WGINV A in the centre of the optical waveguide in type EG diamond, as shown in the top-down and cross-sectional PL map in Fig. 3.2(a), where $w_{x,y,z}$ are the Full Width at Half Maximum linewidth of x, y, z direction Gaussian fitting curves for single WGINV A and also represents the setup's optical resolution. The creation of NVs was confirmed by their PL emission spectrum with a $637\,\mathrm{nm}$ ZPL in Fig. 3.2(b). Moreover, as shown in Fig. 3.2(c), the $g^{(2)}(0) < 0.2$ indicates the single level of NVs, where $g^{(2)}(\tau)$ data is fitted by using the empirical equation [116, 82, 80, 117],

$$g^{(2)}(\tau) = 1 - C_1 e^{-|\tau|\cdot r_1} + \sum_{i=2}^{N} C_i e^{-|\tau|\cdot r_i} \tag{3.1}$$

with varying numbers of variables in the sum, denoted i. Here, r_1 is the antibunching rate, C_1 is the antibunching amplitude, r_i for $i \geq 2$ are bunching rates, and C_i for $i \geq 2$ are the corresponding bunching amplitudes. Then, the number of resolvable timescales, *N*, has been determined by calculating and comparing the reduced chi-squared statistic, r-square for each best-fit model. For this single WGINV A, *N*=3 gives the best-fitting results. The fitting parameters are shown in table 3.2.

Table 3.2. Fitting parameters of $g^{(2)}(\tau)$

Parameters	Value	Standard Error
τ_0 (ns)	0.275	0.012
C_1	1.481	0.011
τ_1 (ns)	9.48	0.12
C_2	0.365	0.061
τ_2 (ns)	114	17
C_3	0.313	0.067
τ_3 (ns)	312	29

Meanwhile, laser power-dependent PL saturation in Fig. 3.2(d) is obtained and fitted with

$$C(P) = \frac{C_{\mathrm{sat}} P}{P + P_{\mathrm{sat}}} \tag{3.2}$$

where *C(P)* is the steady-state PL rate as a function of power *P*, C_{sat} is the saturation PL rate and P_{sat} is the corresponding saturation power. Overall, the $g^{(2)}(0) < 0.2$ and power-dependent behaviour of this single NV indicate the quantized nature of its emission

As explained above, high-density ensembles of WGINVs are produced in type Ib diamond (Fig. 3.2(e)). I observe up to 900 times enhanced NV intensity in the waveguide relative to the pristine area in Fig. 3.2(e), revealing a corresponding NV density enhancement. Furthermore, the ensemble WGINVs density ρ is estimated to be $14\text{-}22\,\mathrm{ppb}$ in the waveguide region by taking the C_{ensemble} of $9.28\text{-}14.46\,\mathrm{MHz}$ in the y plot in Fig. 3.2(e) and C_{single} of $7.7\,\mathrm{kHz}$ in Fig. 3.2(d) under

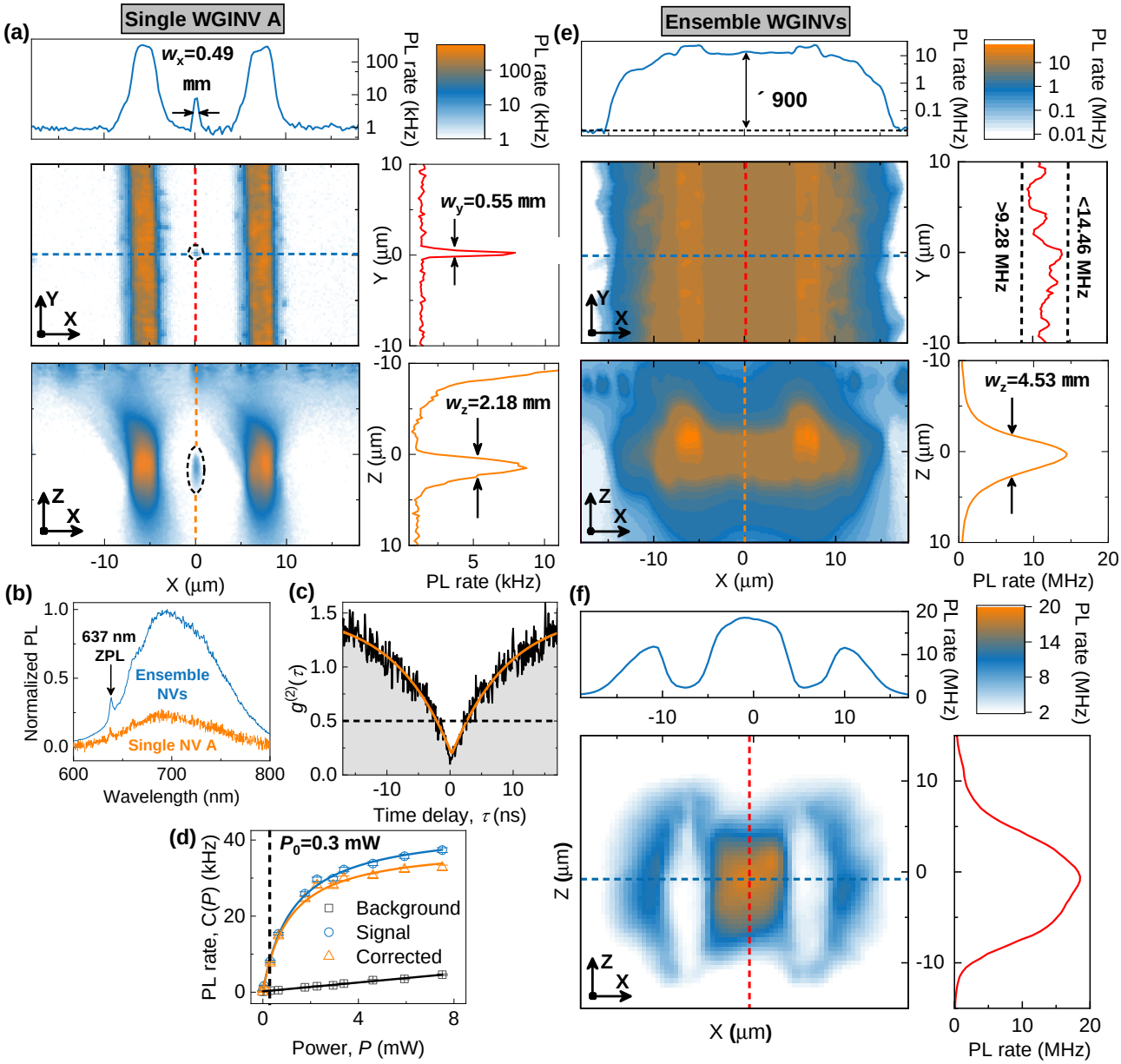

Figure 3.2. PL studies of laser-written WGINVs. (a) PL map of single WGINV A in type EG diamond, mapped from the z-direction (overhead) by scanning in x-y and x-z planes. The blue, red, and orange lines are slices along the dashed lines in (a), where $w_{x,y,z}$ are the Full Width at Half Maximum linewidth of x, y, z direction Gaussian fitting curves for single WGINV A (see high-resolution PL map in 3.3). (b) The emission spectrum of single WGINV A and ensemble NVs. (c) The PECS of single WGINV A, where the black line is raw data and the orange line represents the fitted curve. (d) The power-dependent PL rate for single WGINV A. The dashed line is the test laser power P_0 used for the density estimation of the ensemble WGINVs. (e) PL map of WGINVs in type Ib diamond, mapped from the z-direction (overhead) by scanning in x-y and x-z planes. (f) PL map of the WGINVs in type Ib diamond mapped from the y-direction (along the waveguide).

P_0 of $0.3\,\mathrm{mW}$. The z-slice plot of Fig. 3.2(e) displays a Gaussian variation of PL rate, at the same depth as the modification lines. Furthermore, its width of $4.53\,\mu\mathrm{m}$ is just a factor of 2 greater than the single WGINV in Fig. 3.2(a) which is itself limited by the Rayleigh range of the microscope. This indicates that the laser-formed WGINVs are well-confined in the core of the waveguide region, where I investigate the spin coherence properties of those ensemble WGINVs in Sec. 3.5.

To test the coupling between the ensemble WGINVs and waveguide in type Ib diamond, I scan the waveguide with excitation and collection along the waveguide direction, as shown in Fig. 3.2(f). Interestingly, I observe a stronger PL intensity in the waveguide region than in any other region, which is different from the cross-section PL map in Fig. 3.2(e). This suggests that the pump laser and PL intensity in the waveguide core are guided, being efficiently coupled into the optics enhancing the collected PL intensity. As a result, the green laser is guided to excite the ensemble NVs of the whole waveguide, resulting in stronger PL emission than that in top-down scanning in Fig. 3.2(e). Meanwhile, future experiments should collect PL emissions in another facet of the waveguide, as the side excitation and collection configuration shown in Chapter 2 and Chapter 4.

To estimate the ensemble WGINVs density in type Ib diamond, I compare a single WGINV A's PL intensity at power $P_0 = 0.3\,\mathrm{mW}$, which is much lower than its saturation power $1.10\,\mathrm{mW}$ in Fig. 3.2 (d). In this regime, the detected photon rate $C_{\mathsf{single}}(P)$ linearly scales with the laser power and is given by:

$$C_{\mathsf{single}}(P) = KP \tag{3.3}$$

where K is the linear scaling ratio between PL rate and laser power. I assume the ensemble of NVs in type Ib diamond to be inhomogeneously pumped due to the spatial Gaussian distribution of laser power. Therefore, I obtain the equation

$$C_{\mathsf{gaussian}}(P_0) = \iiint_V KP_0G(x)G(y)G(z)\rho dV, \tag{3.4a}$$

$$C_{\mathsf{gaussian}}(P_0) = C_{\mathsf{single}}(P_0)\rho A_x A_y A_z \tag{3.4b}$$

where the $G(x)$, $G(y)$, and $G(z)$ are the Gaussians fitted to the slices along the *x*, *y* and *z* in Fig. 3.3, $A_{x,y,z}$ are their corresponding integrals of the Gaussian fitting curves in Fig. 3.3. The ensemble NVs density ρ is estimated to be 14- 22 ppb in the waveguide region by taking the C_{ensemble} of 9.28-$14.46\,\mathrm{MHz}$ and C_{single} of $7.7\,\mathrm{kHz}$ under P_0 of $0.3\,\mathrm{mW}$. I assume the light is collected with equal intensity from all 4 allowed NV orientations in the ensemble. NVs density is also estimated at ρ = 0.024 ppb in the pristine region by taking the C_{ensemble} of $16.1\,\mathrm{kHz}$.

In contrast, I note that a more simplistic model of NV centre ensemble excitation which assumes the density to be uniform, could lead to an underestimate of NV density. For example, if I compare to a model which uses uniform excitation and collection from a spheroid with dimensions

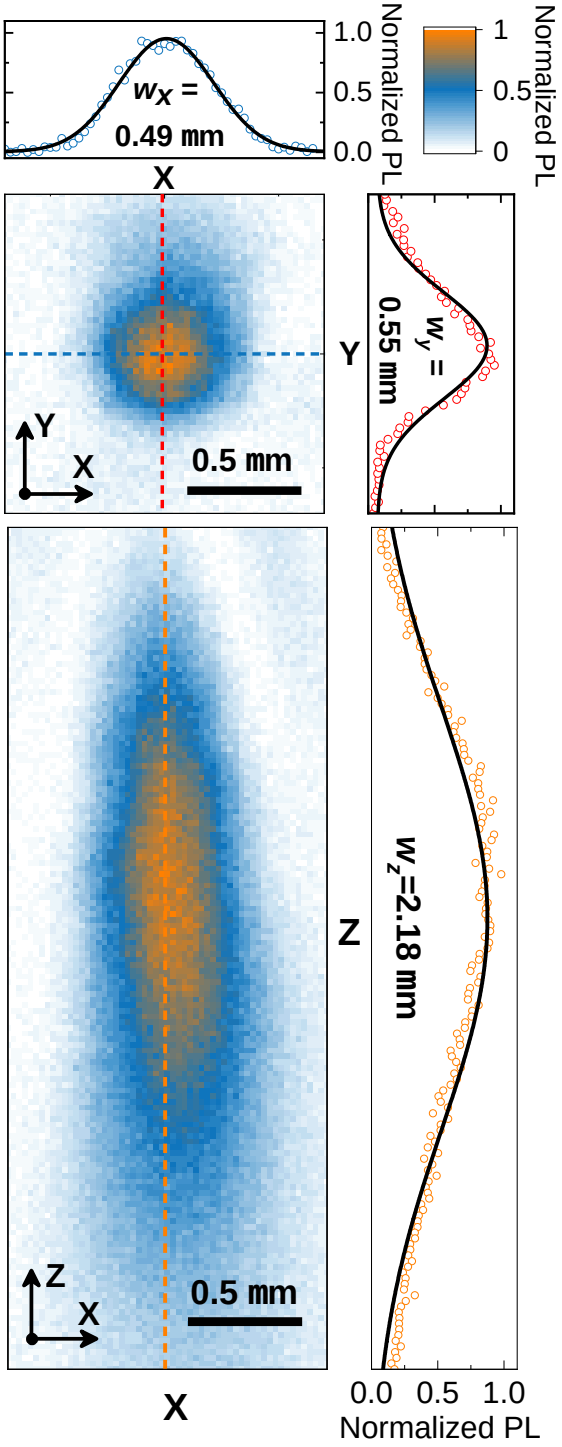

Figure 3.3. High-resolution confocal normalized PL image of single WGINVs A in type EG diamond where the blue, red, and orange data in the top and right plates are x, y, and z slices along the dashed lines in confocal PL image.

$w_{x,y,z}$ of the full width at half maximum linewidth of the confocal microscope's point spread function, I can obtain

$$C_{\text{uniform}}(P_0) = \iiint_V KP_0\rho dV, \tag{3.5a}$$

$$C_{\text{uniform}}(P_0) = C_{\text{single}}(P_0)\rho\frac{4\pi}{3}w_x w_y w_z \tag{3.5b}$$

In this case, there is an additional factor of $\frac{4\pi}{3} \sim 4$ compared to the corresponding integration of the three-dimensional Gaussian distribution. The non-uniform laser power distribution could also be considered to study the laser-induced inhomogeneous charge and spin initialisation dynamics of ensemble NVs, which is crucial for optimizing the ensemble-based quantum sensing protocol.

3.5 Coherence characterization of WGINVs

In this part, I systematically study the spin coherence properties of WGINVs in the frequency and time domains. A NV's ground state is governed by the Hamiltonian in the equation 1.9. The diagonalization of the NV ground state Hamiltonian yields an approximation of the spin resonance ($m_s = \pm 1$) frequencies[118] :

$$v_{\pm} = D + \xi \pm 2\Delta \tag{3.6}$$

where D=2.87 GHzis the axial zero field splitting parameter, the ξ describes the shift component which may be affected by temperature, transverse magnetic field, axial or hydrostatic strain, and axial electric fields. Meanwhile, Δ describes the splitting component which could originate from axial magnetic fields, non-axial or anisotropic strain, non-axial electric fields, and the nuclear hyperfine interaction. For ensembles of NVs, the effect of these external fields must be considered for each of the four possible orientations of NV[15].

3.5.1 Frequency domain ODMR spectrum

Overall, single WGINV A and single WGINV B in the type EG diamond and ensemble WGINVs in the type Ib diamond display a similar shape of zero-field CW-ODMR with three consistent features (first column of Fig. 3.4). First, they all show positive shift ξ of a few MHz compared to D. I attribute this to the compressive strain arising from laser-written modification lines providing a component of strain along the axis of the NV centre[36, 81]. Second, the lower resonance frequency exhibits slightly higher ODMR contrast due to the excitation with a linearly polarised MW magnetic

field on a mixed sublevel $m_s = \pm 1$ state split by non-axial or anisotropic strain[118, 81]. Third, two peaks are observed with the splitting Δ of a few MHz. Using a pulsed ODMR sequence, the resolution of the experiment is greatly improved, leading to more structure being resolved for both single WGINVs. For single WGINV A, the splitting Δ of 2.26 MHz in CW-ODMR and four resolvable resonance peaks in pulsed ODMR indicates the presence of nuclear ^{14}N interaction and non-axial or anisotropic strain in the waveguide region[119, 118, 37]. For single WGINV B, the splitting Δ of 3.87 MHz in CW-ODMR and 8 resolvable resonance peaks in pulsed ODMR implies that a complex combination of the non-axial or anisotropic strain and strong coupled nuclear ^{14}N and ^{13}C leads to splitting[120, 119].

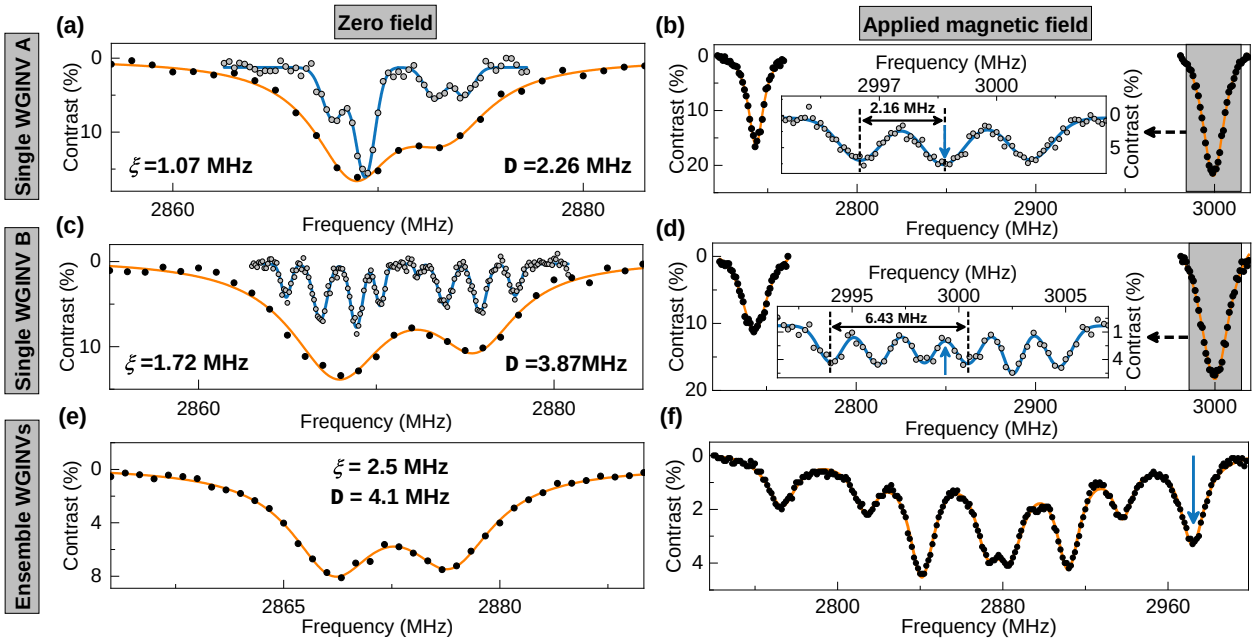

Figure 3.4. ODMR spectra of single WGINVs (first and second rows) and ensemble WGINVs (third row). (a), (c) and (e) are the zero-field ODMR and (b), (d) and (f) are the ODMR spectrum with the applied magnetic field. The black (grey) scatter points and orange (blue) lines are the raw data and corresponding fitted curves in the CW (pulsed) model ODMR. The inserts of (b) and (d) are the hyperfine structure of the grey regions in (b) and (d), respectively. Blue arrows represent the target frequencies used for the time domain ODMR measurements.

For the ensemble WGINVs in type Ib diamond I observe a positive shift ξ of 2.5 MHz, and a zero-field splitting Δ of 4.1 MHz. I note that in this regime the contributions from each of the four orientations of the NV centre ensemble cannot be individually resolved. However, the splitting, and shift of the combined signal are consistent with the expected compressive strain arising from the laser-written modification lines [114, 113], as well as some additional effects from the local electric field from over 200 ppm charge impurities [37].

To further lift the degeneracy of $m_s = \pm 1$ and quantify the hyperfine interaction strength

between NV electron spin and nearby strong coupling nuclear spins, a $4.6\,\mathrm{mT}$ magnetic field is applied for the single WGINVs in type EG diamond. The typical $2.16\,\mathrm{MHz}$ ^{14}N hyperfine splitting observed in pulsed ODMR[15] of single WGINV A is shown in grey data points in Fig. 3.4(b). For single WGINV B, I observed six anti-peaks in the insert of Fig. 3.4(d) revealing the $6.43\,\mathrm{MHz}$ ^{13}C coupling strength[121] in combination with $2.16\,\mathrm{MHz}$ ^{14}N hyperfine splitting. The fact that the nuclear hyperfine splitting is resolvable in both zero field and non-zero magnetic field ODMR, highlights the excellent coherence properties of NVs and their potential as quantum registers. For ensemble WGINVs in Ib, in Fig. 3.4(f), a $\sim 5.17\,\mathrm{mT}$ magnetic field is applied to lift the degeneracy of the $m_s = \pm 1$ transitions along the four NV orientations. The central frequencies marked with blue arrows in Figs. 3.4(b), (d), and (f) are now used for time domain measurements in Sec. 3.5.2.

Overall, these frequency domain ODMR of WGINVs are sensitive enough to probe the microscopic strain[81], the electric field, and the nuclear spin environment[120, 119]. Compared to previous Raman studies on these WGINVs[122], frequency domain ODMR is able to extract the strain vector. Regarding nuclear spin, the pulse ODMR exhibit $1\,\mathrm{MHz}$ linewidth, extracting the nitrogen unclear spin ($2.16\,\mathrm{MHz}$) and strong coupling carbon nuclear spin ($6.43\,\mathrm{MHz}$). The weak electric field and nuclear spin interaction ($<1\,\mathrm{MHz}$) are expected to be detected by the time domain ODMR with a design dynamical decoupling protocol[123].

3.5.2 Time domain ODMR spectrum

To get a deeper understanding of the coherence properties I have measured the T_2^*, T_2, and T_1 of WGINVs with standard protocols, shown at the top of Fig. 3.5. Due to the existence of strongly coupled nuclear spins the dynamics of the electron in single WGINV A and WGINV B are dominated by these hyperfine coupling frequencies. This results in beats being observed in Figs. 3.5(a) and (e) for single WGINV A and single WGINV B with Rabi frequency f_{Rabi} around $5.7\,\mathrm{MHz}$ and Rabi dephasing time $T_{\rho,\mathsf{Rabi}}$ around $4\,\mu\mathrm{s}$. In comparison, a Rabi frequency of $2.9\,\mathrm{MHz}$ coherently drives ensemble WGINVs in type Ib diamond with $T_{\rho,\mathsf{Rabi}}$ of $0.81\,\mu\mathrm{s}$ in Fig. 3.5(i). These Rabi frequencies are used for the following multi-pulse experiments.

The T_2^* of single WGINV A and WGINV B are around $1.5\,\mu\mathrm{s}$ from free induction decay (FID) measurements as shown in Figs. 3.5(b) and (f), which is limited by the naturally abundant isotopic ^{13}C bath[14, 15]. Moreover, there is one dominant oscillation of $2.16\,\mathrm{MHz}$ for single WGINV A in Fig. 3.5(b) and three frequencies of oscillation ($1.07\,\mathrm{MHz}$, $3.23\,\mathrm{MHz}$ and $5.4\,\mathrm{MHz}$) for single WGINV B in Fig. 3.4(f) which are clearly resolved in FID curves. This is consistent with the hyperfine structure of ^{14}N and strong coupling ^{13}C in Figs. 3.4(b) and (d). This indicates their excellent spin dephasing time and strong interaction between these spins. Regarding spin transverse relaxation time, both single WGINV A and single WGINV B exhibit the T_2 over $268\,\mu\mathrm{s}$ which is comparable

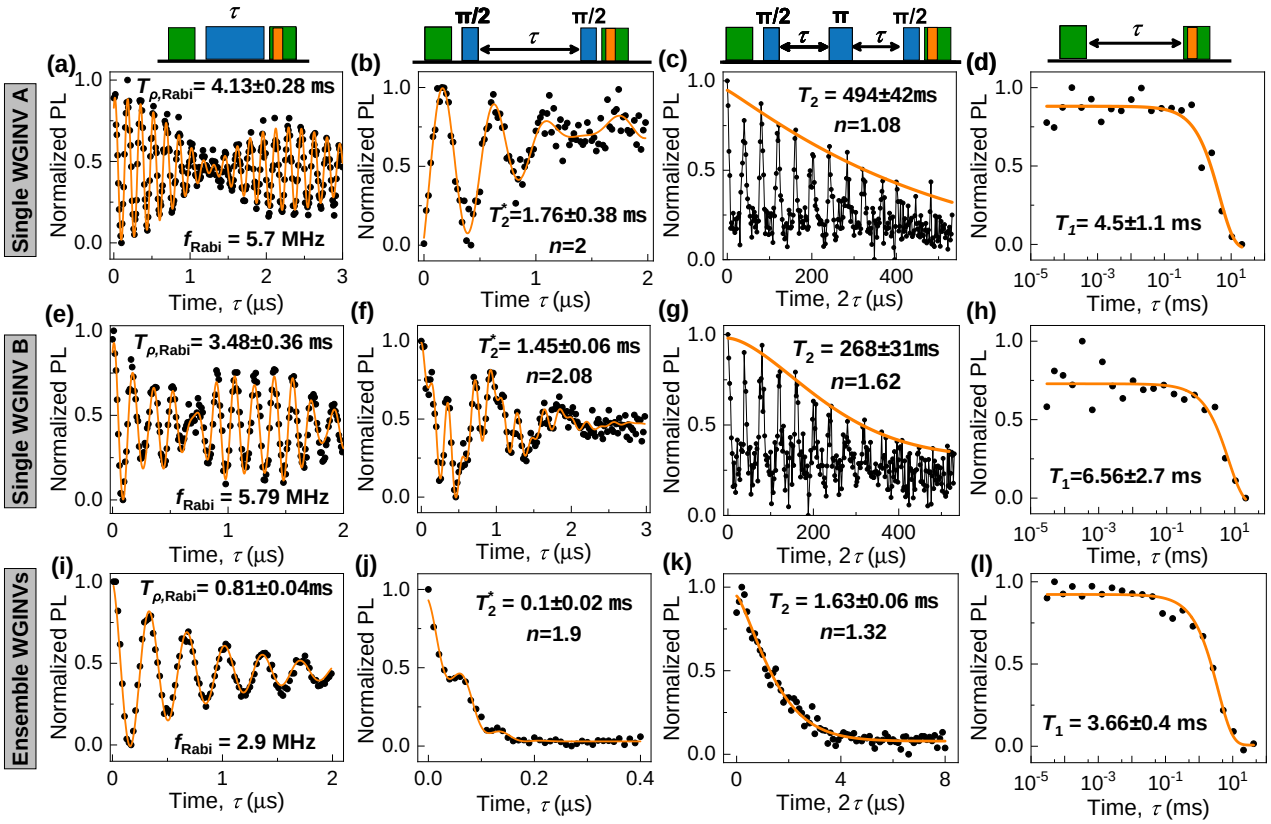

Figure 3.5. Time domain ODMR spectrum of single WGINVs in type EG diamond (from (a) to (h), first and second row) and ensemble WGINVs in type Ib diamond (from (i) to (l), third row). The first second, third, and fourth columns are Rabi, free induced decay (FID), Hahn echo, and relaxometry measurements, respectively. Meanwhile, their quantum control protocol is placed on the top of each column where the green, blue, and orange boxes represent laser and MW pulses, and the single photon detector gating window. The red curves are the fits to the raw data (black points). The envelopes of Rabi oscillation, FID, and Hahn echo data are fitted by equation, $e^{-\left(\frac{t}{T_i}\right)^n}$, to extract $T_{\rho,Rabi}$, T_2^* and T_2, where T_i is the corresponding coherence time, and n is the stretched exponent[124, 15, 125]. The T_1 is obtained by fitting the single exponent decay equation. I state that some fitting parameters are pre-defined by the previous frequency domain ODMR in Fig. 3.4 to process the fitting, for example, the hyperfine interaction relation to the detuning oscillations. The successful fitting will be justified by convergence with less than 200 Levenberg Marquardt iterations in Origin.

with native single NV in type EG diamond. The collapse and revival behaviour in both single WGINV A and WGINV B match the spin bath Larmor precession frequency ($50\,\mathrm{kHz}$) in the Hahn echo curve, which indicates that the ^{13}C spin bath is the dominant decoherence source. In this case, as shown in Fig. 3.5, T_2 values are obtained by only fitting the peak points in every collapse and revival cycle until collapse and revival behaviours fully vanish. Moreover, I highlight that for single WGINV A, T_2 of $494\,\mu\mathrm{s}$ is longer than most of NVs integrated into photonics structures[126, 127, 128]. For example, Luozhou Li et al characterised the T_2=$230\,\mu\mathrm{s}$ of NVs in a nanocavity[126], Paolo Andrich et al. reported the NVs in Engineered Micro- and Nanoscale Diamonds feature $360\,\mu\mathrm{s}$ of T_2[127] , and Elke Neu et al fabricated the NVs in a nanopillar on (111)-oriented diamond with T_2=$235\,\mu\mathrm{s}$[128]. Although single WGINV B has a slightly shorter T_2 of $268\,\mu\mathrm{s}$, the interaction of electron and strong coupling ^{13}C nuclear spin could be used as a quantum memory register[24, 129]. Finally, in Figs. 3.5(d) and (h), both single WGINV A and WGINV B display T_1 over $4.5\,\mathrm{ms}$ as the native single NV in type EG diamond[130].

Although the $0.1\,\mu\mathrm{s}$ T_2^* of ensemble WGINVs is nearly 10 times shorter than single WGINVs due to its inhomogeneous electron spin environment (Fig. 3.5(j)), the value of its coherence time is still consistent with those of native NVs in type Ib diamond[14]. The transverse magnetic field has an impact on the ensemble NVs[131], a T_2 of $1.63\,\mu\mathrm{s}$ is obtained which is comparable with singe NV's coherence properties in type Ib diamond, and mainly limited by the nitrogen electronic spin bath (P1 centres)[15]. Moreover, the T_1 curves of ensemble NVs do not show any obvious decay within $1\,\mathrm{ms}$, which is comparable with the relaxometry performance of native NVs[130, 14]. Therefore, it indeed proves that the laser writing process produces ensemble WGINVs in the waveguide region without compromising their spin coherence properties.

I note the Rabi dephasing time $T_{\rho,\mathsf{Rabi}}$ of single WGINVs could be extended to over $10\,\mu\mathrm{s}$ by reducing the MW power broadening with a Rabi frequency under $1\,\mathrm{MHz}$ as shown in 3.6.

3.5.3 Sensitivity for WGINVs

By taking the PL rate C $\sim$$30\,\mathrm{kHz}$, ODMR contrast $\Lambda \sim 20\%$, readout duration time t_L $\sim$$0.5\,\mu\mathrm{s}$, T_2^* of $1.76\,\mu\mathrm{s}$, and T_2 of $494\,\mu\mathrm{s}$ for single WGINV A, its photon-shot-noise-limited DC (η_{dc}) and AC (η_{ac}) magnetic field sensitivity are estimated around 174.9$\pm$ $17.5\,\mathrm{nT}\cdot\mathrm{Hz}^{-1/2}$ and 10.4$\pm$$0.5\,\mathrm{nT}\cdot\mathrm{Hz}^{-1/2}$, in the pulsed mode measurement by equations[14],

$$\eta_{\mathsf{dc}} \sim \frac{\hbar}{g\mu_B}\frac{1}{\Lambda\sqrt{Ct_L}} \times \frac{1}{\sqrt{T_2^*}} \tag{3.7}$$

$$\eta_{\mathsf{ac}} = \eta_{\mathsf{dc}}\sqrt{\frac{T_2^*}{T_2}}, \tag{3.8}$$

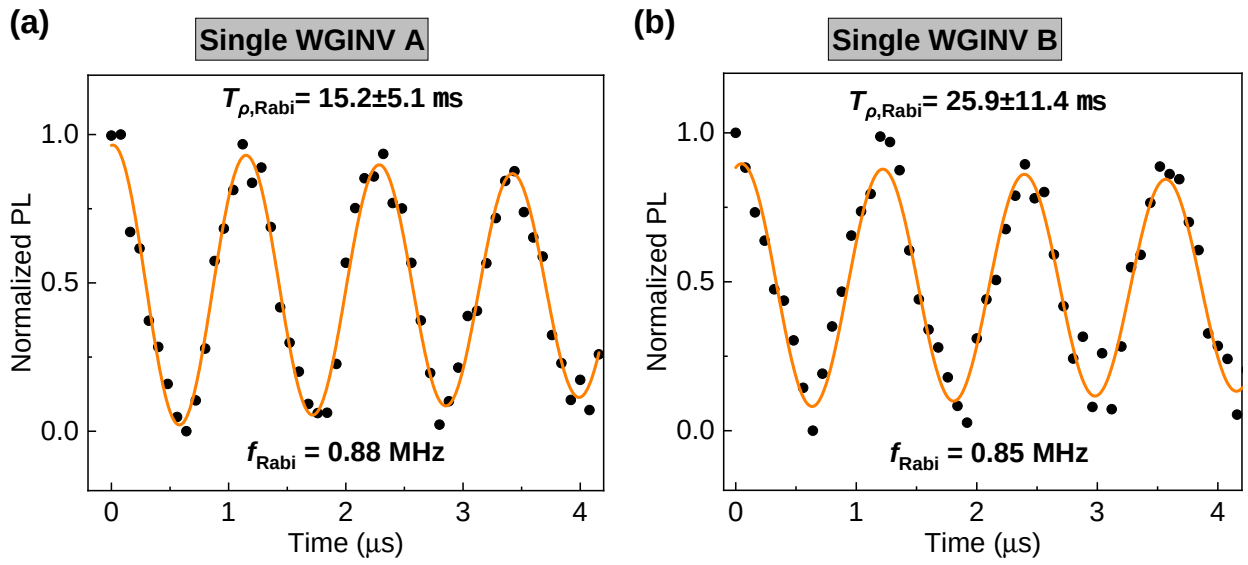

Figure 3.6. Rabi oscillations for single WGINV A (a) and single WGINV B (b) at weak MW power.

respectively. The $g \sim 2.0$ is the Landé g-factor, μ_B is the Bohr magneton, and $\hbar$ is the reduced Planck constant.

For ensemble WGINVs in type Ib diamond, the η_{dc} and η_{ac} are estimated around $25.7\pm2.6\,\text{nT}\cdot\text{Hz}^{-1/2}$ and $6.6\pm0.1\,\text{nT}\cdot\text{Hz}^{-1/2}$, by taking readout duration time t_L $\sim0.5\,\mu\text{s}$, T_2^* of $0.1\,\mu\text{s}$, T_2 of $1.53\,\mu\text{s}$, the PL rate C_{ensemble} $\sim0.9\,\text{GHz}$, and ODMR contrast $\Lambda \sim 3.3\%$ for the external peak (marked by blue arrow) in Fig. 3.4(f). I note that the PL rate of the ensemble WGINVs used here was not at saturation. Therefore, the sensitivity could be improved by increased laser power excitation or by increasing the number of NV centres probed through excitation and collection via the waveguide mode as I will discuss in the Chapter 4. Moreover, there are also some ways to improve the sensitivity. For example, single NV are able to achieve sub $\text{nT}\cdot\text{Hz}^{-1/2}$ by optimizing the sensing protocol[132], such as reducing the overhead time, dynamical decoupling with shaped pulses, and improving readout fidelity. And the ensemble NVs could further be improved by order magnitudes via multiple integrated hybrid sensing devices to realize the sensitivity of $\text{fT}\cdot\text{Hz}^{-1/2}$[133].

3.6 Conclusion and outlook

Laser-written coherent single WGINVs in type EG diamond and ensemble WGINVs in type Ib diamond has been investigated via standard ODMR protocol. The density of ensemble WGINVs in the type Ib diamond sample was estimated to be 14-22 ppb. The spin coherence properties of the WGINVs were similar to that of the native NVs as evidenced by the summary in Table 3.3, further

demonstrating the promise of laser writing to realize an integrated photonics platform incorporating quantum emitters.

Table 3.3. Comparison of native NVs from L. Rondin et al's [14] and our work.

Diamond type	EG native	EG WGINV A	Ib native	Ib WGINVs
Synthesis	CVD	CVD	HPHT	HPHT
N	< 5 ppb	< 5 ppb	200 ppm	200 ppm
NV	Single[a]	Single[a]	Single[a]	14-22 ppb
T_2^* (µs)	3	1.76	0.1	0.1
T_2 (µs)	300	494	1	1.63
$\eta_{\mathrm{dc}}\left(\mathrm{nT}\cdot\mathrm{Hz}^{-1/2}\right)$	300	174.9	1500	25.7
$\eta_{\mathrm{ac}}\left(\mathrm{nT}\cdot\mathrm{Hz}^{-1/2}\right)$	30	10.4	500	6.6

[a]The single means a single NV defect exhibiting single photon emission.

These highly coherent single WGINVs couple to nearby nuclear spins with excellent coherence which could be used as a quantum register within photonic integrated circuits. NV features spin-photon interference to establish entanglement between stationary spin qubits and flying photon qubits. The coupled nuclear could swap the entanglement information from the NV electron spin and store the information for a longer time[24, 129]. Moreover, this robust multiplies qubit system with electron spin qubit and unclear spin qubits could also provide a room temperature quantum platform for the quantum simulation applications to study the fundamental physics[134, 135, 136, 137]. In terms of ensemble WGINVs, this all-optical fabrication technique paves the way for a cost-effective waveguide-integrated quantum sensing device based on the more economical type Ib diamond. Future work will focus on the optimization of the NV creation process, including the annealing and laser writing processes, to further increase the NV density and reduce the non-NV spin noise. For example, the different depths and scan speeds of the laser beam could potentially affect the NV yield. The CVD diamond with different native nitrogen concentrations should also be interesting in implementing the laser writing to create ensemble WGINVs with better spin coherence properties. Another interesting thing is to fabricate other useful photonics-integrated NVs. Meanwhile, a further plan is to investigate their NVs' creation yield and quantum properties, such as optical and spin coherence. Last but not least, the method used in this chapter could also be used for other QEs in semiconductors, such as group IV QEs in diamond and QEs in nitride semiconductors.

Chapter 4

Enhanced quantum magnetometry with a laser-written integrated photonic diamond chip

4.1 Statement of authorship of paper included in Chapter 4

Chapter 4 of the thesis is based on the following paper: Yanzhao Guo, Giulio Coccia, Vinaya Kumar Kavatamane, Argyro N. Giakoumaki, Anton N. Vetlugin, Roberta Ramponi, Cesare Soci, Paul E. Barclay, John P. Hadden, Anthony J. Bennett, and Shane M. Eaton, "Enhanced quantum magnetometry with a laser-written integrated photonic diamond chip", arXiv:2502.02478.

The corresponding author identified the following author contributions, using the CRediT Contributor Roles Taxonomy standard:

Yanzhao Guo: Conceptualization; Methodology; Software; Data curation; Investigation; Writing - Original Draft, Writing - Review & Editing. Giulio Coccia: Resources; Writing - Review & Editing. Vinaya Kumar Kavatamane: Resources; Writing - Review & Editing. Argyro N. Giakoumaki: Resources; Writing - Review & Editing. Anton N. Vetlugin: Resources; Writing - Review & Editing. Roberta Ramponi: Writing - Review & Editing; Supervision; Funding Acquisition. Cesare Soci; Resources; Writing - Review & Editing; Supervision. Paul E. Barclay: Resources; Writing - Review & Editing; Supervision. John P. Hadden: Conceptualization; Writing - Review & Editing; Supervision; Funding Acquisition. Anthony J. Bennett: Conceptualization; Writing - Review & Editing; Supervision, Funding Acquisition. Shane M. Eaton: Conceptualization; Writing - Review & Editing; Supervision; Funding Acquisition.

4.1.1 Highlight

An ensemble of NVs in diamond can act as a precise quantum sensor even at room temperature. However, to optimize the sensitivity of any device it is crucial to increase the number of spins sampled, maximize their coupling to the detection system, and not degrade their spin properties. In this chapter, I demonstrate enhanced quantum magnetometry via a high-quality buried II-type laser-written waveguide in diamond with a 4.5 ppm density of NVs. I show that the waveguide-coupled NVs exhibit comparable spin coherence properties as that of NVs in pristine diamond using pulsed ODMR spectroscopy. Waveguide-enhanced magnetic field sensing is demonstrated in a fibre-coupled integrated photonics chip, showing a 10-fold enhanced sensitivity relative to conventional confocal configuration, paving a promising way for NVs ensemble-based microscale sensing.

4.2 Introduction

Quantum sensing based on NVs in diamond has achieved remarkable progress in the last two decades. Due to its asymmetric atomic structure[34], NVs are highly sensitive to weak external influences like temperature[35], pressure[36, 37], electric field[38] and magnetic field [14, 39]. Meanwhile, their long spin coherence time allows single NV-based quantum sensors to achieve good sensitivity ($\mathrm{nT} \cdot \mathrm{Hz}^{-1/2}$ to $\mu\mathrm{T} \cdot \mathrm{Hz}^{-1/2}$)[95] and high-resolution (nm) sensing[39, 14]. However, given that the sensitivity scales inversely with the square root of detected signal intensity[15, 14], NVs ensemble-based sensing protocol is expected to achieve $\mathrm{pT} \cdot \mathrm{Hz}^{-1/2}$ for real-life applications [14, 15]. The NVs ensemble-based sensing protocol would bring the challenge of homogeneous excitation, manipulation, and readout. Thus, it is crucial to efficiently excite and collect from a large volume of ensemble NVs with good spin coherence properties[15]. Previous work on NVs ensemble-based magnetometers reported that a light-trapping diamond waveguide geometry[138] can improve the optical depth of a mm-sized sensor to enhance the exciting efficiency. Another solution could be to couple an ensemble of NVs into the fibre-integrated photonic structure, with micron-scale sensing resolution and improved efficiency [139]. Thus, a high-quality integrated device for ensemble NVs is crucial for sensitivity improvement.

As mentioned in the Chapter 3, the highly coherent WGINVs can be created by relying on a two-step fabrication of WGINVs through laser writing followed by annealing. However, to achieve a robust laser-written device with optimal performance, it would be more attractive to use a single direct laser fabrication step. This method is particularly suitable for a diamond substrate containing a high density of native NVs.

In this chapter, I demonstrate an enhanced quantum sensing platform via a high-quality

buried II-type laser-written waveguide in DNV-B14 diamond with a 4.5 ppm density of NVs. I show that the waveguide-coupled NVs exhibit comparable coherence properties to NVs in pristine diamond through pulsed ODMR spectroscopy. A fibre-to-waveguide-to-fibre setup (see 2.2.2) is built to efficiently harness the large volume of NVs along the whole waveguide, showing 10-fold enhanced sensitivity than conventional confocal configuration, paving a promising way for NVs ensemble-based microscale sensing.

4.3 Direct laser writing fabrication protocol

The laser writing of optical waveguides in the DNV-B14 diamond sample is studied in Fig. 4.1(a). The sample information is detailed in 2.1.1. In Politecnico di MILANO, Optical waveguides were written by scanning laser pulses of $515\,\mathrm{nm}$ wavelength, $300\,\mathrm{fs}$ pulse duration, $500\,\mathrm{kHz}$ pulse duration across the sample using a 1.25 NA oil immersion objective, $0.5\,\mathrm{m/s}$ scan speed, $18\,\mu\mathrm{m}$ in-depth and $13\,\mu\mathrm{m}$ separation between waveguide sidewalls. From left to right of Fig. 4.1(b), four waveguides are fabricated with powers of 20, 30, 40, and 50 mW, where the overlaid mode profile in cross-sectional (lower plate) optical microscopy image is the waveguide mode of $635\,\mathrm{nm}$ test laser. The detailed profile parameters are demonstrated in Table 4.1. Basically, as the fabrication laser power increased, I observed the decreasing profile and improving the insertion loss. The insertion loss includes the scattering in the imperfect sidewall, fibre-waveguide coupling efficiency and intrinsic loss of the diamond sample which is evaluated by the UV-Via-NIR transmission spectrum in Fig. 4.1(c). In particular, the waveguide written with $40\,\mathrm{mW}$ features less than $-12\,\mathrm{dB}$ per $2.8\,\mathrm{mm}$ transmission loss and around $5\,\mu\mathrm{m}$ of mode profile diameter via $635\,\mathrm{nm}$ probe laser, which is further investigated its spin coherence and spectral properties in this chapter. I note that due to the high NV density in the pristine diamond, there is no following annealing after the laser writing fabrication.

Table 4.1. Insertion loss at $635\,\mathrm{nm}$ for waveguide

Power (mW)	Insertion loss (dB)	Mode size x (μm)	Mode size y (μm)
20	14.15	5.48	6.03
30	12.07	4.3	6.21
40	11.6	4.83	5.47
50	11.58	4.15	4.86

4.4 PL study

I used the home-build ODMR confocal setup (see 2.2.1) with the green laser excitation, as shown in Fig. 4.1(d), to characterize the waveguide's spectral and spin coherence properties.

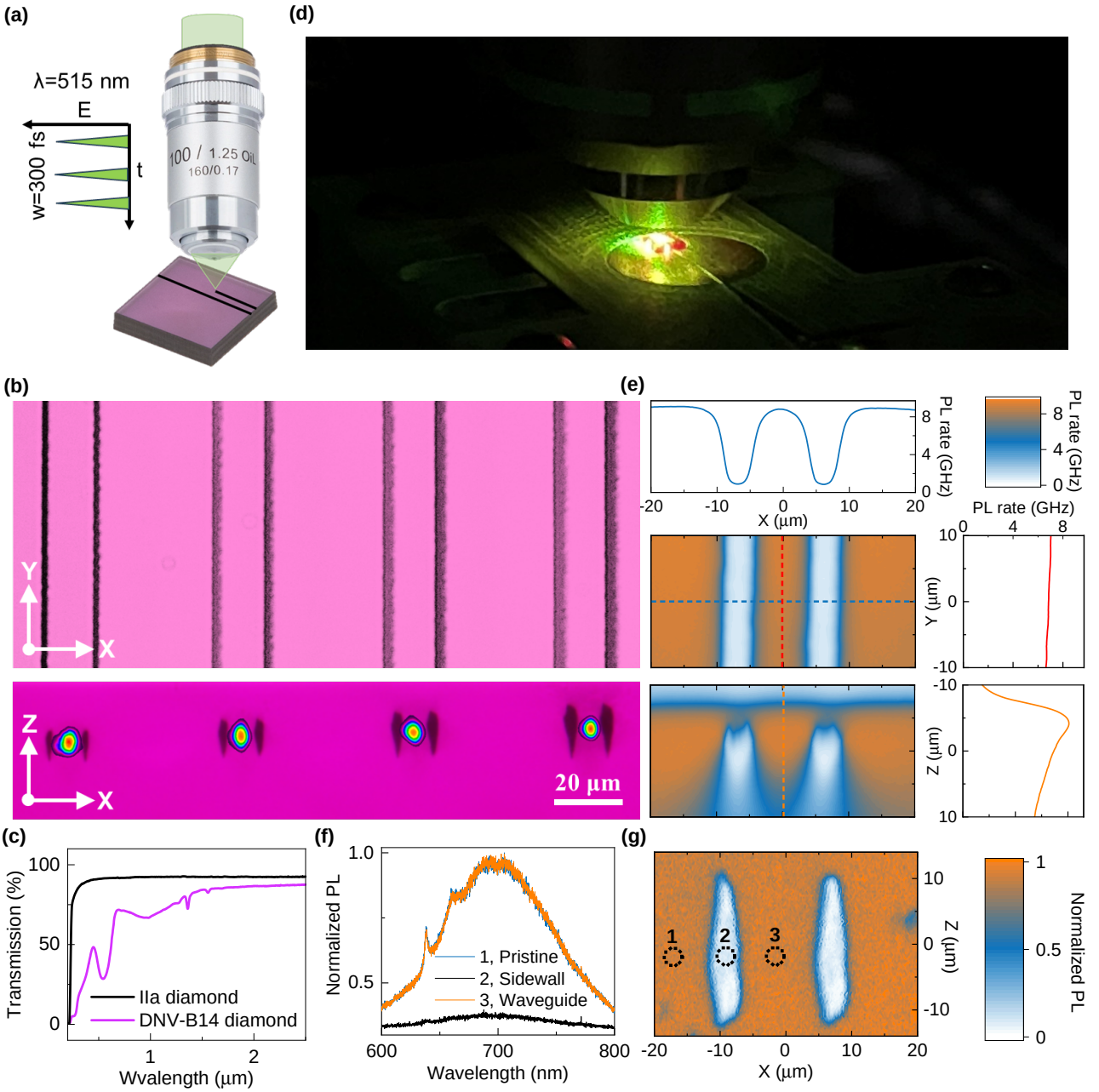

Figure 4.1. (a) The schematic diagram for the laser-written integrated photonics diamond chip (b) Overhead (upper plate) and cross-sectional (lower plate) optical microscopy images of waveguides with overlaid 635 nm mode profile. (c) UV-Vis-NIR transmission spectra for pristine DNV-B14 diamond and IIa diamond. (d) The photo of the DNV-B14 sample under green laser illumination. (e) The confocal PL maps of the waveguide were written with a 40 mW femtosecond laser, mapped from the z-direction (overhead) by scanning in x-y and x-z planes. (g) The confocal PL map of the WGINVs was written with a 40 mW femtosecond laser, mapped from the y-direction (along the waveguide). (f) PL emission spectrum for the pristine, waveguide, and sidewall region in waveguide written with a 40 mW femtosecond laser.

The setup details are in the section 2.2.1. A $532\,\mathrm{nm}$ and $650\,\mathrm{nm}$ optical filters are used to remove the laser reflection and Raman from the diamond substrate except for measuring the PL emission spectrum. In Fig. 4.1(e), the two dark strips are the waveguide modification lines which host a high density of laser-formed damage instead of NVs in the upper plates of Fig. 4.1(e). In the cross-sectional view (lower plates), there is a measurement artefact below the sidewalls because they are strongly absorbing and scattering so as the laser moves through them, there is a reduction in the signal. To avoid this issue, in Fig. 4.1(g), measuring the sample from its facet edge, and end on, I directly map the waveguide cross-section, which resolves three regions labelled as 1-pristine, 2-sidewall, and 3-waveguide regions. In Fig. 4.1(f), the spectra of 1-pristine and 3-waveguide areas feature similar spectral properties with a clear $637\,\mathrm{nm}$ ZPL and broad PSB extending to almost $800\,\mathrm{nm}$. The PL intensity was reduced in the sidewall areas by its hosting graphitized and amorphous carbon from laser-written waveguide modification lines[81]. Notably, the identical PL intensity and spectra in pristine and waveguide regions indicate the laser writing process preserves the excellent PL emission properties as the pristine regime.

4.5 Spin coherence characterization

The frequency domain ODMR is used to characterize the microscopic local environment of NVs in pristine and waveguide regions. As discussed in the equation 3.6 in Chapter 3, the spin resonance ($m_s = \pm 1$) frequency is obtained by axial zero-field splitting parameter D, shift component ξ and splitting component Δ which are sensitive to the external environment. In Fig. 4.2(a), the zero-field CW-ODMR shows a less than $0.3\,\mathrm{MHz}$ shift component ξ for both the pristine and waveguide regions. There is a $\sim 3\,\mathrm{MHz}$ of splitting component Δ observed in the pristine and waveguide regions which arise from the local strain and electric field in the diamond crystal. In contrast, the broader linewidth (w_1=$6.2\,\mathrm{MHz}$ and w_2=$7.8\,\mathrm{MHz}$) of the $m_s = \pm 1$ resonance peaks in the waveguide region are found compared to the w_1=$5.7\,\mathrm{MHz}$ and w_2=$7.2\,\mathrm{MHz}$ observed in the pristine region. This indicates the increased non-hydrostatic strain induced by the laser-written fabrication process, which is consistent with previous studies [81]. A $5\,\mathrm{mT}$ magnetic field is applied to lift the degeneracy of the $m_s = \pm 1$ transitions along the four NV orientations in Fig. 4.2(b). The highest frequency transition is further investigated with pulsed ODMR in Fig. 4.2(c), where the typical $2.16\,\mathrm{MHz}$ ^{14}N hyperfine splitting is resolved, suggesting the good coherence properties.

I have measured the Rabi oscillation, FID, Hahn echo, and spin-lattice relaxometry of ensemble NVs in pristine and waveguide regions with standard protocols in Fig. 4.2(d-g). The detailed experiment protocols are illustrated in 2.3.2. Surprisingly, the NV ensembles in both regions are shown to have comparable spin coherence times of $\sim 1\,\mu\mathrm{s}$ for $T_{\rho,\mathrm{Rabi}}$, $\sim 500\,\mathrm{ns}$ for T_2^*, $\sim 5\,\mu\mathrm{s}$ for T_2, and $\sim 5\,\mathrm{ms}$ for T_1. This implies that laser writing fabrication does not degrade the spin

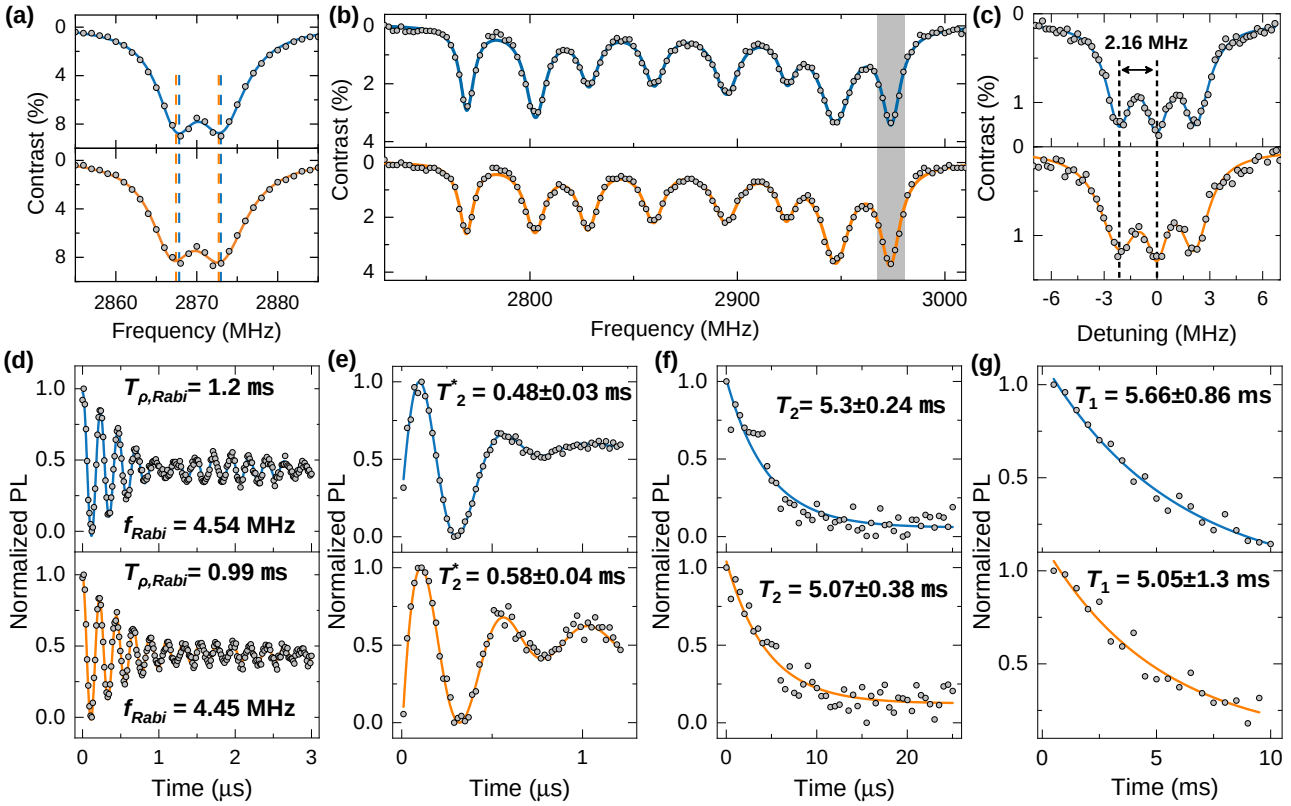

Figure 4.2. Spin coherence properties of an ensemble of NVs in the pristine and waveguide regions where the upper plates are for NVs in the pristine region and lower plates are for the NVs in the waveguide region. (a) Zero-field CW-ODMR. (b) CW-ODMR with the applied magnetic field. (c) Pulsed ODMR for the highest resonance transition in (b). (d), (e) (f), and (g) are the Rabi oscillation, FID, Hahn echo, and lattice relaxometry measurements, respectively. The grey points are the experimental data, and the blue and orange lines are fitting curves.

coherence properties. This should be contrasted with other fabrication methods such as plasma etching [97] and focused-ion beam[96], which have a detrimental effect on these parameters[15].

4.6 Magnetometry via fibre to waveguide to fibre configuration

Compared to the conventional free space confocal setup for limited numbers of NV, a fibre-waveguide-fibre configuration was used for high-density ensemble waveguide integrated NVs in Fig. 4.3(a). Two SMF-28 single-mode fibres were used to couple to opposing facets to probe NV along the entire waveguide efficiently. The input fibre delivers green laser excitation and collects the backward-travelling red fluorescence from the NVs in the waveguide, which is filtered with a dichroic splitter and directed to a first detector. The second fibre solely collects the forward-travelling red fluorescence from the waveguide and directs it to a second detector. The detailed information on the fibre-to-waveguide-to-fibre setup see the section 2.2.2 in the Chapter 2.

Fig. 4.3(a) is the zero-field ODMR recorded using the backward reflection and forward transmitted travelling PL emission from the chip. Their splitting components Δ are $5.4\,\mathrm{MHz}$ and $6.7\,\mathrm{MHz}$, respectively, which is larger than the results in the confocal configuration in Fig. 4.2(a). This implies the average effect of the strain-induced and electric field splitting for the ensemble NVs along the whole waveguide region which is consistent with the previous results [139]. Moreover, the over 10% ODMR contrast suggests an excellent ODMR response potentially leading to high sensitivity. I also observed a robust ODMR response with the applied magnetic field in Fig. 4.3(b) via using the backward reflection and forward transmitted travelling PL emission from the chip. Eight resonance peaks resulting from the four different NV orientations have been clearly resolved. The ODMR contrast of the highest frequency peak in the ODMR spectrum is over 3%, comparable to the confocal ODMR results. Meanwhile, there are also some resonance frequency shifts between backward and forward ODMR. This potentially could be used to demonstrate the magnetic field gradient along the waveguide direction, where the detailed gradient characterization would be beyond the regime of paper. Moreover, due to the magnetic field projection along four crystalline NVs <111> orientations[140], I rebuilt magnetic field vectors B_1 and B_2 in Fig. 4.3(c) solely via the forward transmission PL. I note the magnetic field vector in lab coordinates can be defined by the excitation polarisation plot for four differently oriented NVs[141, 142]. The magnetic field is calculated by the Zeeman effect via the equation[14],

$$\nu_{\pm}(B_i) = D \pm \sqrt{(\frac{g\mu_B}{h}B_i)^2 + \Delta^2}$$

, where B_i is the magnetic field projection along four different NV orientations, $\nu_{\pm}(B_i)$ is the ODMR resonance frequency for different Zeeman splitting from four different NV orientations, the $g \sim 2.0$ is the Landé g-factor, μ_B is the Bohr magneton, and h is the Planck constant.

I also studied the MW and laser power effect on the CW-ODMR spectrum. In confocal microscopy, the laser power and MW power greatly impact the ODMR shape due to the non-negligible power broadening. In the fiber-waveguide-fiber configuration, from Fig. 4.4 the laser excitation power appears to play less role than the microwave in the ODMR spectrum recorded by forward and backward traveling PL. This mechanism is interesting and ought to be demonstrated in future studies.

4.7 Enhanced sensitivity

As discussed in 3.5.3, the intrinsic sensitivity is not only dependent on the strong response to the target signal but also on avoiding interactions with undesirable noise. In this chapter, the T_2^* is $0.5\,\mu\mathrm{s}$ and T_2 is $5\,\mu\mathrm{s}$, where the spin coherence properties of the WGINVs are consistent with

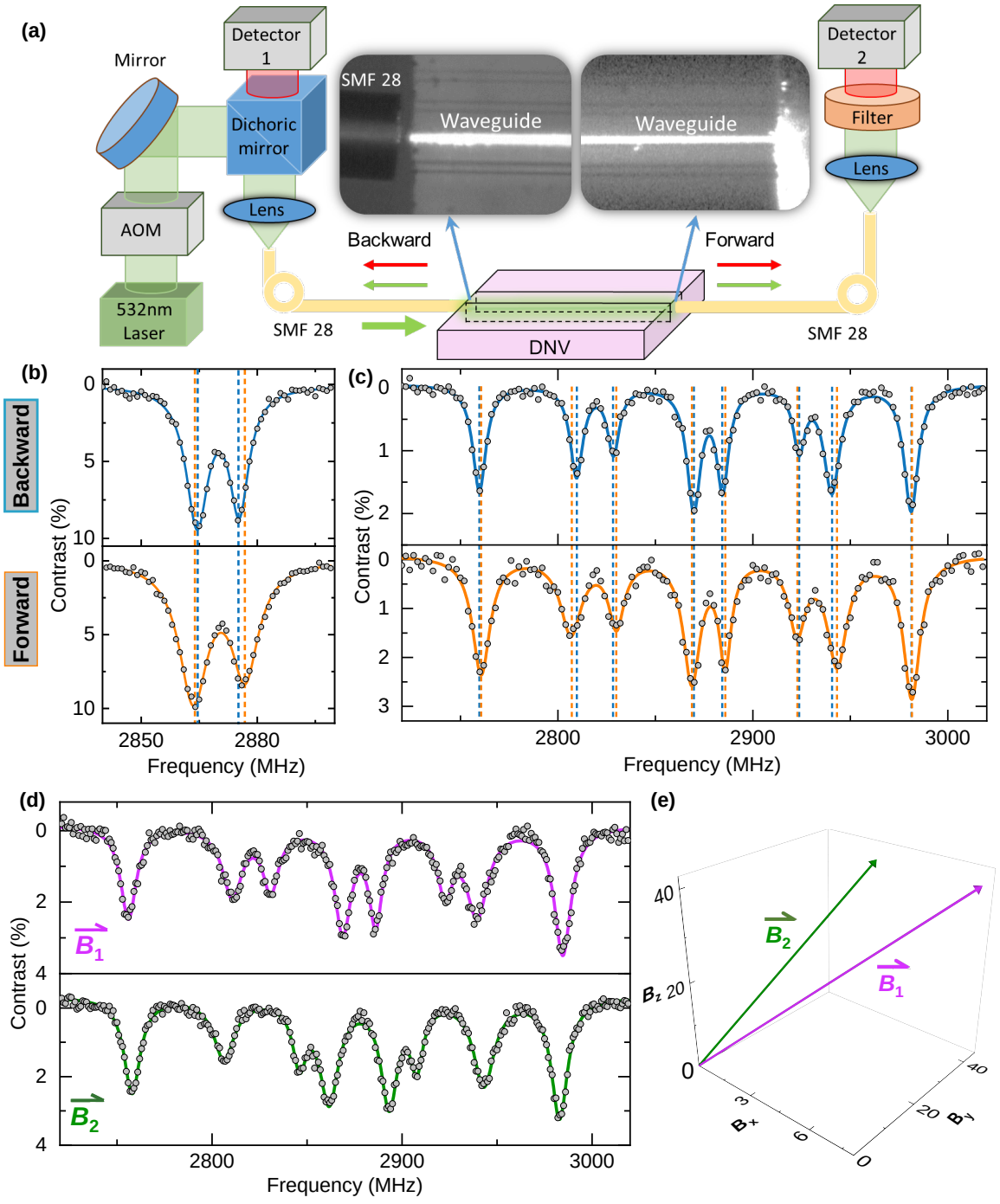

Figure 4.3. Enhanced quantum sensing via fibre-waveguide-fibre configuration. (a) Schematic diagram of fibre-waveguide-fibre configuration where the insert two microscopy images show backward and forward travel light in the waveguide. (b) Zero-field ODMR (c) ODMR spectra with the applied magnetic field are recorded by backward PL (upper plates) and forward PL (lower plates) where the vertical blue and orange dash lines represent the resonance frequency from backward and forward travelling ODMR curve fitting. (d) Magnetic field sensing via the forward travelling waveguide ODMR. (e) Magnetic field vector inferred from (d).

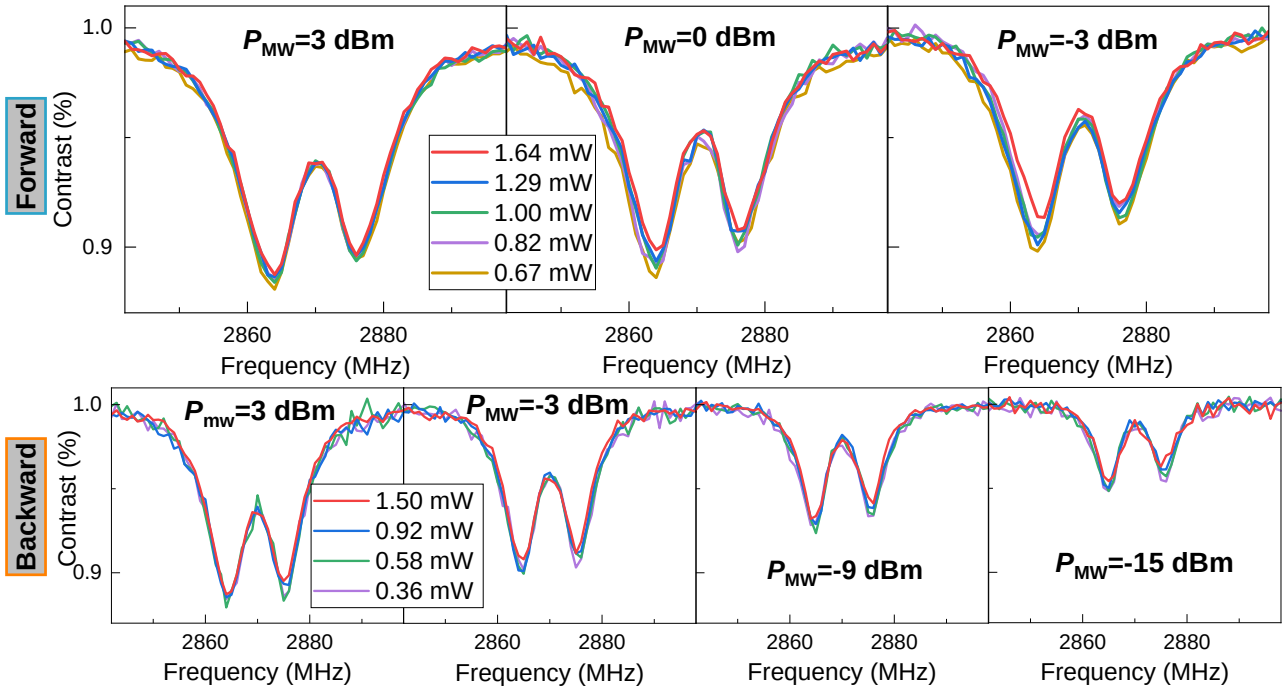

Figure 4.4. Laser power and MW power effects on zero-field CW-ODMR via collecting forward (upper plates) and backward (lower plates) PL emission.

that of native NVs in pristine regions. $\Lambda \sim 3\%$ is ODMR contrast. t_L $\sim$0.5 µs is the readout duration time. The detected PL rate is the total detected PL rate relying on the excitation power and experiment configuration. For a confocal configuration with NA=0.95 objective, the saturation PL rate of $362.4\,\mathrm{GHz}$ and saturation power of 11.7 mW is achieved in Fig. 4.5. The confocal laser spot could be taken as a ellipsoid with the radius of $0.5\,\mu\mathrm{m}$ and heigh of $2.2\,\mu\mathrm{m}$ to estimate its volume of $2.30\,\mu\mathrm{m}^3$, from Fig. 3.3. In this case, the saturation power of 11.7 mW can be converted to a saturation power density of $5.08\,\mathrm{mW}\cdot\mu\mathrm{m}^{-3}$. Thus η_{dc} and η_{ac} in this confocal configuration are $0.56\,\mathrm{nT}\cdot\mathrm{Hz}^{-1/2}$ and $0.18\,\mathrm{nT}\cdot\mathrm{Hz}^{-1/2}$ by the equation 3.7 and equation 3.8.

One can estimate how this signal may scale in the fibre-waveguide-fibre configuration, even if experimental practicalities prevent us from doing so in this work. A 10-fold larger mode field diameter ($\sim$5 µm from Table 4.1) in the waveguide requires 100 times higher excitation power to reach saturation[94, 111], which at $1.17\,\mathrm{W}$ is outside the range of our experimental apparatus. A laser power of $1.5\,\mathrm{mW}$, much less than saturation power, was used to evaluate the PL emission in fibre-waveguide-fibre configuration. I infer $40\,\mathrm{GHz}$ PL rate in the backward-traveling fluorescence and $4\,\mathrm{GHz}$ PL rate in the forward direction, which is comparable to the PL emission of $42\,\mathrm{GHz}$ in confocal emission. This indicates that 100 times less excitation density in fibre-waveguide-fibre configuration achieves similar PL emission in confocal configuration due to probing a large volume of NVs. Therefore, I can estimate a 100 times PL rate enhancement under 100 times higher excitation

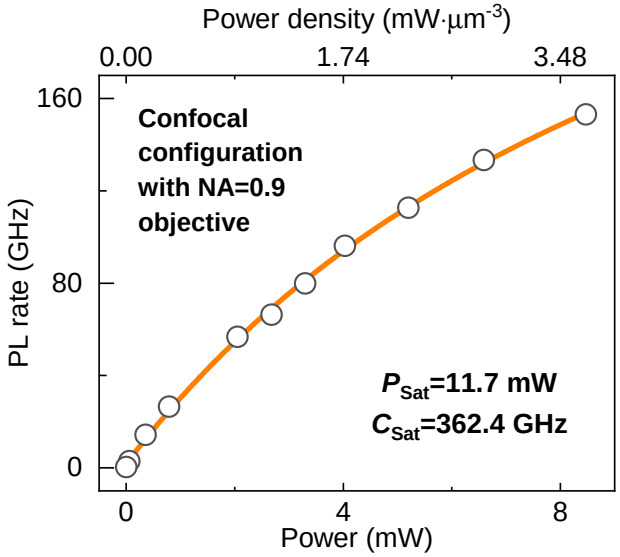

Figure 4.5. Laser power-dependent PL emission under confocal configuration, where the experiment raw data (white points) is fitted by an orange saturation curve from the equation 3.2. I state that the laser power density is obtained by laser power divided by the confocal laser spot volume, which is described in the section4.7

power, offering a 10-fold improvement of sensitivity of η_{dc}=56 pT · $\mathrm{Hz}^{-1/2}$ and η_{ac}=18 pT · $\mathrm{Hz}^{-1/2}$.

4.8 Conclusion

I introduced an approach for waveguide-enhanced quantum sensing using a high-quality buried waveguide in diamond chip with 4.5 ppm NV density. I observed that femtosecond laser fabrication does not change the density, spectra, and spin coherence properties of the NVs, leading to a high sensitivity and increased optical depth with ten micrometres of resolution. In a fibre-waveguide-fibre setup, I obtained robust ODMR response from which we inferred the magnetic field magnitude and direction. Compared to conventional confocal setup, I estimate 100 times higher PL emission and 10 times improvement of sensitivity of η_{dc}=56 pT · $\mathrm{Hz}^{-1/2}$ and η_{ac}=18 pT · $\mathrm{Hz}^{-1/2}$ in fibre-waveguide-fibre configuration. Other than the improved sensitivity, WGINVs in DNV-B14 are significantly more reproducible compared to the WGINVs in HPHT diamond in my previous report[94], thanks to a more uniform NV in the CVD sample and the lack of a post-thermal annealing step. Future work will focus on electric field sensing, bio-sensing, and liquid sensing based on this laser-written integrated photonic diamond chip, potentially integrating with microfluidics.

Chapter 5

Photo-dynamics of quantum emitters in aluminium nitride

5.1 Statement of authorship of paper included in Chapter 5

Chapter 5 of the thesis is based on the following published paper: Yanzhao Guo, John P. Hadden, Rachel N. Clark, Samuel G. Bishop and Anthony J. Bennett, "Emission dynamics of optically driven aluminum nitride quantum emitters," Physical Review B 110, 014109 (2024)[143].

The corresponding author identified the following author contributions, using the CRediT Contributor Roles Taxonomy standard:

Yanzhao Guo.: Conceptualization, Methodology, Software, Investigation, Data-curation, Writing-original draft, Writing- review and editing. John P. Hadden: Software, Methodology, Writing-review and editing, Supervision, Funding acquisition. Rachel N. Clark: Software, Methodology, Writing- review and editing. Samuel G. Bishop: Software, Methodology, Writing- review and editing. Anthony J. Bennett: Conceptualization, Methodology, Writing- review and editing, Supervision, Project administration, Funding acquisition.

5.1.1 Highlight

AlN is a technologically important wide bandgap semiconductor which has been shown to host bright QEs. In this chapter, I use PECS, TRPL and state-population dynamic simulations to probe the dynamics of emission under CW and pulsed optical excitation. I infer that there are at least

four dark shelving states, which govern the TRPL, bunching and saturation of the optical transition. I study in detail the emission dynamics of two QEs with differing power-dependent shelving processes, hypothesised to result from charge ionization and recombination. These results demonstrate that photon bunching caused by shelving the system in a dark state inherently limits the saturation rate of the photon source. In QEs where increasing optical power de-shelves the dark states, I observe an increased photon emission intensity.

5.2 Introduction

Single QEs in wide bandgap semiconductors are promising single-photon sources which can operate up to room temperature[144, 56, 145]. In addition to the numerous luminescent defects in diamond[146], there are more recent reports of quantum light emission in SiC[147], silicon nitride (SiN)[148] and the group III-nitrides. Many of the QEs reported in the latter category display favourable optical properties including a high DW factor (>0.5) in GaN [149, 78], a high CW photon detection rate of 3.7 MHz from a single emitter in hBN [150] and availability of low-cost epitaxial wafers of AlGaN [151]: therefore each potentially offers advantages for scalable quantum nanophotonics [152]. Moreover, some QEs in hBN and GaN have been reported with ODMR response[60, 153, 78], which makes them attractive for quantum sensing.

Another member of the III-nitride semiconductor family, AlN is a commercially important semiconductor for high-power and optoelectronic devices. The discovery of QEs hosted in a material with advanced crystal growth technology and established industrial fabrication processes paves the way to wafer-scale device manufacture at a low marginal cost. Various QEs have been reported within its ultra-wide $\sim$ 6.015 eV bandgap. For example, Lu et al. found QEs with 580-650 nm emission and low multi-photon emission probability ($g^{(2)}(0)$<0.1) by He implantation into a commercial AlN film on a sapphire substrate[74]. Samuel G. Bishop et al. also reported similar emitters in an as-grown AlN film[73], and recently enhanced their PL saturation rate to almost 1 MHz using an index-matched solid immersion lens [149]. Wang et al fabricated emitters with near 0.65 Debye-Waller factor emitting near 600 nm in free-standing AlN by laser writing [75].

Despite this interest in AlN's QEs, their physical origin and electronic structure remain uncertain. Theoretical calculations have shown that AlN QEs may host solid-state qubits with long qubit-state lifetime due to their small spin-orbit splitting [154] but it is not certain that the observed QEs are the same as those simulated. Previous studies on QEs in AlN have reported photon bunching associated with transition to one longer-lived metastable dark "shelving state" [149, 155, 74, 75]. This shelving process occurs when the population of the excited state relaxes to a metastable state without a photon being detected, either through a non-radiative process or photon emission at a

wavelength outside the detection range. However, a single shelving state is insufficient to explain their full PL behaviour. A better understanding of their radiative and non-radiative transitions may allow optimization of quantum emission, for example through state preparation, or by identifying features that allow pre-selection of QEs with a certain performance. The existence of a dark shelving state is a pre-requisite for the fluorescence depletion mechanism which can be used for stimulated depletion spectroscopy [156, 157], and super-resolution microscopy applications[156, 158]. More fundamentally, determining the electronic structure of these QEs is also an important step in the effort to determine their physical origin.

In this chapter, I use optical excitation to probe the emission dynamics in two QEs with differing power-dependent behaviours. PECS and TRPL are compared to simulations showing that there are at least six internal energy levels in each emitter (one ground state, one radiative excited state and four shelving states). The two QEs have different laser power-dependent shelving and de-shelving processes. These results demonstrate that photon bunching caused by shelving the system in dark states inherently limits the saturation rate of the photon source. However, in the QEs I identify that can be optically driven out of the dark state, bunching is suppressed at high power, and I observe an increased photon emission intensity.

5.3 Experiment approach

I use a home-built confocal microscope to study isolated single QEs in a commercial single-crystal c-plane $1\,\mu\mathrm{m}$ AlN film on a sapphire template at ambient conditions [73] with an emitter density of $0.09\pm0.02\,\mu\mathrm{m}^{-2}$. The emitter density is calculated by counting the number of QEs from several randomly selected areas. By investigating ten QEs in this AlN film I identify QEs in which shelving processes are found to increase or decrease with laser power, exemplified by emitters QE A and QE B, respectively which are studied in detail. All the measurements are made with the laser polarisation aligned to the QE's preferred absorption polarisation angle [73] with no polariser in the collection path. The collection optical filter window is between 532-650 nm covering their dominant spectral emission range. Further details on the confocal system are in 2.2.1 in the Chapter 2. These QEs often show spectral and intensity fluctuations on the milliseconds to seconds timescale at room temperature [73], but display consistent spectral and photodynamic properties after months of measurements in ambient conditions.

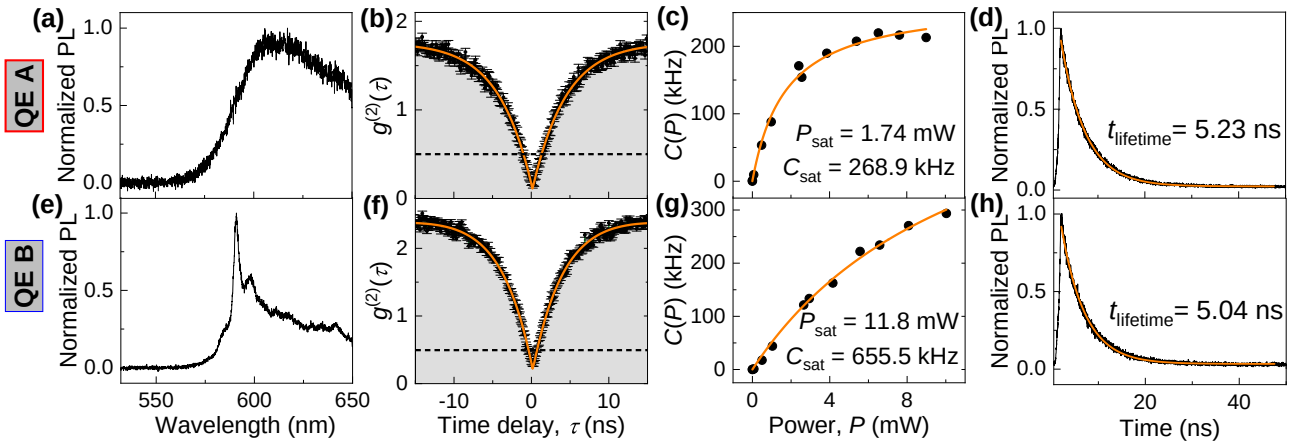

Figure 5.1. Characterization of two QEs in AlN at room temperature: QE A (first row) and QE B (second row). (a) and (e) show the spectra between 532 and 650 nm. (b) and (f) are the photon emission correlation histograms, normalised, without background correction (black points) and fit using an empirical model discussed in the text (red line). Error bars represent Poissonian uncertainties based on the photon counts in each bin. (c) and (g) are the CW-PL saturation behaviours (black points) as a function of laser power, fit using equation (3.2). (d) and (h) show the excited state lifetime measurement, fit with a single exponential (red line).

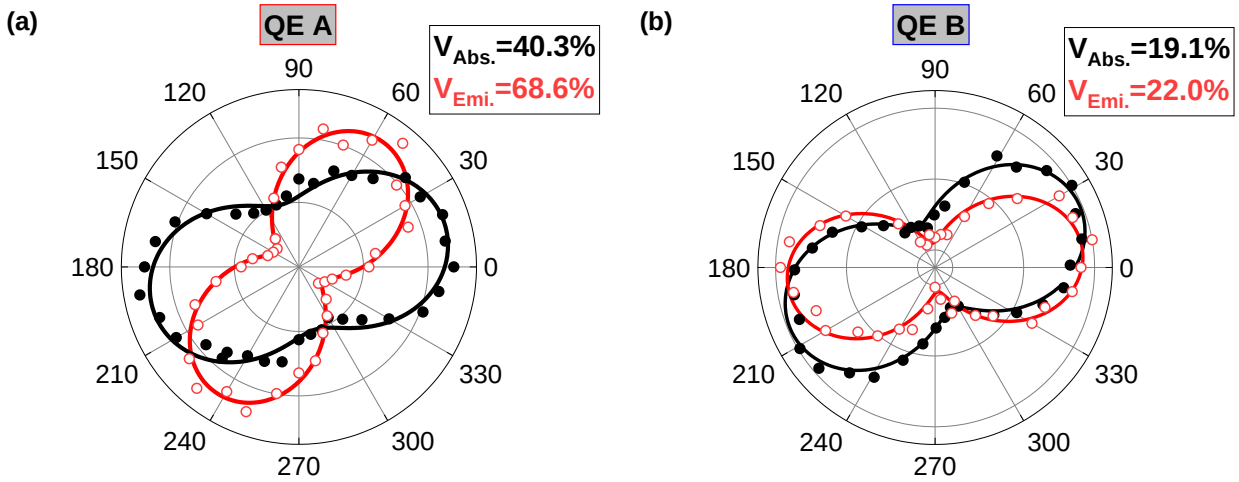

Figure 5.2. Absorption and emission polarisation plot of QE A (a) and QE B (b). The black-filled circles and red open circles represent the experiment data for absorption and emission polarisation. The black and red solid lines are the least squares fitting curve (from equation 5.1) for absorption and emission polarisation where their visibilities are given by equation 5.2

5.4 PL study

In Fig. 5.1(a), the spectrum of QE A consists of a single broad feature I attribute to the PSB extending from 600 nm to beyond the optical filtering cut-off at 650 nm. The absence of a resolvable ZPL suggests a low DW factor, consistent with some previous reports [73, 149]. In contrast, in Fig. 5.1(e), QE B displays a strong ZPL at 590 nm with a PSB more comparable to the $N_{Al}O_N$ type defect proposed in a recent study [75]. The correlation histograms of both QEs display substantial bunching over hundreds of nanoseconds, nevertheless, the values of $g^{(2)}(0)$ for QE A and QE B are 0.16±0.042 and 0.29±0.034, respectively, in Figs. 5.1(b) and (f). Such low $g^{(2)}(0)$ suggests a single transition is involved in photon emission across this spectral feature. Another signature of a quantized emitter is its PL intensity saturation with CW excitation. Figs. 5.1(c) and (g) show this data fitted by the equation 3.2. QE B requires 6.8 times higher P_{sat} and has 2.4 times higher C_{sat}. The PSB is truncated via a 650 nm short pass filter which suppresses the emission from the sapphire substrate. Thus, was I able to detect the full spectrum the saturated intensities would be higher. Despite the difference in saturation behaviour, the two QEs both have a ∼5 ns radiative lifetime obtained by fitting a single exponential decay function to the TRPL data in Figs. 5.1(d) and (h), suggesting the difference in saturation intensity is a result of differing non-radiative pathways [158, 157]. I state $g^{(2)}(\tau)$ and lifetime measurements are implemented with an optical window $532\text{-}650\,\mathrm{nm}$ without extra spectrally filtered. Their absorption and emission polarization behaviours are shown in Fig. 5.2, indicating similar optical dipole properties from previous studies[73]. The polarisation plots are fitted by

$$C(\theta) = A\cos^2(\theta - \theta_0) + B \tag{5.1}$$

where *A* is the amplitude, θ_0 is the polarisation angle of the maximum PL rate, and *B* is the offset[80]. Their visibilities V are calculated by equation[80],

$$V = \frac{C_{\mathrm{Max}} - C_{\mathrm{Min}}}{C_{\mathrm{Max}} + C_{\mathrm{Min}}} = \frac{A}{A + 2B} \tag{5.2}$$

where C_{Max} and C_{Min} are the maximum and minimum intensities, respectively.

5.5 PECS study

To further explore the dynamics of photon emission in these QEs, PECS was recorded for QE A and QE B (Figs. 5.3(a) and (b)) over $100\,\mu\mathrm{s}$ time scale. The minimum time bin in the PECS is $100\,\mathrm{ps}$. Empirical equation 3.1 is used to fit the PECS. The number of resolvable timescales,

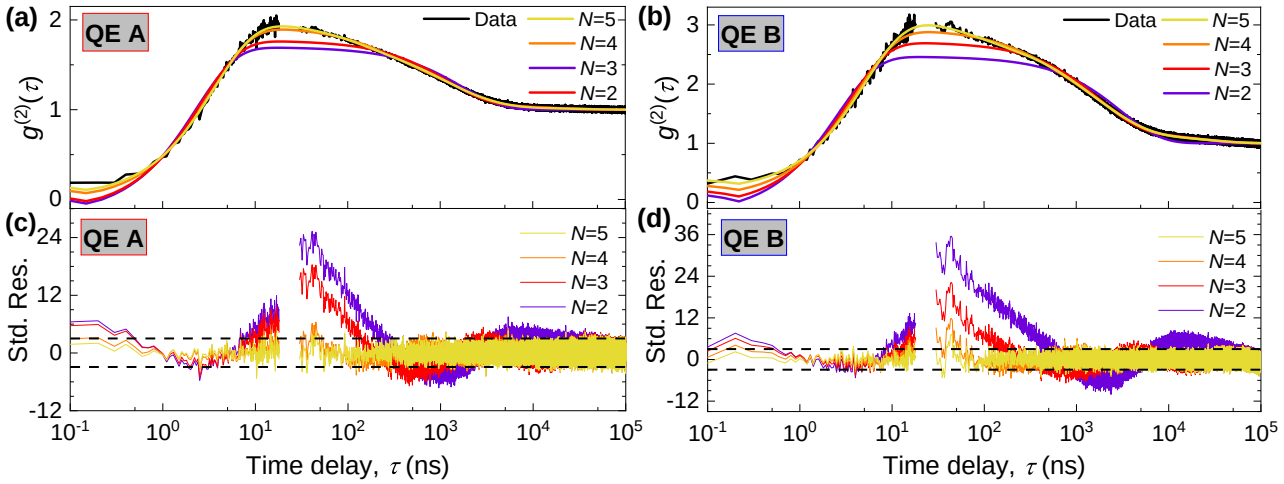

Figure 5.3. Photon emission correlation spectroscopy (PECS). Black lines in (a) and (b) are the PECS of QE A and QE B, fit using empirical equation (3.1) for $N = 2$, 3, 4 and 5. (c) and (d) are the corresponding residuals from the fits to QE A and QE B, respectively. The raw data between 22-35 ns is masked to hide reflections from the APDs' backflash.

N, include radiation transitions and several shelving transitions, which have been determined by calculating and comparing the reduced chi-squared statistic, r-square for each best-fit model. As I shall show later in power-dependent PECS measurement, single radiation transition is predefined for these QEs, which leads to single ground state and excited state. Thus, the total number of energy levels is the number of transitions plus the ground state (*N*+1). The total number of shelving states is the number of transitions minus the excited state (*N*-1). Figs. 5.3(c) and (d) show standardized residuals for each QE for the best-fit empirical model at different *N*. Interestingly, for both QEs an adequate fit (within the noise level of the data) is provided by the *N*=5 model, suggesting at least four shelving levels, plus the radiative state, are present. And their timescales range from ns to tens of µs which are much more complex than simple one shelving process with sub µs timescale in the previous reports in AlN [73]. However, this behaviour is comparable to some optically addressable QEs in hBN[153, 159], where the tunable shelving process might predict the spin-selective transition. These shelving states could arise from different spin manifolds or charge states internal to the QE or fluorescence intermittency caused by charging of nearby trap sites [117, 160, 161].

To investigate the power-dependence of shelving, the power-dependent $g^{(2)}(\tau)$ under CW excitation has been fitted with equation (3.1) for $N = 5$. In Figs. 5.4(a) and (b), QE A and QE B show nearly opposite power-dependent bunching mechanisms, indicating the different power-dependent shelving dynamics. Figs. 5.4(c) and (d) summarize the fitting results of the antibunching and bunching rates and amplitudes for QE A and QE B, respectively. First of all, there are two obvious different trends for the antibunching amplitude C_1 which shows power increase bunching behaviour for QE A and power decrease bunching behaviour for QE B. It straightforwardly

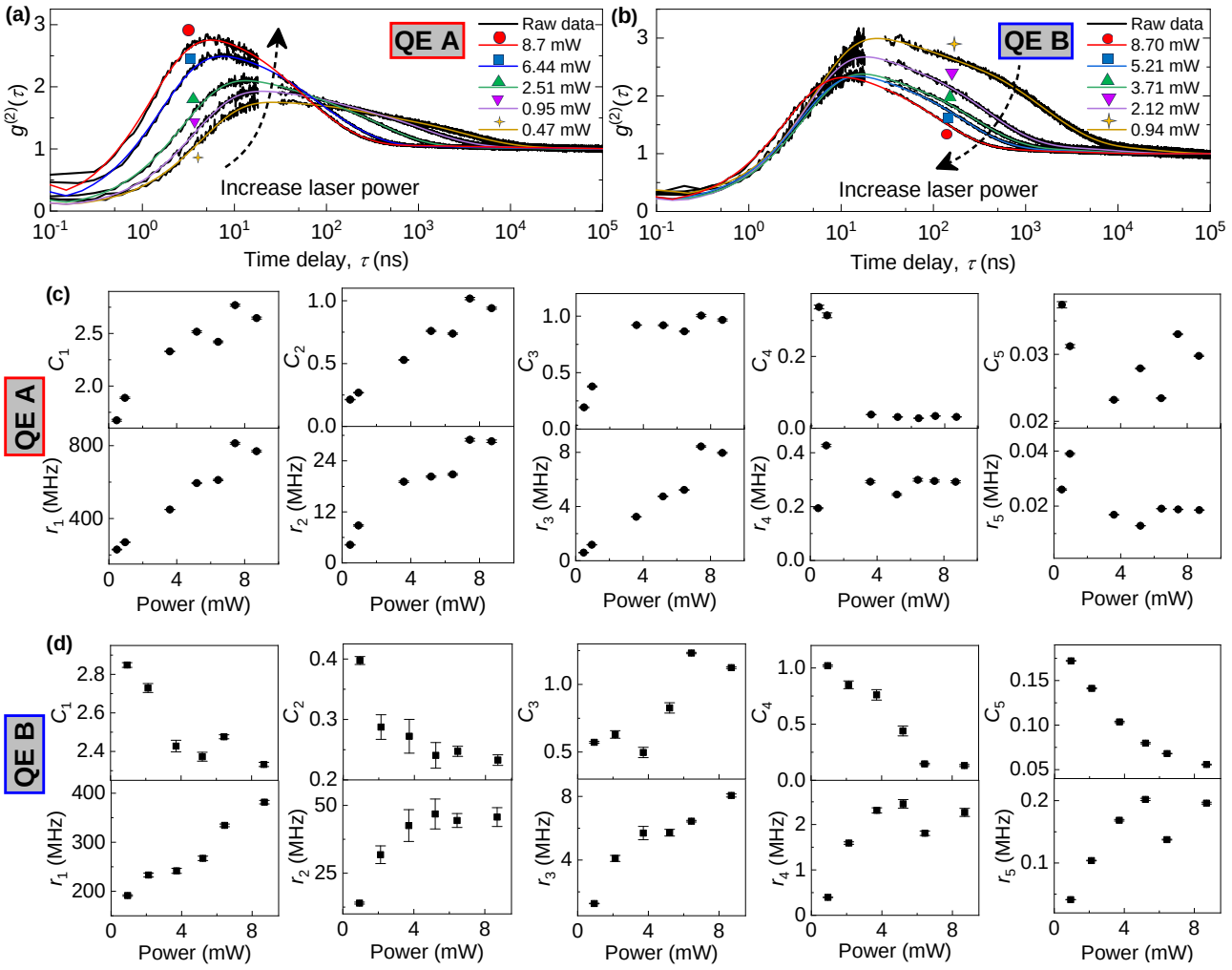

Figure 5.4. Power-dependent PECS from (a) QE A and (b) QE B. Each autocorrelation is fitted with equation (3.1) and $N = 5$. (c) and (d) are amplitudes C_i and rates r_i arising from fitting the equation (3.1) for QE A and QE B, respectively.

indicates the opposite laser power-dependent non-radiation shelving in QE A and QE B. However, due to as many as 4 shelving states, the bunching behaviour associated with these four shelving states would be much more complicated. For QE A, the dominant $C_{2,3}$ bunching amplitudes rise with laser power, thus the bunching increases in Fig. 5.4(a). This trend reveals that the increasing laser power transfers the population from the excited state to these shelving states, reducing the PL intensity [157]. This power-enhanced bunching behaviour is consistent with previous reports on these same samples [73, 149]. Moreover, these are decay trends with weak amplitude as laser power in $C_{4,5}$, which could be explained by some weak deshelving process. In contrast, for QE B, the bunching amplitudes $C_{2,4,5}$ fall with power, resulting in a net reduction in bunching with increasing laser intensity. In other words, increasing laser power transfers the population out of the shelving states. This enables QE B to be an efficient radiative emitter at high laser power [158, 162, 157]. There is also a non-monotonic trend in C_3, which may be from the random charge fluctuation between radiation and non-radiation decay[163].

Furthermore, the antibunching rates for QE A and QE B scale linearly with power, indicating a single radiative state[80, 155]. For QE A, bunching rate r_3 shows linear scaling and zero offset with laser power, which suggests the transition between the radiative state and the shelving states is laser-driven. Moreover, r_2 and r_4 for QE A have a non-zero value at low power due to spontaneous emission and yet linearly increase with power, suggesting both optical pumping and spontaneous decay exist[80]. Regarding QE B, the bunching rates are more complicated which are zero at low power (no decay by spontaneous emission from excitation state) but saturate at high power, suggesting the transitions can be optically driven between shelving states[80, 157, 164].

5.6 TRPL study

It is possible to directly probe differences in the shelving dynamics under optical driving, and when the QEs are not illuminated, using time gating. Then recording the PL emission with TRPL would help probe the photodynamics between the internal energy levels of QEs. In Figs. 5.5(a) and (b), I excited QE A and QE B with pairs of square $2\,\mu s$ laser pulses with variable spacing, τ_{double}. The first pulse pumps the population into the shelving states, resulting in an exponentially decreasing intensity until a steady state is reached. Dependent on the delay between the two pulses τ_{double} I observe a revival of the PL emission intensity at the start of the second pulse, as the population decays back to the ground state in Figs. 5.5(a) and (b) [83]. Integrating the first 120 ns PL at the start of the second pulse, I plot the PL revival curve in Figs. 5.5(c) and (d). The double exponential gives an adequate fit, indicating more than one decay rate associated with the shelving states absent of excited laser. This result further supports the inference from Fig. 5.3 that multiple shelving states exist. The fact Figs. 5.5(c) and (d) can be modelled with two shelving states when there is no

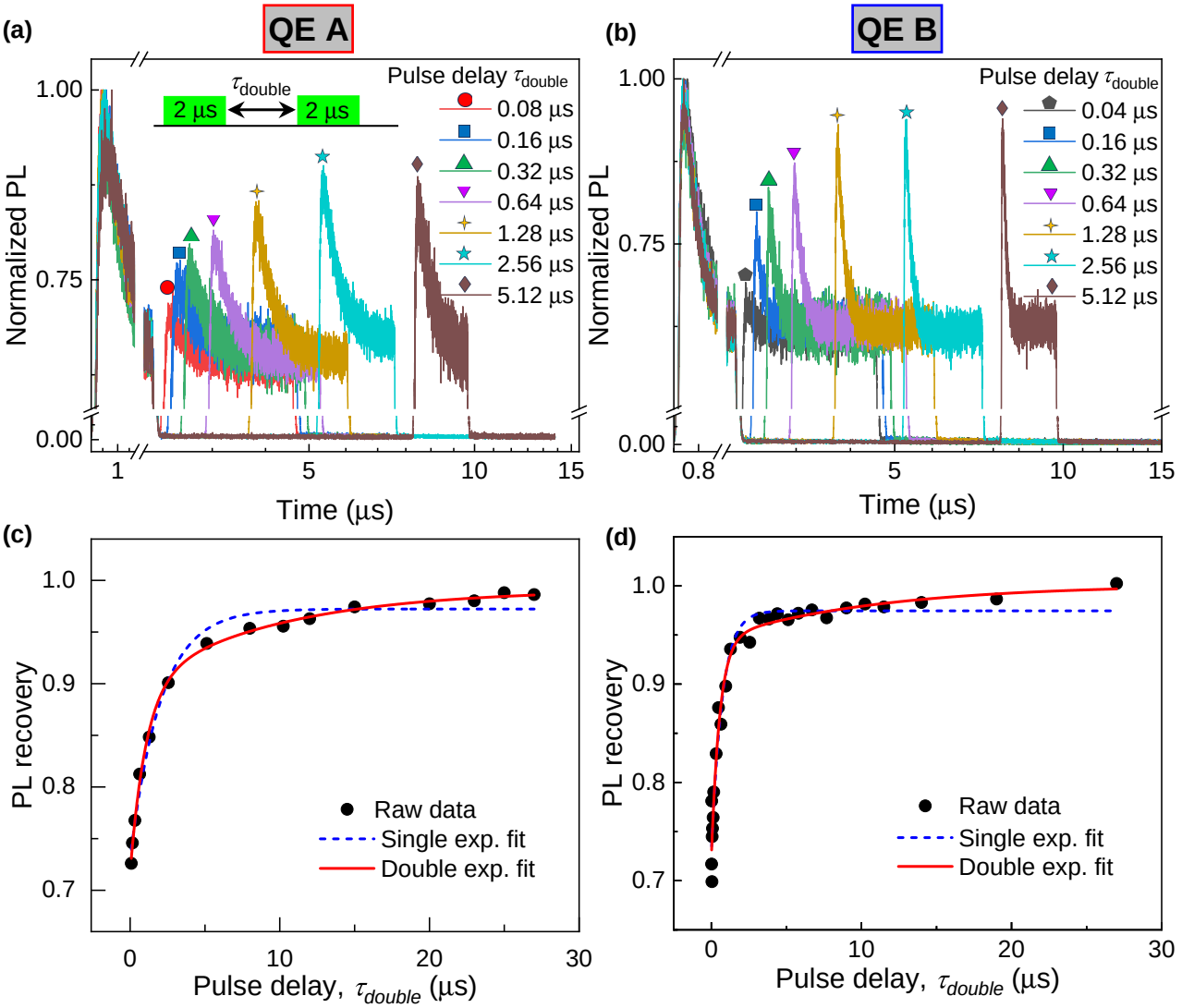

Figure 5.5. Double pulse laser excitation. (a) and (b) are the TRPL of QE A and QE B under double pulse laser excitation. The inset in (a) is the train of the laser pulses. (c) and (d) represent the PL revival behaviour under the second pulse excitation in (a) and (b) fitted by single exponential and double exponential equations.

optical power during τ_{double}, rather than the 4 shelving states required for $g^{(2)}(\tau)$, maybe a result of some laser-driven de-shelving mechanism in QE A and QE B.

The power-dependent optical dynamics can also be probed with TRPL under $2\,\mu\mathrm{s}$ square-pulsed excitation in Figs. 5.6(a) and (b). These saturation behaviours also reveal that the population of the excited state in QE A is rapidly shelved at high power, leading to reduced steady-state radiative emission. QE B requires an 18.2 times higher laser power to saturate than QE A. In contrast, QE B remains an effective emitter at high power. The discrepancy between this value and the ratio obtained from CW saturation (Figs. 5.1(c) and (g)) may be a result of using short $2\,\mu\mathrm{s}$ pulses, which does not allow enough time for the longer time-scale decay processes to reach equilibrium. I fit the TRPL with a single exponential decay function to extract a decay rate and normalized steady-state PL rate in Figs. 5.6(c)-(f). The shelving rate of QE A is super-linear and that of QE B is sub-linear. Referring to the example of the NVs in diamond and QEs in hBN, these saturation behaviours may stem from optically pumped shelving (e.g. charge ionization and conversion)[157, 164, 80].

5.7 Photo-dynamics simulation

To qualitatively understand these power-dependent behaviours, I use a state population dynamics simulation[82] in Fig 5.7 with four different shelving models. For simplicity, I perform this simulation with only three energy levels and vary only the power dependence of the transitions. This approach enables me to understand the trends in the power dependence of PECS and TRPL without the complexity of solving for all N=5 energy levels. Information regarding these simulations is given in Chapter 2. Each model consists of a ground state (GS) 1, an excited state (ES) 2, and a shelving state (SS) 3, where transitions between the states are labelled k_{ij}, where i and j are the initial and final state numbers in insert of Fig. 5.7 (a). The transition rates of the four models are shown in Table 5.1, but briefly, in model I, I assume both shelving and de-shelving transitions are driven by the laser, whereas in model II there is a fixed fast shelving rate and optically pumped de-shelving rate. Moreover, model III is the easiest case with the fixed spontaneous shelving and de-shelving rate. Compared to model III, the last model IV contains an optical repump from the shelving state to the excitation state. From Figs. 5.7 (a) and (b), I observed that model I and model III show the power-increasing shelving behaviour as QE A, while model II and model IV display power-increasing de-shelving behaviour as QE B.

To further demonstrate these models' photo-dynamics, in Figs. 5.7(c), (d), and (e), the PECS and TRPL of these models have been fitted by Eq. 3.1 for $N = 2$ and single exponential decay, respectively. Their steady-state PL saturation is also simulated in Fig. 5.7(f). In Fig. 5.7(c) the antibunching rates (r_1) of these four models are linearly rising with pump power, offset by

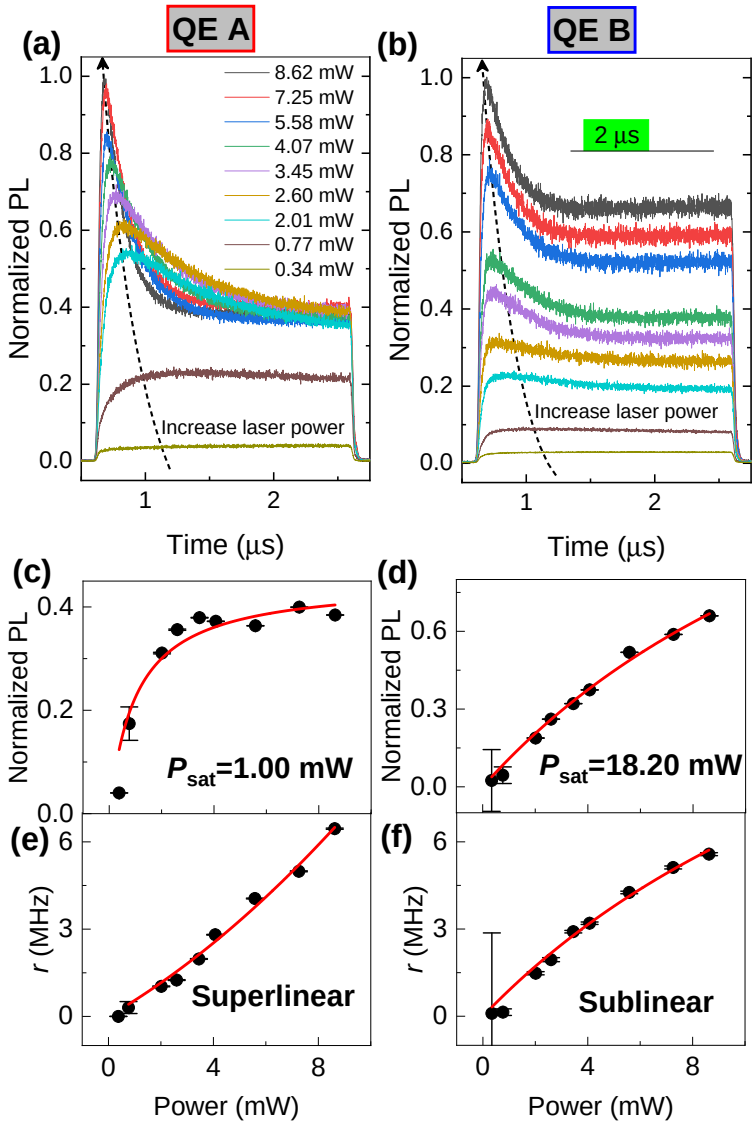

Figure 5.6. Power-dependent TRPL with square excitation pulses. (a) QE A, (b) QE B, with insert showing the pulse sequence. (c) and (d) are the normalized PL saturation behaviours of the steady states. (e) and (f) are the TRPL decay rates observed in (a) and (b).

Table 5.1. Simulation rate table

Model	Shelving rate	De-shelving	Emission transition rate
I	k_{23}= 0.05*k_{12}[a]	k_{31}= 0.03*k_{12}[a]	k_{21}= 200 MHz
II	k_{23}= 10 MHz	k_{31}= 0.03*k_{12}[a]	k_{21}= 200 MHz
III	k_{23}= 10 MHz	k_{31}= 4 MHz	k_{21}= 200 MHz
IV	k_{23}= 10 MHz	k_{31}= 4 MHz, k_{32}=0.005*k_{12}[a]	k_{21}= 200 MHz

[a] Optically excited rate k_{12} = α_{12}*k_{21}, α_{12}=0.01, 0.05, 0.1, 0.2, 0.5, 1, 2, 5, 10.

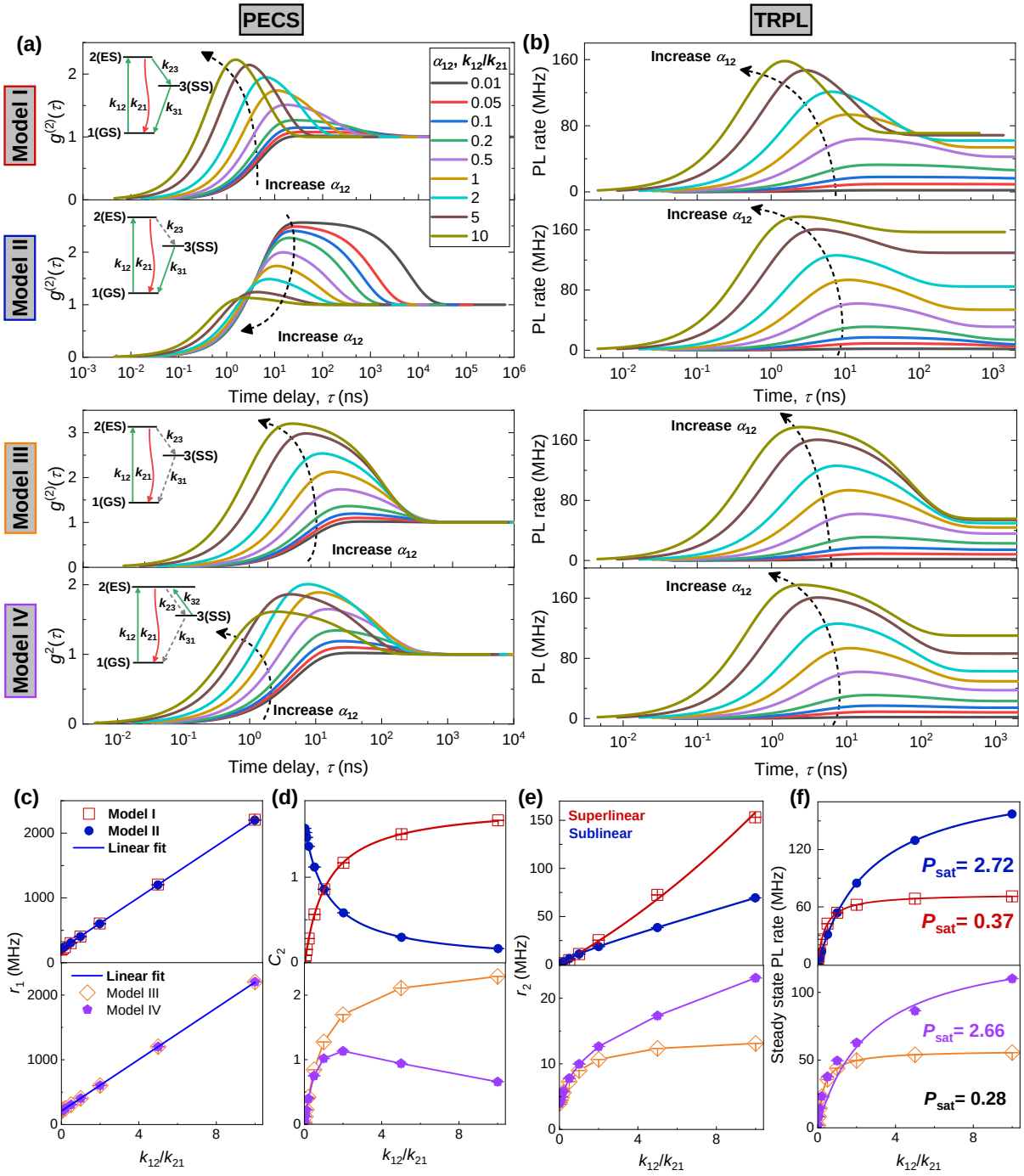

Figure 5.7. State population dynamics simulation. (a) PECS and (b) TRPL simulation results for shelving Model I and Model II with transition rates from Table 5.1. The inset in (a) is the proposed three-energy level shelving Model I, II, III and IV which include radiative emission (red arrow), optically pumped transitions (green arrows), and non-radiative transitions with a fixed spontaneous decay rate (dotted grey arrows). (c), (d) and (e) are the best-fit parameters r_1, C_2, and r_2 determined by fitting simulated $g^{(2)}(\tau)$ data using equation (3.1) with $N = 2$. (f) is the steady state PL saturation behaviour fitted by equation (3.2). The results are plotted as a function of k_{12}/k_{21}, where k_{21}= 200 MHz is a fixed parameter as the spontaneous emission decay rate.

the spontaneous emission rate, which is consistent with the results of QE A and QE B. Moreover, models I and III display opposite power-dependent bunching dynamics compared to modes I and IV. Specifically, model I and model III show an increasing bunching amplitude comparable to what is observed in QE A. On the other hand, model II and model IV show a reduced bunching amplitude comparable to what is seen in QE B.

Interestingly, the TRPL shelving rates of model I and model II in Fig. 5.7(e) can be fitted by superlinear and sublinear functions with zero offsets, which is perfectly consistent with the TRPL results of QE A and QE B in Figs. 5.6(e) and (f). However, the shelving rates of model III and model IV could get saturated. Additionally, model II and model IV show several times higher saturation power and saturation intensity than model I and model III in Fig. 5.7(f), which is comparable to the results of QE A and QE B in Figs. 5.1(c) and (g). Overall, comparing my simulation and experimental results, I conclude that QE A displays model I shelving and QE B displays model II behaviour.

As the physical structure of the studied emitters is unknown, it is difficult to unambiguously determine the physical origin of the shelving and de-shelving behaviours I have observed. However, it is instructive to compare their behaviour to other well-studied emitters in other materials. I note that the behaviour of QE A with shelving Model I is comparable to the NV in diamond which displays laser-induced shelving and de-shelving to the NV^0 at high excitation power, as well as spontaneous shelving and de-shelving to the NV singlet states[157, 165]. In contrast, at low power, QE B is fast-decaying to the shelving state resulting in a strong bunching in the PECS, while at higher laser excitation this bunching is suppressed, allowing higher emission rates by laser-induced de-shelving. This is not common for single QEs under monochromatic laser excitation but is observed in multiple laser excitation of QEs in hBN as well as the NVs[158, 156, 162, 157]. One laser is selected to efficiently pump the ground state, while another laser re-pumps the population out of the shelving state, allowing recovery of the emission[158, 156, 162]

Based on the discussions above, a key factor for the achievable saturation PL rate of QEs is the shelving dynamics at high power. The ideal QE should have reduced shelving at high power, as observed in QE B. A second colour laser could be used to efficiently repump the population from the shelving state back to the bright transition. In the best case, the non-radiative transition could be completely neglected, leading to an emitter with an intensity determined only by the spontaneous decay rate. For example, QE A would become $\sim$2.5 times brighter at saturation, giving $>$ 0.67 MHz PL rate, and QE B would become 1.5 times brighter leading to $\sim$ 1.0 MHz PL rate.

5.8 Conclusion and future work

5.8.1 Conclusion

In conclusion, AlN QEs display complex optical dynamics which indicates they have internal electronic level structures with multiple charge or shelving states. I identify two different optical-power-dependent shelving behaviours associated with the charge ionization and recombination processes. I propose models of the dynamic behaviour which complements previous reports and explains the quantitative features of my observations which provide an important experimental reference for future theoretical work. Moreover, this study will be useful in designing a suitable protocol to minimise the time each QE spends in metastable shelving states, resulting in an overall increased intensity.

5.8.2 Future work in photo-dynamics study

The further task for the photo-dynamics study on quantum emitters in AlN should focus on the charge dynamics study. For example, energy-dependent behaviour of the shelving and de-shelving processes using tunable lasers, such as PLE characterization. Moreover, the techniques used in this chapter offer a way to study the internal energy levels in the QEs of other materials, for example, QEs in GaN, hBN, and SiN. Especially, the recent ODRM on quantum emitters in GaN suggests that the ODMR contrast is from the multiple tunable shelving processes[78]. The PECS and TRPL measurements would further disclose the photodynamics behind these optical addressable quantum emitters, which is crucial for designing the quantum control protocol. These photodynamics studies combining their spin properties will benefit theoretical studies on the nature of these QEs.

Chapter 6

Native quantum emitters in free-standing gallium nitride

6.1 Highlight

GaN is the third-biggest commercial semiconductor with extensive electrical and optical applications. In quantum-based applications, GaN hosts a variety of QEs with ZPLs from the visible range to the telecommunication band. However, their origin remains under debate. Moreover, most of these studies are on the thin film GaN with foreign substrates, which leads to a question: are these QEs present in the GaN complex or the defect-rich interface between the GaN and its substrate? In this chapter, I report the native QEs in the free-standing GaN at room temperature. They are tentatively ascribed to Fe-related and Ge-related complex defects modulated by the dislocation density. This study will not only provide useful information about the nature of QEs but also provide a promising way to fabricate them, such as by controlling doping and ion implantation.

6.2 Introduction

As the pioneer of third-generation semiconductors, GaN has excellent electrical and optical properties, such as direct bandgap, high electron mobility, and stable chemical and physical inertness[166]. This contributes to a huge market for opto and microelectronics devices, for example, high-power high-frequency electronic devices[167], light-emitting diode applications[168, 169], and lasers[168]. Such potential interests further stimulate its mature material growth processes, such

as metal-organic chemical vapour deposition[170, 171], allowing for p-type and n-type doping with structures ranging from nanoscale to freestanding bulk material.[172, 56, 173]

Recently, GaN has emerged as a promising host for single-photon QEs with excellent spectral properties[174, 76]. These QEs feature a wide emission range with ZPLs from the visible to telecom regime[56, 76], a high DW factor of >0.5[175, 78], low multi-photon emission probability of ($g^{(2)}$(0)<0.05), high brightness of 1.5 MHz[76], and integration compatibility[176]. These excellent quantum light sources have been integrated within metropolitan quantum key distribution systems[177]. Moreover, QEs could be resonantly excited with nearly Fourier-transform-limited lines of 250 MHz[77], paving the way for coherent control of the emitters' quantum states. More recently, the high-contrast (20%) optically detected magnetic resonance of single QE has been found in Fe-doped GaN film with sapphire substrate at room temperature[78], implying coherent spin in GaN is a potentially low-cost, manufacturable quantum information platform compared to well-known NVs in diamond.

However, previous studies mainly focus on the thin film of GaN hetero-epitaxially grown on various other substrates.[56, 178, 172], and there are few studies on native QEs in free-standing GaN[172], which leads to the question: whether the QEs exclusively originate from the dislocation-rich interface between GaN and its substrate instead a pure GaN complex. Meanwhile, it is also difficult to discuss the origin of QEs in a thin GaN film with the foreign substates[56, 179, 172, 178].

In this chapter, I report native single-photon QEs in free-standing N-type GaN with (0001) C plane at room temperature. By investigating four different doped GaN, the native single-photon QEs are tentatively ascribed to be the Fe-related and Ge-related complex defects. This study directly confirms the existence of native QEs in GaN crystal and their complex defect nature. It provides a strategy to create QEs in GaN via doping and ion implantation which is crucial for the integrated quantum photonics platform.

6.2.1 PL characterization of free-standing GaN before annealing

As illustrated in 2.1.3, the single crystal free-standing nominally undoped, Si-doped, Ge-doped, and Fe-doped N-type GaN samples with (0001) C plane, purchased from MSE Supplies, are investigated by a home-built confocal microscopy (see 2.2.1) before any treatment. A 532 nm laser was used to excite the GaN sample, and its PL emission is filtered by a 532 nm long pass filter only. As shown in Fig. 6.1, the near-surface of the GaN sample is mapped from the z-direction (overhead) by scanning in x-y and x-z planes. To check the QEs in a fair polarisation condition, the x-y planes are mapped with excitation polarisation angles of 120°, 60 °, and 0°.

From the x-y PL maps in Figs. 6.1(a-b), no isolated emitters are found in undoped GaN

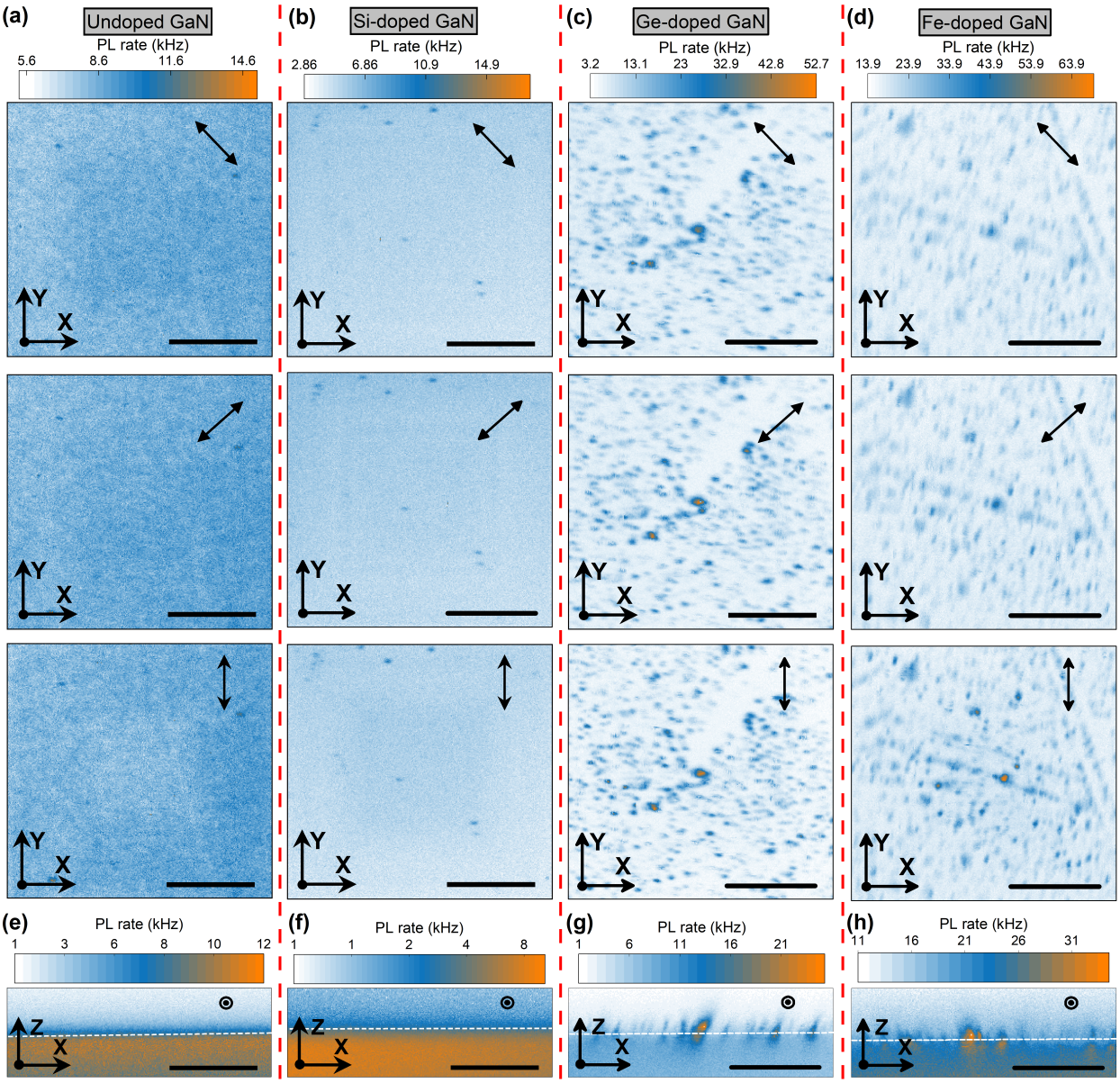

Figure 6.1. Near-surface PL maps for free-standing undoped (a,e), Si-doped (b,f), Ge-doped (c,g), and Fe-doped GaN (d,h) with the same excitation power, where the black bars represent the scale of 10 µm. The three plates in (a-d) are mapped from the z-direction (overhead) by scanning in the x-y plane with excitation polarisation angles of 120°, 60 °, and 0° (as denoted by the black arrow), respectively. (e-h) are the x-z PL maps when the polarisation of the excitation laser is 0°, where the white dashed lines represent the surface of GaN.

which is almost similar to Si-doped GaN except for very few dimmer emitters. In contrast, dense bright emitters are optically resolved in Fe-doped and Ge-doped GaN as shown in Figs. 6.1(c-d). The density difference of emitters among the GaN samples indicates that Ge-doping and Fe-doping during the growth would efficiently produce the isolated emitter. Part of the reason can be attributed to lattice distortion, such as local dislocation or vacancies induced by the mismatch of native and extrinsic atoms[178]. Furthermore, only the low density of dimmer emitters in Si-doped GaN, potentially, explains that Ge and Fe might provide the necessary extrinsic impurities to form the emitters. In this case, these emitters are likely to be Ge-related and Fe-related defects.

Similarly, from these x-z PL maps, no resolvable emitters are present in undoped GaN and Si-doped GaN, resulting in a clear PL intensity boundary between the air and GaN in Figs. 6.1 (e-f). Moreover, numerous bright spots are observed near the surface of the GaN sample, overlaying a uniform PL emission at a deeper depth. This is different from previous studies on QEs in GaN with the foreign substrate where the QEs are found in the deeper depth close to the foreign substrate[178, 56]. The interface between GaN and its foreign substrate[56, 178] contains abundant dislocations such as thread dislocations and point defects [178, 172], which may be defect sources for emitters. However, in the case of free-standing GaN, the surface features more active chemical and physical properties to form emitters due to the unstable chemical termination and physical damage. Thus, the density of dislocations or defects correlates to the optical active emitters which is consistent with the previous study[178, 172].

Overall, I can conclude that the emitters observed in this chapter are likely Ge-related and Fe-related complex defects, including the extrinsic atoms and vacancies such as NVs in diamond, whose density is modulated by the local extended defect density. I note these results are consistent with the previous study[178]. The future photodynamics and theoretical studies of these emitters would be helpful to fully confirm thier origin.

To further understand the uniform PL background emission from the deeper depth of these GaN, I took the spectrum for all GaN samples in the depth of $5\,\mu\mathrm{m}$ with sample excitation laser power in Fig. 6.2. Four strong peaks before 600 nm are observed in all the GaN samples as their typical Raman related peaks[180, 181]. However, a stronger emission with a broad band of 600-800 nm is solely found in the undoped GaN and not in the other three GaN samples. Moreover, two peaks of 850 nm and 950 nm are found in Fe-doping GaN, suggesting some ensemble near-infrared emitters. Due to the limited working range of silicon-based detectors, there is no further PL emission over 1000 nm. I note the Ge-doping GaN displays the lowest background emission from 532 nm to 1000 nm.

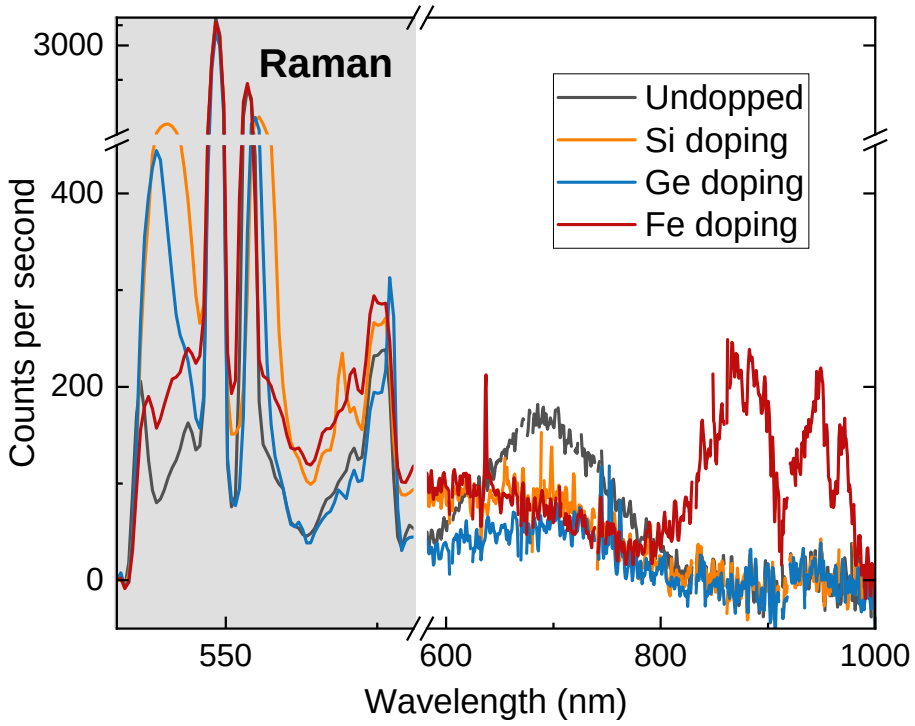

Figure 6.2. Intrinsic background spectra for all four doping GaN samples

6.2.2 Quantum emitters in Ge-doping and Fe-doping GaN

The quantized properties of the emitters in Ge-doped and Fe-doped GaN are investigated in Fig. 6.3. One representative emitter in Ge-doped (QE-Ge) GaN and one representative emitter in Fe-doped (QE-Fe) GaN are systemically studied for their quantized properties. QE-Ge and QE-Fe display similar PL emission spectra with the ZPL around 605 nm in Figs. 6.3(a-b). I state that the difference in the noise ratio of Fig 6.3(a) and (b) is because of the different background noise and collection efficiency during taking spectra. Most of QEs in GaN display ZPL around 590-650 nm. I demonstrated its excitation polarisation behaviour by rotating the half-wave plate, showing optical dipolar properties. In Figs. 6.3(c-d), the excitation polarisation plots are fitted by the equation 5.1. Their visibilities V of 42.7% and 65.3% for QE-Ge and QE-Fe are calculated by the equation 5.2.

The PECS are recorded for the QE-Ge and QE-Fe in Figs. 6.3(e-f), with photon arrival times acquired from two detectors in a Hanbury-Brown and Twiss interferometer. Without any background correction, the values $g^{(2)}(0)$ are 0. 48 and 0.35 for QE-Ge and QE-Fe, respectively.

The background-corrected autocorrelation function is demonstrated by

$$g_*^{(2)}(\tau) = \frac{g^{(2)}(\tau) - (1-\rho^2)}{\rho^2}, \tag{6.1}$$

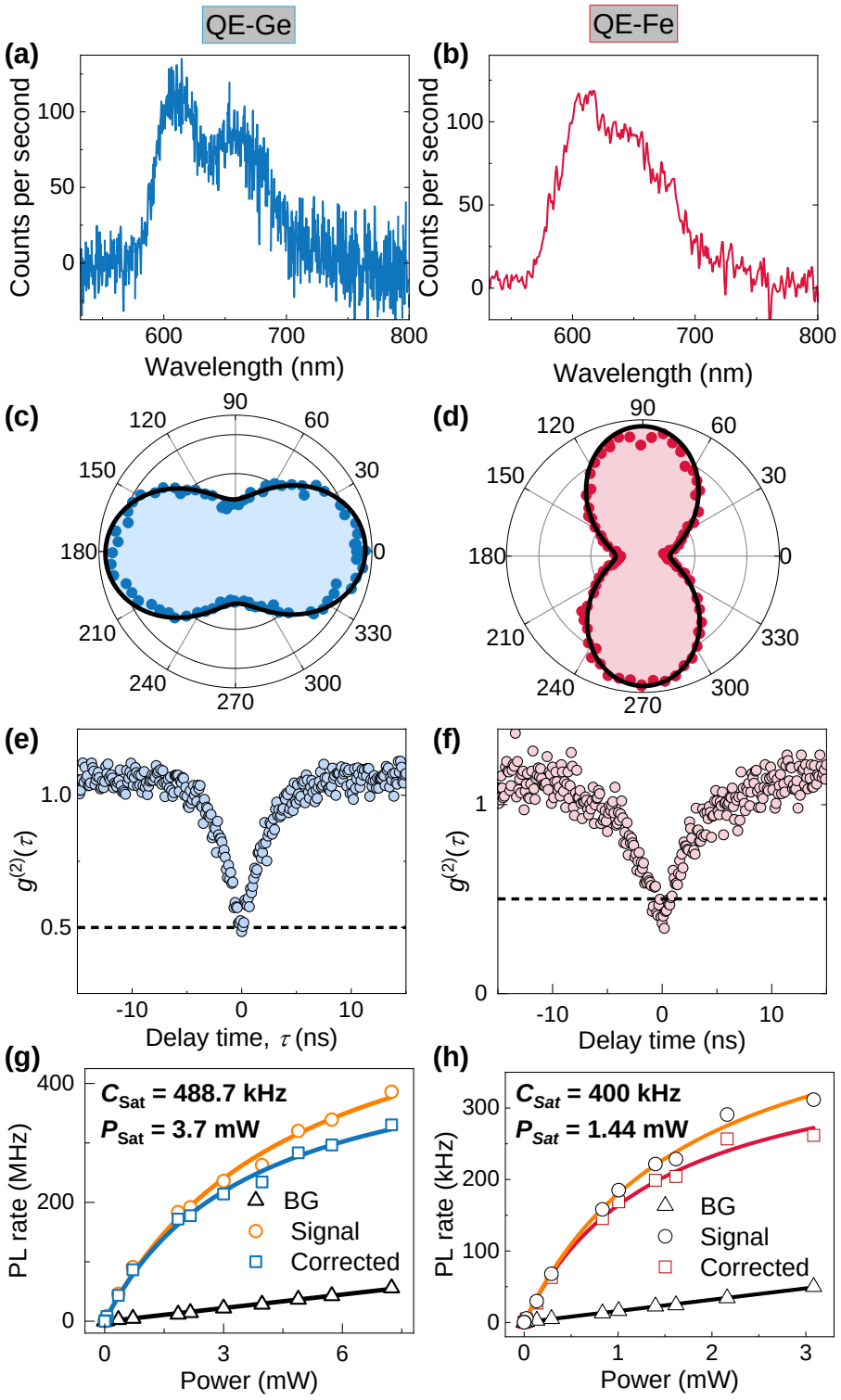

Figure 6.3. PL study of QE in Ge-doping GaN (a,c,e,g) and Fe-doping GaN(b,d,f,h), which includes (a-b) PL spectrum, (c-d) absorption polarisation polt, (e-f) PECS, (g-h) power-dependent PL saturation behaviour.

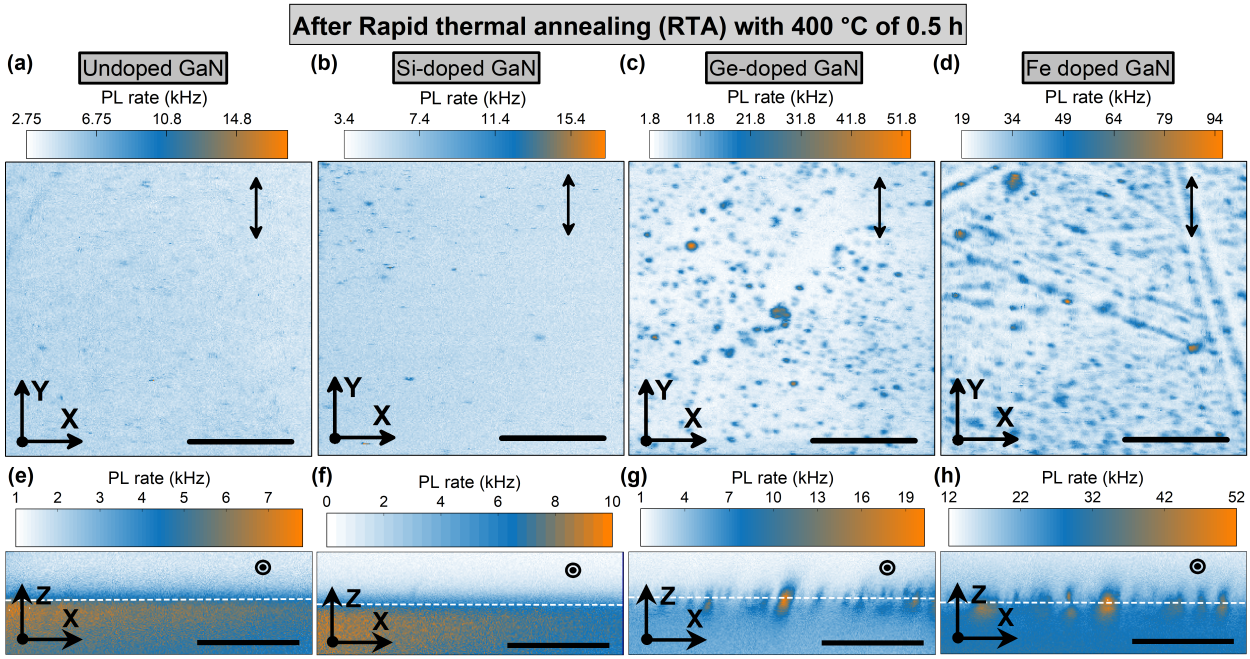

Figure 6.4. Near-surface PL map for free-standing undoped GaN (a, e), Si-doped GaN(b,f), Ge-doping (c,g), and Fe-doped GaN (d,h) after RTA annealing, where the black bars represent the scale of 10 µm. The (a-d) are the x-y PL maps and (e-h) are the x-z PL maps with excitation polarisation laser along the y-axis, where the white dashed lines represent the surface of the GaN samples.

where the $\rho = C_{\text{signal}}/(C_{\text{signal}}+C_{\text{background}})$ is the ratio of signal and total emission. The $C_{\text{background}}$ is the background emission at $1\,\mu\text{m}$ around QEs[80]. By taking $\rho = 0.9$, the $g_*^{(2)}(0)$ are 0.36 and 0.20 for QE-Ge and QE-Fe which is well below 0.5, suggesting they are single photon emitters.

Another signature of a quantized emitter is its photoluminescence (PL) intensity saturation with CW excitation. In Figs. 6.3(g-h), the power-dependent PL emission is fitted by equation 3.2. In general, QE-Ge and QE-Fe show over $400\,\text{kHz}$ under several milliwatts of laser power which is comparable with the QEs in GaN with foreign substrate[56, 76].

6.2.3 After annealing

The GaN samples are further annealed at 400 °C for 0.5 h in a rapid thermal annealing (RTA) approach to check the thermal effect for QEs. From the PL maps for these four samples in Figs. 6.4(a-h), there is no obvious change compared to PL maps before annealing in Fig. 6.4. The background emission of the annealed samples is lower, which I ascribe to an expected reduction in internal strain due to the annealing. Compare the PL map for Fe-doped GaN before annealing, more emitters are formed along the lines in the Fe-doped sample. The annealing process results in the diffusion of vacancies and impurities which yields the emitters. More importantly, there are

still no stable emitters found in undoped GaN and Si-doped GaN, while dense QEs remain active in Ge-doped GaN and Fe-doped GaN. In this case, I conclude that QEs in GaN are more likely to link to extrinsic impurities and dislocation, compared to the thermal effect in this chapter. In other words, the QEs observed in this chapter are ascribed to Fe-related and Ge-related defects in the GaN.

6.3 Conclusion and outlook

I discovered the native QEs in free-standing single crystal GaN, proving that native QEs exist on the GaN at room temperature. The QEs domain in the near-surface of the GaN sample indicates the surface polish damage and the interface provides a necessary condition for QEs. The background emission study of Fe-doped GaN substrate suggests some ensemble emitters in the NIR range. The doping-dependent QEs reveal these QEs are tentatively ascribed to be Ge-related and Fe-related defects. This study reveals important information for the fabrication and theoretical atomic structure prediction of QEs in GaN. Moreover, combined with the future photodynamic study, the origin of these QEs would be determined. Future work should focus on Ge and Fe controlling doping and ion implantation in GaN with suitable annealing processes. This study will pave the way for creating the quantum emitters in GaN deterministically, which is crucial for future GaN-based integrated photonics circuits. Some theoretical works are also needed to further elucidate the nature of QEs.

Chapter 7

Laser-written quantum emitters in gallium nitride

7.1 Highlight

GaN hosts various single-photon QEs with sharp ZPLs in ultraviolet, visible, and telecom ranges, which is a promising quantum light source at room temperature. However, it is crucial to scalably and precisely fabricate the QEs for quantum photonic circuits. In this chapter, I fabricate an array of QEs in free-standing GaN via femtosecond laser writing and subsequent annealing. The QEs show antibunching behaviour in their PECS at room temperature. This study provides important information for the creation mechanism of QEs in GaN indicating a promising way to create QEs in GaN deterministically.

7.2 Introduction

In the last decade, QEs, in GaN have been an attractive field due to their comparatively high DW factor at room temperature [174]. These QEs with low multi-photon emission probability and high CW photon detection rate are promising room-temperature quantum light sources[174, 56, 76, 175]. Recently, optical resonance excitation and ODMR have been observed in QEs of GaN[77, 78], leading to their potentiality in quantum sensing and computation. However, the scalable fabrication of QEs in GaN is still a challenge, and it is a significant and necessary step to integrate those systems into functional nanophotonics and electronics structures[182]. The conventional approaches, such as ion implantation and doping growth[181, 178, 172], would create QEs with random positions and

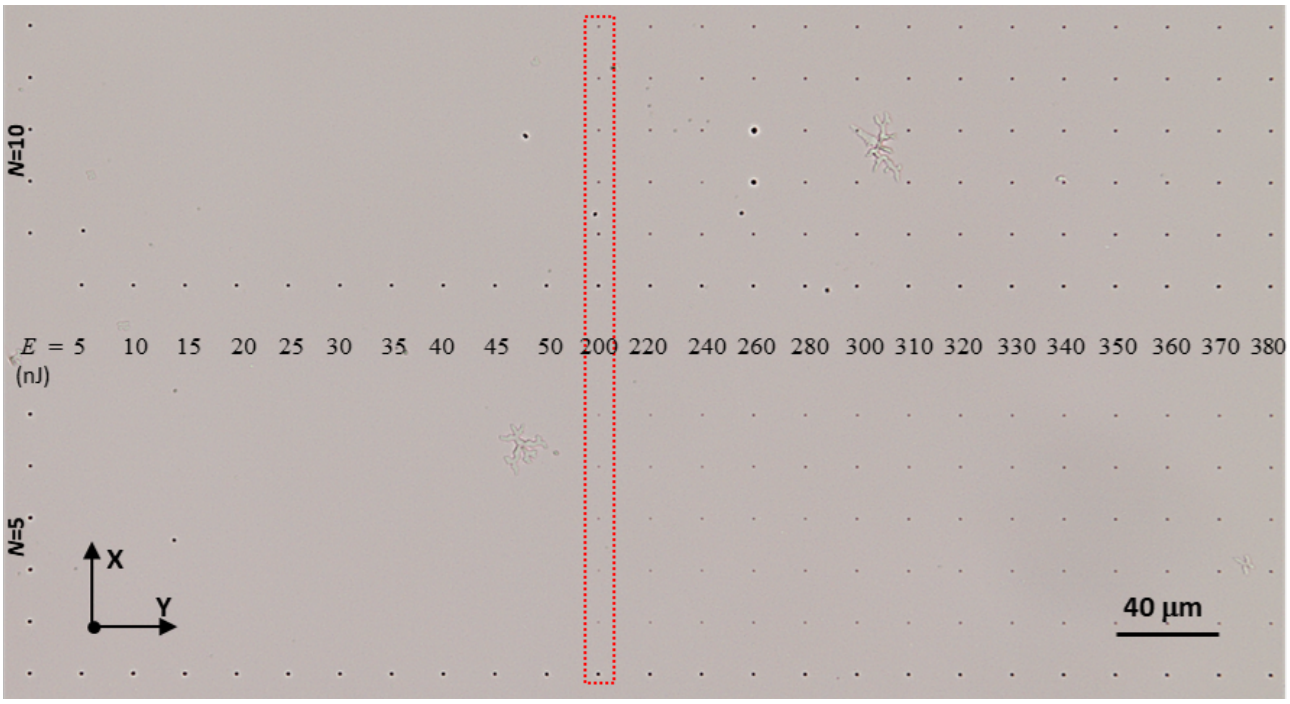

Figure 7.1. Microscopy of laser writing set of N=5, 10 in GaN

residual lattice damage[81]. This would further degrade the spin and optical coherence properties. Recently, femtosecond laser writing fabrication has attracted intense attention for its precise and highly controlling creation of QEs in semiconductors, such as diamond[103], SiC[109], hBN[107, 108], and AlN[75]. Moreover, these laser-written QEs show excellent spin coherence properties as the native counterparts in the host material[94]. The previous studies reported the PL emission from laser-induced ablation[183, 184], while no quantum light source has been found. Thus it is crucial to engineer the quantum light source via the promising tool of laser writing.

In this chapter, I used femtosecond laser writing and subsequent annealing to fabricate the array of QEs in GaN. I studied the laser-induced damage threshold (LIDT) inside GaN via various laser writing parameters. The laser-written QEs show antibunching in their PECS and shelving behaviour on their TRPL measurements. Bright quantum emission of few MHz PL rates have been observed in these laser-written QEs. The spectral and saturation behaviours during the different annealing processes have been recorded to investigate the creation dynamics mechanism of laser-written QEs. This study would pave a promising way for scalable, integrated on-chip quantum technologies based on GaN via laser writing.

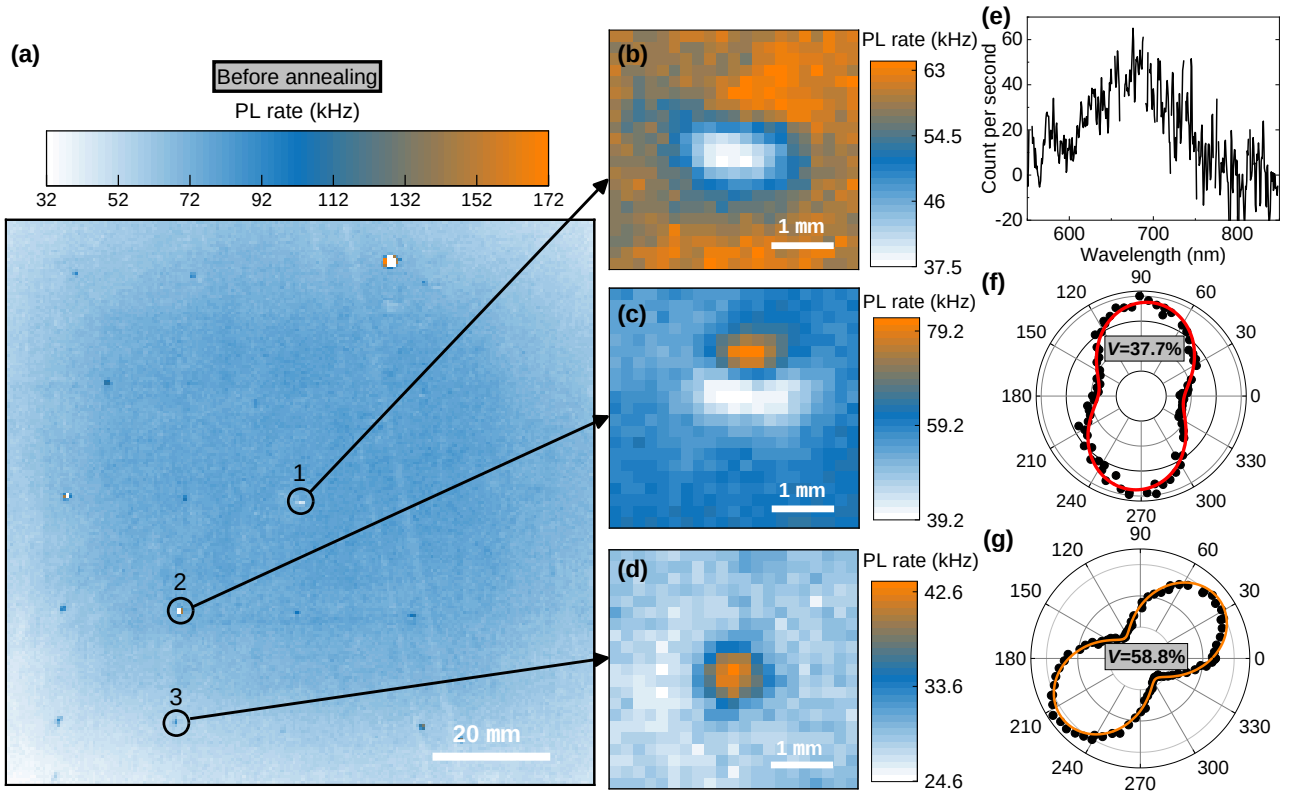

Figure 7.2. The PL study of laser-written GaN before any annealing process. (a) PL maps of laser-written GaN. (b-d) are the high-resolution PL maps of the laser-written areas labelled as 1-3, respectively in (a). (e) represents the spectrum of emitters in (d). (f) and (g) are the excitation polarisation plots for the emitters in (c) and (d), respectively

7.2.1 Femtosecond laser writing fabrication on GaN

The sample used in this experiment is a free-standing single-crystal nominally undoped GaN substrate with (0001) C plane purchased from MSE Supplies. A commercial femtosecond laser (Menlo Systems BlueCut) that produces linearly polarised pulses with a wavelength of 515 nm (second harmonic), repetition rate of 500 kHz, and a duration of 300 fs was used for femtosecond laser writing in Politecnico di MILANO. A 100× oil immersion objective with NA=0.9 was used to focus the laser beam in GaN at a depth of $30\,\mu\mathrm{m}$. I note that the laser heating during the fabrication would induce bubbles in the oil between the objective and GaN substrate, resulting in the misalignment of the laser beam. Therefore, the fabrications were all done without the oil. The pulse energy was controlled using a combination of a motorized half-wave plate and a fixed linear polariser. There are four different laser fabrication sets with laser exposure pulses number of N = 1, 2, 5, 10, respectively. In each set, the laser energies are spaced with $20\,\mu\mathrm{m}$ from E = 5, 10, 15, 20, 25, 30, 35, 40, 45, 50, 200, 220, 240, 260, 280, 300, 310, 320, 330, 340, 350, 360, 370, 380, 390, 400, 410, 420, 430, 440, 450, 460, 470, 480, 490, 500, 510 nJ, where there are 5 trials for each laser writing parameters. From the microscopy of the laser-writing pulse N= 5, 10 regions of GaN in Fig. 7.1, the LIDT is between 50-200 nJ. The same LIDT is also found for laser writing pulse N = 1, 2 under a high-resolution microscopy image. The number of laser pulses doesn't affect the LIDT which is determined by the nature of the substrate[183].

7.2.2 PL study on laser-written GaN before annealing

A homebuilt confocal setup (see section 2.2.1) was used to study the PL emission for the laser-written GaN sample before any annealing process. A 532 nm laser was used to excite the laser fabrication region, and its PL emission was collected by detectors after a 532 nm optical long pass filter. The invisible laser-written spots in Fig . 7.1 are unable to be resolved from their PL maps. However, as shown in Fig. 7.2(a), the regular emitters grids have been observed from the visible laser-written damaged area in the GaN substrate. The PL emission of these laser-written spots is not a large signal relative to the background with a small dependence on the laser energy which is consistent with previous studies[184]. Basically, there are three different cases in the laser-written regions. First, some laser-written spots show a dark centre in the fabrication region as shown in Fig. 7.2(b). Some display a dark centre with a nearby bright emitter as shown in Fig. 7.2(c). I expect that these dark centres are due to the laser writing causing structure deterioration of the GaN Crystal. Some laser-written areas only feature a bright emitter. Whatever the emitters in the case of Figs. 7.2(c) or (d), they exhibit a broad emission from 550-800 nm without a clear ZPL, as shown in Fig. 7.2(e). I state that the spectrum signal suffers a significant loss compared to the signal obtained

from confocal scanning in Fig. 7.2(c-d) due to a suboptimal alignment of the spectrometer system. They also show optical dipolar-like excitation polarization properties with good visibility, as shown in Figs 7.2(f) and (g). The excitation polarisation plots were fitted by the equation 5.1. Their viability V of 37.7% and 58.8% for emitters in Fig. 7.2(c) and (d) were calculated by the equation 5.2

However, no antibunching or bunching behaviours were found in their PECS. And their PL emissions are linearly scaling with excited laser power. Thus, these bright spots appear to be some optically active structural dislocation that lacks further annealing activation to form stable QEs. Or it is a number of emitters within the size of the laser spot which is being probed.

7.2.3 PL study on laser-written GaN after annealing

A series of annealing processes are developed via a RTA approach. After the first 0.5 h of 400°C annealing, the invisible laser-written spots remain unresolvable, while the visible laser-written areas in Fig. 7.1 are getting brighter in Fig. 7.3(a), leading to a good PL contrast compared to Fig. 7.2(a). Most of the laser-written emitters show similar properties as the emitters in Fig. 7.2 (d), exhibiting dipolar-like excitation polarisation, a broadband spectrum from 550-800 nm, and weak dependence on laser power. However, some blinking emitters are found on the edge of laser-written spots as shown in Fig. 7.3(b), and close to the surface of the substrate as shown in Fig. 7.3(c). More importantly, they show antibunching in their PECS. However, these QEs are highly unstable and suffer photo-bleaching which makes them unable to collect their spectra.

After the second 0.5 h of 400°C annealing, it is possible to find more weak QEs appearing in the laser-written region, with a weak antibunching. Their spectra are still around 550-800 nm but with a few weak peaks. The power-dependent PL shows the saturation behaviour. After the third 0.5 h of 400°C annealing, I found some stable and bright emitters around the laser-written region as shown in Fig. 7.4(a). For example, QE 1 in Fig. 7.4(b) is resolved in the laser-written region with MHz PL rate, showing a clear antibunching signal in its PECS in Fig. 7.4(c). This is the direct evidence that laser writing created quantum emitters in GaN. The $g^{(2)}(\tau)$ data is shown using the empirical equation 3.1. The fitting parameters are shown in table 7.1.

Moreover, other dimmer emitters like QEs 2-4 couldn't exhibit the antibunching or bunching in their PECS. To understand their photodynamics, in Fig. 7.4(d), I investigated their TRPL spectra under square laser pulse excitation. TRPL was binned with 1 ns resolution. The spacing between each laser pulse train was $50\,\mu s$ to reset the ground state population of QEs. The background signal is linear scaling with the laser power, therefore their TRPL shows the exact excited laser responding to the AOM. However, any PL emission of QEs is defined by its excited state lifetime and shelving process[143, 80]. In Fig. 7.4(d), the measured PL relates to the population in the excitation state

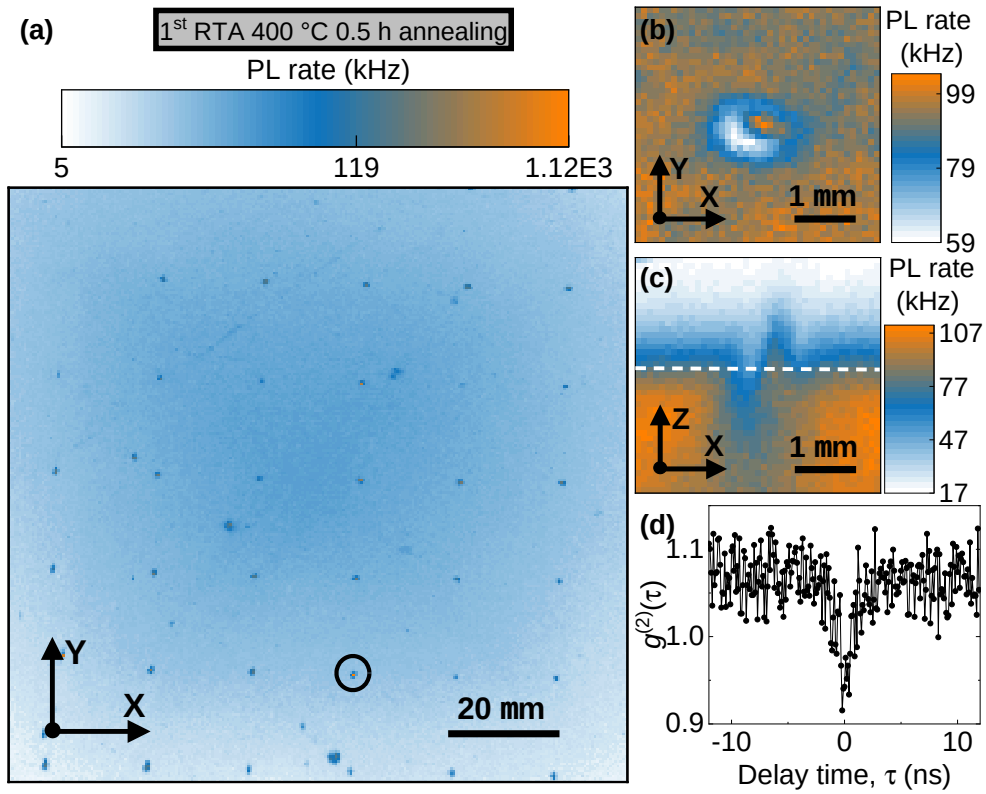

Figure 7.3. The PL study of laser-written GaN after the first 0.5 h of 400°C. (a) PL maps for laser-written GaN. (b) and (c) are the x-y and x-z PL maps of the laser-written grids marked in (a) where the white dashed line represents the GaN substrate surface. (d) is the PECS of the QEs in (a-c)

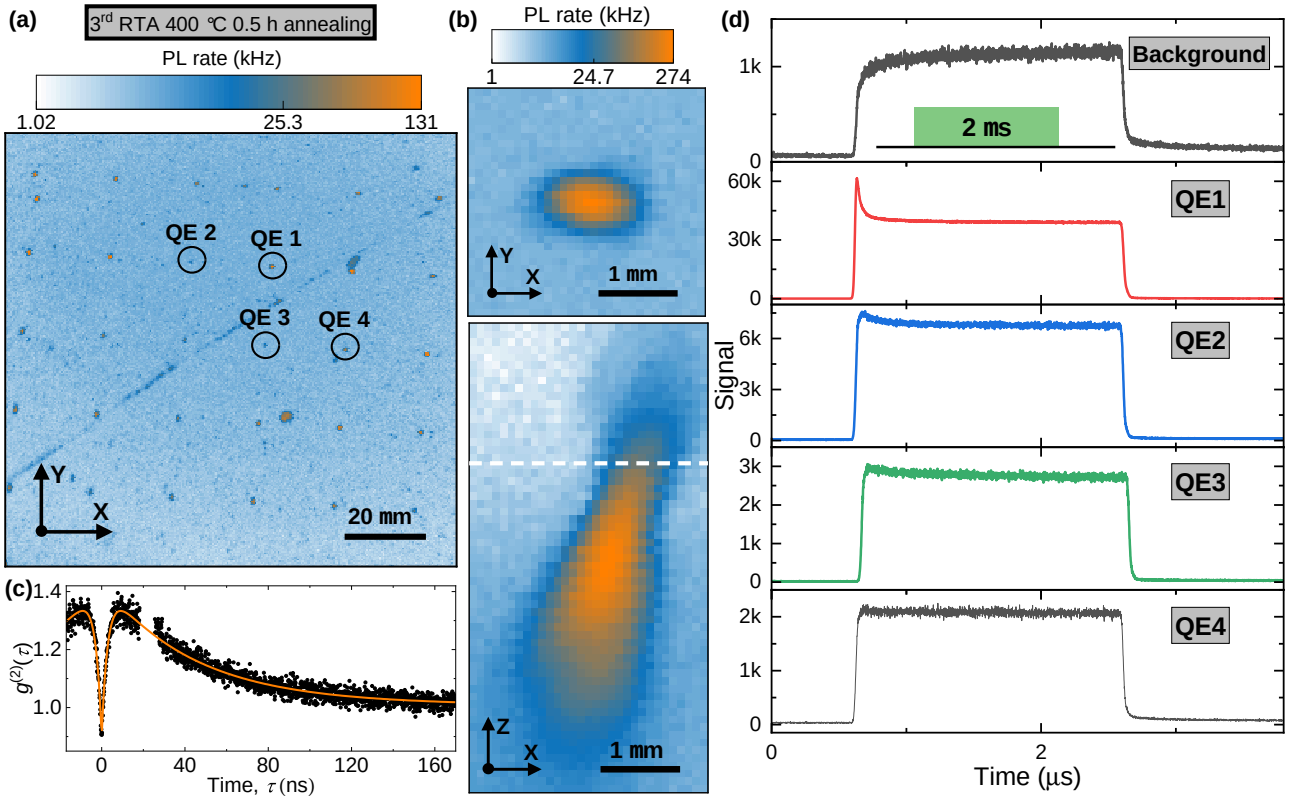

Figure 7.4. PL study of laser-written GaN after the third 0.5 h of 400°C RTA annealing. (a) x-y PL map of laser-written GaN, where some emitters around the laser-written area are labelled as QE 1-4 for the discussion in (b-d). (b) is the x-y (upper plate) and x-z (lower plate) PL maps for QE 1 labelled in (a) where the white dashed line represents the GaN substrate surface. (c) PECS for QE 1. (d) TRPL measurement for QE 1-4 and background under a square excited laser pulse, where the insert cartoon is the train for laser pulses.

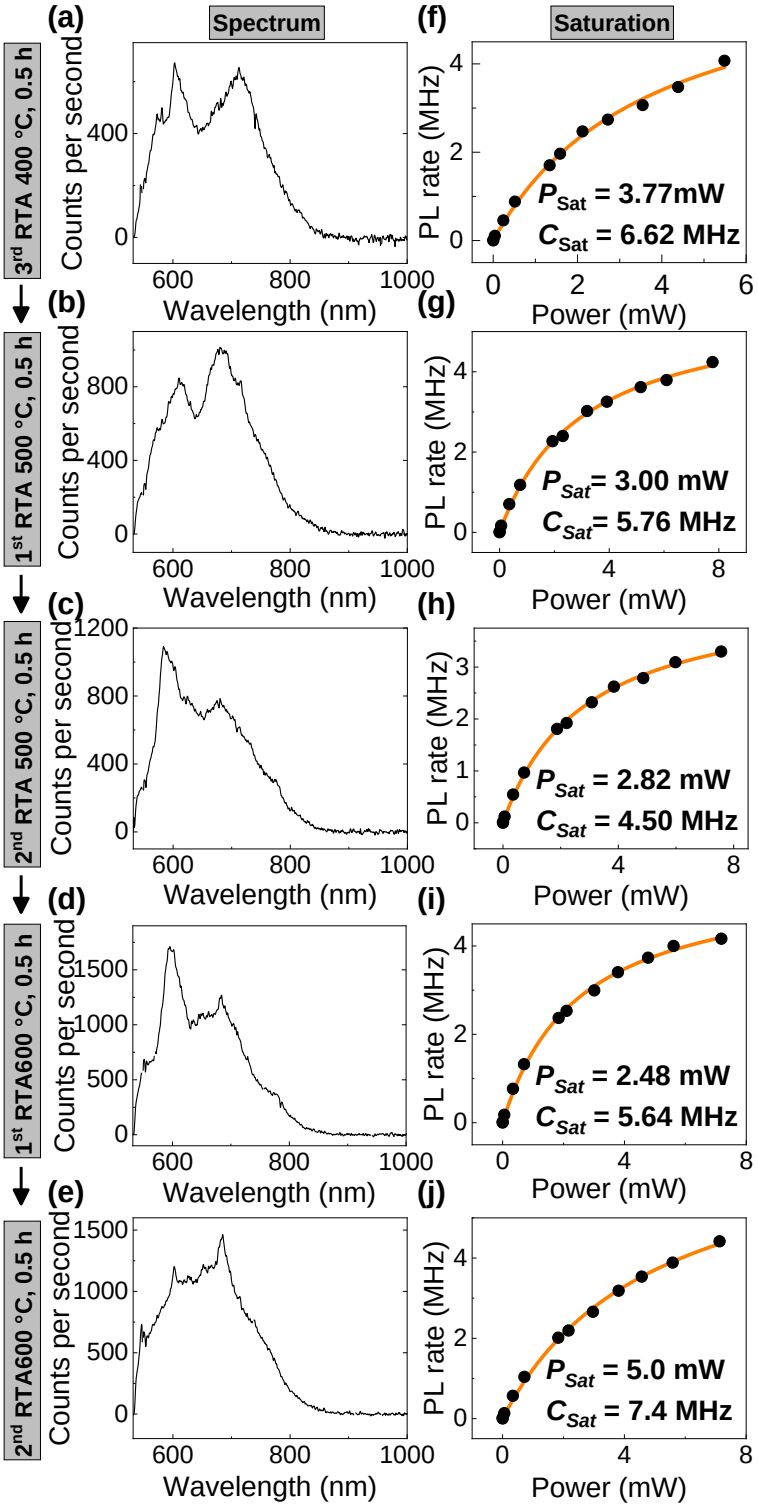

Figure 7.5. The spectra (a-e) and power-dependent PL saturation behaviours (f-j) for QE 1 during the RTA annealing.

Table 7.1. Fitting parameters of $g^{(2)}(\tau)$

Parameters	Value	Standard Error
C_1	0.54	0.005
τ_1 (ns)	2.90	0.06
C_2	0.42	0.003
τ_2 (ns)	42.93	0.59
C_3	0.019	0.002
τ_3 (ns)	290.84	56.46

which relies on the population in the ground state at the beginning of the laser pulse. Therefore, for example, QE 1 exhibits a very sharp rise at the beginning of laser pulses due to the laser-pumped occupation on its excitation state and follows an exponential decay until a steady state is reached due to the shelving process, which also responds to the bunching behaviour of QE 1 in Fig. 7.4(c). For the dimmer emitters QE 2-3, I can see very small decay during the laser excitation in Fig. 7.4 (d). I conclude that the shelving process prevails in laser-written emitters, implying their atomic-like energy structures, while their weak emission could be ascribed to their unstable atomic structure due to residual lattice damage.

I further record the spectra and PL saturation behaviours of QE 1 during further high-temperature RTA annealing. I observed that the spectrum changed a lot during the annealing. There are two peaks in 600 nm and 700 nm whose intensities have been strongly affected via RTA annealing. This highlights the dynamic processes of creation and annihilation for different species of QEs in laser-written spots. It seems that after 3 times 0.5 h of 400°C, 2 times 0.5 h of 500°C, and one time 0.5 h of 600°C annealing, a sharper peak is resolved at a wavelength of 600 nm. Another signature of a quantized property is its PL intensity saturation with CW excitation. In Figs. 7.5(f-j), the power-dependent PL emission is fitted by equation 3.2. In general, the P_{sat} decreases with the annealing process until the second time 0.5 h of 600°C annealing. This implies that the laser-written emitter becomes more quantized after the annealing process. In other words, the laser-written emitter is getting more effectively saturated with decreased P_{sat}, which might indicate the annealing process makes the emitters get further thermal diffusion resulting in more quantized (or ordered) PL emission. This is also consistent with the spectra dynamics in Figs. 7.5(a-e). After the second 0.5 h of 600°C, the spectrum lost the sharp peak which indicates damage from some over-annealing. Similarly, the P_{sat} increased to $7\,\mathrm{mW}$ after the second 0.5 h of 600°C RTA annealing. These results conclude that 0.5 h of 600°C RTA annealing might be a threshold for the creation of stable quantum emitters.

7.2.4 Discussion for emitters' yield

All the laser fabrication areas are scanned with a fixed excited laser power $\sim$ 2.2 mW to study the emitters' yield. First of all, there is no obvious PL emitters in laser-written areas when the laser fabrication energy is below LIDT, as mentioned in section 7.2.1. On other words, the PL emission is only found around the laser-induced visible damage region. After the LIDT, the laser pulse numbers play an important role for PL intensity. There is less than 4% laser-written regions in laser pulse number N=1 showing resolved PL emission. A 33% is for the laser pulse number N=2, and over 97% for both the laser pulse number N=5 and N=10. Moreover, the PL intensity of laser-written emitters also increases as the laser pulse number increases. In general, the laser pulse numbers N=1 and N=2 region exhibit PL emission around $10\,\mathrm{kHz}$. And the laser pulse numbers N=5 and N=10 region exhibit PL emission over $10\,\mathrm{kHz}$ with weak relation to the laser energy. Only 5% of emitters feature over $1\,\mathrm{MHz}$ saturation PL emission. The reason for this relatively low yield is, probably, from the complex recovery and annihilation during the RTA annealing. Thus, a future precise controllable annealing process is needed to improve the yield of bright laser-written QEs in GaN, such as real-time PL-tracked annealing.

7.3 Conclusion and outlook

In this chapter, I reported the array of engineered QEs in GaN via femtosecond laser writing and followed RTA annealing. Some bright QEs with MHz emission rates are deterministically created in the laser-written region. The PL emission dynamics are tracked during the annealing process. 500-600°C is considered a suitable temperature to activate the laser-written QEs. This study paves a promising way to scalably engineer the QEs which is a crucial step for advanced integrated quantum circuits. Future works should focus on increasing the yield of laser-written QEs, optimizing the annealing process, and fabricating the quantum emitters at a single level.

Chapter 8

Conclusion

8.1 Thesis overview and key results

In this thesis, I investigated the well-understood NVs in diamond and studied the novel QEs in AlN and GaN. In the NVs chapter 3, I did a fine characterization of the spin coherence properties of laser-written WGINVs, showing the comparable spin coherence time as native NVs in diamond. The laser writing fabrication does not degrade the spectral and spin coherence properties. In contrast, the conventional fabrication of NVs, such as ion implantation or electron radiation, would inevitably introduce residual damage along the focused beam direction. This residual damage either breaks the crystal lattice or the impurities, which eventually deteriorate the spin coherence time, such as T_2 less than $10\,\mu s$. Compared to native NVs (Or NVs engineered via crystal growth) in diamond, this laser writing method allows for the deterministic fabrication of NVs from single to ensemble level at a μm scale. These precisely controllable fabrications pave a promising way for engineering NVs in the photonics structure, which is crucial for photonics-integrated quantum circuits.

In chapter 4, an enhanced quantum sensor based on ensemble WGINVs is demonstrated by a fibre-waveguide-fibre configuration resulting in at least a 10-fold sensitivity improvement compared to the conventional confocal configuration. This sensing approach provides a way to excite and collect the ensemble NVs in a larger volume ($5\,\mu m \times 5\,\mu m \times 2.8\,mm$). It achieves 100 times PL emission compared to the conventional confocal method by effectively probing a large volume of ensemble NVs. Moreover, the laser-written waveguide doesn't greatly introduce an extra decoherence source to obtain comparable spin coherence properties for NVs in pristine and waveguide regions. Combine these two factors, a sensitivity of η_{dc}=$56\,pT \cdot Hz^{-1/2}$ and η_{ac}=$18\,pT \cdot Hz^{-1/2}$ are acheived. This micron waveguide-integrated sensing device shows more than an order of magnitude sensitivity than the hall sensor[185] at the same scale. And compared to the SQUID, this diamond can work at room

temperature with lower cost and energy consumption.

Regarding the QEs in AlN, in chapter 5, I revealed their complex internal energy levels, studied their photodynamics by PECS and TRPL, and demonstrated the laser-driven deshelving process for the bright QEs in AlN. This study provides important information for future quantum information processing protocols. First of all, the complex internal energy level and multiple shelving states indicate that the tunable shelving processes might be able to feature a similar spin-selective transition as NVs in diamond. Moreover, this photodynamics study also helps to understand the PL behaviour of QEs, contributing to finding a way to enhance the quantum efficiency of QEs by minimising the time QEs spend in shelving states. Last but not least, the study of these transitions provides important information for future theoretical work to identify the origin of these QEs.

In chapter 6, I discovered the native quantum emitters in free-standing GaN which might be the Ge-related and Fe- related defects. Compared to the previous studies on the QEs in the GaN thin film, this work reliably confirms the existence of QEs in the GaN complex. Moreover, the discovery of Ge-related and Fe-related QEs also indicates a promising way for the efficient creation of QEs via doping and ion implantation.

In the last research chapter 7, I summarise my effort in engineering the QEs in GaN with femto-second laser writing. An array of quantum emitters is formed via laser writing. Compared to the previous studies on the femtosecond laser writing of QEs in GaN, the laser-written QEs in this thesis exhibit the important the antibunched emission which initiates a possibility to engineer the single-photon emitters, paving the way to deterministically fabricate the QEs in GaN. Shelving dynamics are observed in these QEs, showing at least three energy levels.

In conclusion, QEs in three different wideband gap semiconductors (diamond, AlN, and GaN) are investigated in this thesis. It's hard to claim which semiconductor is the perfect host for the QEs or which QEs is the perfect emitter to meet demand for all quantum applications. NVs in diamond feature stable PL emission, long coherence time ($T_2 > 0.5$ ms), and mature quantum control techniques. However, NVs also exhibit relatively poor spectral properties. First of all, its longer excited state lifetime ($\sim 12\,\mathrm{ns}$) determinates low staturation PL emission of 30-$50\,\mathrm{kHz}$ under a confocal setup of NA = 0.9.objective. This is 10 -20 times less than that of QEs in AlN and GaN. Moreover, the 3% DW factor of NVs is 10 times less than that of QEs in AlN and GaN, which reduces coherent photon generation for advanced quantum applications, such as spin-photon interference-based quantum networks. Therefore, compared to the novel QEs in AlN and GaN, NVs have more potential for spin-based quantum sensing, perfectly with integrated photonics structure to enhance their PL emission. The novel QEs in AlN and GaN are expected to be better single-photon sources than NVs. However, one of the biggest challenges in these QEs is that the origins of these QEs are still unknown. This inherently hinders its fabrication and quantum control protocol. A few

useful works and ideas are listed in the next section 8.2.

8.2 Future work

This thesis also proposes several ideas for future work. First, optimizing the laser writing parameters and annealing process could enhance NV yield and reduce the non-NV spin noise to improve NVs density and spin coherence properties, paving the way for high-sensitivity sensing using low-cost Ib diamonds. For example, higher laser writing powers will produce higher-density vacancy which combines native nitrogen to form high-density NVs. Similarly, increased laser flux, such as lower scan speed and higher laser pulse repetition, will also induce increased vacancies in diamond. Another key thing is using a suitable annealing process, for example, annealing temperature, annealing duration time, heating and cooling dynamics. Laser in situ annealing is also a promising method which can monitor the PL emission of NVs in real-time. It is also possible to combine laser writing techniques with the CVD diamond growth process. For example, future laser writing fabrication could employ a different type of diamond whose NVs density and crystal lattice quality can be controlled by the CVD growth process.

Second, WGINVs on-chip sensors can be easily integrated into microfluidic devices for biological sensing, offering high sensitivity for real-world applications. The fibre-waveguide-fibre configuration could be upgraded to improve the coupling efficiency, for example, by testing different types of optical fibre and changing the confinement of the laser-written waveguide. The readout fidelity could also be improved by excitation laser absorption and near-infrared absorption assisting readout[15]. The sensitivity could be improved by the advanced sensing protocol. For example, reduced sensing overhead time, increased readout fidelity, and optimal dynamic decoherence sensing protocol all contribute to better sensitivity [132]. For frequency domain ODMR sensing, the lock-in amplifier could also be used to suppress the fast noise. Some other high-quality laser-written photonics circuits are also worthy of being developed for specific applications. At the same time, the techniques used in NVs in diamond would be interesting to study other QEs-rich hosts like AlN, GaN, SiC, and hBN.

Regarding QEs in AlN, it's still a very young field. Compared to the NVs, there are many things unknown, which bring a lot of challenges and opportunities. First of all, the photodynamics study on the QEs in AlN suggests many tunable shelving processes which haven't been fully defined in their manifold structures. These processes are likely relative to optically driven charge state dynamics or ISC mechanisms governed by different spin manifolds. Therefore, it's interesting to study the ODMR response with the QEs in AlN. In this case, QEs in AlN can be used as another room-temperature qubit as NVs for quantum sensing. Conducting PLE studies would shed light on

emitters' charge state dynamics and help pinpoint the position of QEs within the semiconductor's wide bandgap. This crucial information will not only illuminate the way to improve emitters' quantum efficiency but also support theoretical predictions about the origin of these QEs. Lately, the resonance excitation of these QEs in AlN is another very important step for the study of thier optical coherence properties, which is crucial for spin-photon interference in quantum network applications.

QEs in GaN have attracted a lot of attention due to the recent progress of over 20% ODMR contrast and optical resonance excitation. Compared to NVs, QEs in GaN exhibit 10-20 times higher saturation PL emission, 10 times higher DW factor, and mature host material fabrication. This makes the QEs in GaN has emerged as the next promising room-temperature platform for quantum sensing and quantum networking. For example, the iterations between the QEs and external temperature, pressure and electric field are still unclear. Therefore, it is very worthwhile to study the ODMR dependent on these physical quantities to expand its quantum applications. However, the origin of these QEs is under debate. Future research should also focus on the identification of these QEs via the joint effort of fabrication process and theoretical prediction. Based on the studies from this thesis, these doping-induced and laser-written QEs would be interesting to inspect thier ODMR signal. Moreover, it's important to continue conducting controllable doping and ion implantation, optimizing the laser-written parameter to realize scalable fabrication of these QEs. It's also worthy conducting some material characterisation to understand the formation dynamics of these QEs, such as transmission electron microscopy (TEM), scanning electron microscopy (SEM) and atomic force microscopy (AFM). Last but not least, some photodynamic studies and theoretical works are also needed to determine the origin of these defects.

Bibliography

[1] Michael A. Nielsen and Isaac L. Chuang. *Quantum Computation and Quantum Information: 10th Anniversary Edition*. Cambridge University Press, 2010. DOI: 10.1017/CBO9780511976667.

[2] Richard P Feynman. "Simulating physics with computers". In: *International Journal of Theoretical Physics* 21 (1982), pp. 467–488. DOI: 10.1007/BF02650179. URL: https://link.springer.com/article/10.1007/BF02650179.

[3] David P DiVincenzo. "The physical implementation of quantum computation". In: *Fortschritte der Physik: Progress of Physics* 48.9-11 (2000), pp. 771–783. DOI: 10.1002/1521-3978(200009)48:9/11<771::AID-PROP771>3.0.CO;2-E. URL: https://onlinelibrary.wiley.com/doi/abs/10.1002/1521-3978%28200009%2948%3A9/11%3C771%3A%3AAID-PROP771%3E3.0.CO%3B2-E.

[4] P.W. Shor. "Algorithms for quantum computation: discrete logarithms and factoring". In: *Proceedings 35th Annual Symposium on Foundations of Computer Science*. 1994, pp. 124–134. DOI: 10.1109/SFCS.1994.365700.

[5] Tycho Sleator and Harald Weinfurter. "Realizable Universal Quantum Logic Gates". In: *Phys. Rev. Lett.* 74 (20 May 1995), pp. 4087–4090. DOI: 10.1103/PhysRevLett.74.4087. URL: https://link.aps.org/doi/10.1103/PhysRevLett.74.4087.

[6] Wen Yang, Wen-Long Ma, and Ren-Bao Liu. "Quantum many-body theory for electron spin decoherence in nanoscale nuclear spin baths". In: *Reports on Progress in Physics* 80.1 (Nov. 2016), p. 016001. DOI: 10.1088/0034-4885/80/1/016001. URL: https://dx.doi.org/10.1088/0034-4885/80/1/016001.

[7] Nan Zhao, Sai-Wah Ho, and Ren-Bao Liu. "Decoherence and dynamical decoupling control of nitrogen vacancy center electron spins in nuclear spin baths". In: *Phys. Rev. B* 85 (11 Mar. 2012), p. 115303. DOI: 10.1103/PhysRevB.85.115303. URL: https://link.aps.org/doi/10.1103/PhysRevB.85.115303.

[8] Google Quantum AI et al. "Quantum error correction below the surface code threshold". In: *Nature* 638.8052 (2024), p. 920. DOI: 10.1038/s41586-024-08449-y. URL: https://www.nature.com/articles/s41586-024-08449-y.

[9] Sergey Bravyi et al. "High-threshold and low-overhead fault-tolerant quantum memory". In: *Nature* 627.8005 (2024), pp. 778–782. DOI: 10.1038/s41586-024-07107-7. URL: https://www.nature.com/articles/s41586-024-07107-7.

[10] C. L. Degen, F. Reinhard, and P. Cappellaro. "Quantum sensing". In: *Reviews of Modern Physics* 89.3 (July 2017), p. 035002. ISSN: 0034-6861. DOI: 10.1103/RevModPhys.89.035002. URL: http://link.aps.org/doi/10.1103/RevModPhys.89.035002.

[11] Gang-Qin Liu et al. "Demonstration of entanglement-enhanced phase estimation in solid". In: *Nature Communications* 6.1 (2015), p. 6726. DOI: 10.1038/ncomms7726. URL: https://www.nature.com/articles/ncomms7726?utm_source=chatgpt.com.

[12] Vittorio Giovannetti, Seth Lloyd, and Lorenzo Maccone. "Advances in quantum metrology". In: *Nature photonics* 5.4 (2011), pp. 222–229. DOI: 10.1038/nphoton.2011.35. URL: https://www.nature.com/articles/nphoton.2011.35.

[13] Jiangfeng Du et al. "Single-molecule scale magnetic resonance spectroscopy using quantum diamond sensors". In: *Reviews of Modern Physics* 96.2 (Apr. 2024). ISSN: 15390756. DOI: 10.1103/RevModPhys.96.025001. URL: https://journals.aps.org/rmp/abstract/10.1103/RevModPhys.96.025001.

[14] L Rondin et al. "Magnetometry with nitrogen-vacancy defects in diamond". In: *Reports on Progress in Physics* 77.5 (May 2014), p. 056503. ISSN: 0034-4885. DOI: 10.1088/0034-4885/77/5/056503. URL: https://iopscience.iop.org/article/10.1088/0034-4885/77/5/056503.

[15] John F. Barry et al. "Sensitivity optimization for NV-diamond magnetometry". In: *Reviews of Modern Physics* 92.1 (Mar. 2020), p. 015004. ISSN: 0034-6861. DOI: 10.1103/RevModPhys.92.015004. URL: https://link.aps.org/doi/10.1103/RevModPhys.92.015004.

[16] A. Dréau et al. "Avoiding power broadening in optically detected magnetic resonance of single NV defects for enhanced dc magnetic field sensitivity". In: *Physical Review B - Condensed Matter and Materials Physics* 84.19 (Nov. 2011). ISSN: 1550235X. DOI: 10.1103/PhysRevB.84.195204. URL: https://journals.aps.org/prb/abstract/10.1103/PhysRevB.84.195204.

[17] Marc A Kastner. "The single-electron transistor". In: *Reviews of modern physics* 64.3 (1992), p. 849. DOI: 10.1103/RevModPhys.64.849. URL: https://link.aps.org/doi/10.1103/RevModPhys.64.849.

[18] Masahiro Kitagawa and Masahito Ueda. "Squeezed spin states". In: *Physical Review A* 47.6 (1993), p. 5138. DOI: 10.1103/PhysRevA.47.5138. URL: https://link.aps.org/doi/10.1103/PhysRevA.47.5138.

[19] Caspar F Ockeloen et al. "Quantum metrology with a scanning probe atom interferometer". In: *Physical review letters* 111.14 (2013), p. 143001. DOI: 10.1103/PhysRevLett.111.143001. URL: https://journals.aps.org/prl/abstract/10.1103/PhysRevLett.111.143001.

[20] Dolev Bluvstein et al. "Logical quantum processor based on reconfigurable atom arrays". In: *Nature* 626.7997 (2024), pp. 58–65. DOI: 10.1038/s41586-023-06927-3. URL: https://www.nature.com/articles/s41586-023-06927-3.

[21] Simon J Evered et al. "High-fidelity parallel entangling gates on a neutral-atom quantum computer". In: *Nature* 622.7982 (2023), pp. 268–272. DOI: 10.1038/s41586-023-06481-y. URL: https://www.nature.com/articles/s41586-023-06481-y.

[22] Robert Maiwald et al. "Stylus ion trap for enhanced access and sensing". In: *Nature Physics* 5.8 (2009), pp. 551–554. DOI: 10.1038/nphys1311. URL: https://www.nature.com/articles/nphys1311.

[23] Han-Sen Zhong et al. "Quantum computational advantage using photons". In: *Science* 370.6523 (2020), pp. 1460–1463. DOI: 10.1126/science.abe8770. URL: https://www.science.org/doi/abs/10.1126/science.abe8770.

[24] C. E. Bradley et al. "A Ten-Qubit Solid-State Spin Register with Quantum Memory up to One Minute". In: *Physical Review X* 9.3 (Sept. 2019). ISSN: 21603308. DOI: 10.1103/PhysRevX.9.031045. URL: https://journals.aps.org/prx/abstract/10.1103/PhysRevX.9.031045.

[25] F. Arute et al. "Quantum supremacy using a programmable superconducting processor". In: *Nature* 574 (2019), pp. 505–510. DOI: 10.1038/s41586-019-1666-5. URL: https://dx.doi.org/10.1088/0034-4885/80/1/016001.

[26] Ming Gong et al. "Quantum walks on a programmable two-dimensional 62-qubit superconducting processor". In: *Science* 372.6545 (2021), pp. 948–952. DOI: 10.1126/science.abg7812. eprint: https://www.science.org/doi/pdf/10.1126/science.abg7812. URL: https://www.science.org/doi/abs/10.1126/science.abg7812.

[27] M. S. Grinolds et al. "Nanoscale magnetic imaging of a single electron spin under ambient conditions". In: *Nature Physics* 9.4 (2013), pp. 215–219. ISSN: 17452481. DOI: 10.1038/nphys2543. URL: https://www.nature.com/articles/nphys2543.

[28] Hannes Bernien et al. "Heralded entanglement between solid-state qubits separated by three metres". In: *Nature* 497.7447 (2013), pp. 86–90. DOI: 10.1038/nature12016. URL: https://www.nature.com/articles/nature12016.

[29] Bas Hensen et al. "Loophole-free Bell inequality violation using electron spins separated by 1.3 kilometres". In: *Nature* 526.7575 (2015), pp. 682–686. DOI: 10.1038/nature15759. URL: https://www.nature.com/articles/nature15759.

[30] Ali W Elshaari et al. "Hybrid integrated quantum photonic circuits". In: *Nature photonics* 14.5 (2020), pp. 285–298. DOI: 10.1038/s41566-020-0609-x. URL: https://www.nature.com/articles/s41566-020-0609-x.

[31] A.M. Zaitsev. *Optical Properties of Diamond: A Data Handbook*. 1st ed. Springer, 2001. ISBN: 354066582X,9783540665823. URL: http://gen.lib.rus.ec/book/index.php?md5=70776e47f35d97097fbec06654909874.

[32] Jan Isberg et al. "High carrier mobility in single-crystal plasma-deposited diamond". In: *Science* 297.5587 (2002), pp. 1670–1672. DOI: 10.1126/science.1074374. URL: https://www.science.org/doi/10.1126/science.1074374.

[33] A Gruber et al. "Scanning confocal optical microscopy and magnetic resonance on single defect centers". In: *Science* 276.5321 (1997), pp. 2012–2014. DOI: 10.1126/science.276.5321.2012. URL: https://www.science.org/doi/10.1126/science.276.5321.2012.

[34] J R Maze et al. "Properties of nitrogen-vacancy centers in diamond: the group theoretic approach". In: *New Journal of Physics* 13.2 (Feb. 2011), p. 025025. ISSN: 1367-2630. DOI: 10.1088/1367-2630/13/2/025025. URL: https://iopscience.iop.org/article/10.1088/1367-2630/13/2/025025.

[35] V. M. Acosta et al. "Temperature Dependence of the Nitrogen-Vacancy Magnetic Resonance in Diamond". In: *Physical Review Letters* 104.7 (Feb. 2010), p. 070801. ISSN: 0031-9007. DOI: 10.1103/PhysRevLett.104.070801. URL: https://link.aps.org/doi/10.1103/PhysRevLett.104.070801.

[36] Marcus W. Doherty et al. "Electronic properties and metrology applications of the diamond NV^- Center under pressure". In: *Physical Review Letters* 112.4 (Jan. 2014). ISSN: 00319007. DOI: 10.1103/PhysRevLett.112.047601. URL: https://journals.aps.org/prl/abstract/10.1103/PhysRevLett.112.047601.

[37] T. Mittiga et al. "Imaging the Local Charge Environment of Nitrogen-Vacancy Centers in Diamond". In: *Physical Review Letters* 121.24 (Dec. 2018), p. 246402. ISSN: 0031-9007. DOI: 10.1103/PhysRevLett.121.246402. URL: https://link.aps.org/doi/10.1103/PhysRevLett.121.246402.

[38] F. Dolde et al. "Electric-field sensing using single diamond spins". In: *Nature Physics* 7.6 (June 2011), pp. 459–463. ISSN: 1745-2473. DOI: 10.1038/nphys1969. URL: https://www.nature.com/articles/nphys1969.

[39] Gopalakrishnan Balasubramanian et al. "Nanoscale imaging magnetometry with diamond spins under ambient conditions". In: *Nature* 455.7213 (Oct. 2008), pp. 648–651. ISSN: 0028-0836. DOI: 10.1038/nature07278. URL: https://www.nature.com/articles/nature07278.

[40] Benjamin S. Miller et al. "Spin-enhanced nanodiamond biosensing for ultrasensitive diagnostics". In: *Nature* 587.7835 (Nov. 2020), pp. 588–593. ISSN: 14764687. DOI: 10.1038/s41586-020-2917-1. URL: https://www.nature.com/articles/s41586-020-2917-1.

[41] G. Kucsko et al. "Nanometre-scale thermometry in a living cell". In: *Nature* 500.7460 (2013), pp. 54–58. ISSN: 00280836. DOI: 10.1038/nature12373. URL: https://www.nature.com/articles/nature12373.

[42] M. Pompili et al. "Realization of a multinode quantum network of remote solid-state qubits". In: *Science* 372.6539 (Apr. 2021), pp. 259–264. ISSN: 0036-8075. DOI: 10.1126/science.abg1919. URL: https://www.science.org/doi/10.1126/science.abg1919.

[43] Changhao Li et al. "SARS-CoV-2 quantum sensor based on nitrogen-vacancy centers in diamond". In: *Nano letters* 22.1 (2021), pp. 43–49. DOI: 10.1021/acs.nanolett.1c02868. URL: https://pubs.acs.org/doi/10.1021/acs.nanolett.1c02868.

[44] Tongtong Zhang et al. "Toward quantitative bio-sensing with nitrogen–vacancy center in diamond". In: *ACS sensors* 6.6 (2021), pp. 2077–2107. DOI: 10.1021/acssensors.1c00415. URL: https://pubs.acs.org/doi/10.1021/acssensors.1c00415.

[45] Yingke Wu and Tanja Weil. "Recent developments of nanodiamond quantum sensors for biological applications". In: *Advanced Science* 9.19 (2022), p. 2200059. DOI: 10.1002/advs.202200059. URL: https://doi.org/10.1002/advs.202200059.

[46] Wesley Wei-Wen Hsiao et al. "Fluorescent nanodiamond: a versatile tool for long-term cell tracking, super-resolution imaging, and nanoscale temperature sensing". In: *Accounts of chemical research* 49.3 (2016), pp. 400–407. DOI: 10.1021/acs.accounts.5b00484. URL: https://pubs.acs.org/doi/10.1021/acs.accounts.5b00484.

[47] Yuzhou Wu and Tanja Weil. "Nanodiamonds for biological applications". In: *Physical Sciences Reviews* 2.6 (2017). DOI: 10.1515/psr-2016-0104. URL: https://doi.org/10.1515/psr-2016-0104.

[48] P Neumann et al. "Multipartite entanglement among single spins in diamond". In: *science* 320.5881 (2008), pp. 1326–1329. DOI: 10.1126/science.1157233. URL: https://www.science.org/doi/10.1126/science.1157233.

[49] Norbert Kalb et al. "Entanglement distillation between solid-state quantum network nodes". In: *Science* 356.6341 (2017), pp. 928–932. DOI: 10.1126/science.aan0070. URL: https://www.science.org/doi/10.1126/science.aan0070.

[50] Wolfgang Pfaff et al. "Unconditional quantum teleportation between distant solid-state quantum bits". In: *Science* 345.6196 (2014), pp. 532–535. DOI: 10.1126/science.1253512. URL: https://www.science.org/doi/full/10.1126/science.1253512?casa_token=ZZ_G487YHqsAAAAA%3AZwQv9kjXH0ZGUJU63_NHI_3flcnPEFZ1SVVLecQKvgm5xn28Baw6

[51] C Delle Donne et al. "An operating system for executing applications on quantum network nodes". In: *Nature* 639.8054 (2025), pp. 321–328. DOI: 10.1038/s41586-025-08704-w. URL: https://www.nature.com/articles/s41586-025-08704-w.

[52] Eric I Rosenthal et al. "Microwave spin control of a tin-vacancy qubit in diamond". In: *Physical Review X* 13.3 (2023), p. 031022. DOI: 10.1103/PhysRevX.13.031022. URL: https://link.aps.org/doi/10.1103/PhysRevX.13.031022.

[53] Isaac B. W. Harris and Dirk Englund. "Coherence of group-IV color centers". In: *Phys. Rev. B* 109 (8 Feb. 2024), p. 085414. DOI: 10.1103/PhysRevB.109.085414. URL: https://link.aps.org/doi/10.1103/PhysRevB.109.085414.

[54] Carlo Bradac et al. "Quantum nanophotonics with group IV defects in diamond". In: *Nature Communications* 10.1 (Dec. 2019). ISSN: 20411723. DOI: 10.1038/s41467-019-13332-w. URL: https://www.nature.com/articles/s41467-019-13332-w.

[55] Toan Trong Tran et al. "Quantum emission from hexagonal boron nitride monolayers". In: *Nature nanotechnology* 11.1 (2016), pp. 37–41. DOI: 10.1038/nnano.2015.242. URL: https://www.nature.com/articles/nnano.2015.242.

[56] Amanuel M. Berhane et al. "Bright Room-Temperature Single-Photon Emission from Defects in Gallium Nitride". In: *Advanced Materials* 29.12 (Mar. 2017), p. 1605092. ISSN: 0935-9648. DOI: 10.1002/adma.201605092. URL: https://onlinelibrary.wiley.com/doi/10.1002/adma.201605092.

[57] Alexander Kubanek. "Coherent quantum emitters in hexagonal boron nitride". In: *Advanced Quantum Technologies* 5.9 (2022), p. 2200009. DOI: 10.1002/qute.202200009. URL: https://onlinelibrary.wiley.com/doi/full/10.1002/qute.202200009.

[58] Toan Trong Tran et al. "Resonant excitation of quantum emitters in hexagonal boron nitride". In: *Acs Photonics* 5.2 (2018), pp. 295–300. DOI: 10.1021/acsphotonics.7b00977. URL: https://pubs.acs.org/doi/10.1021/acsphotonics.7b00977.

[59] Andreas Dietrich et al. "Solid-state single photon source with Fourier transform limited lines at room temperature". In: *Physical Review B* 101.8 (2020), p. 081401. DOI: 10.1103/PhysRevB.101.081401. URL: https://link.aps.org/doi/10.1103/PhysRevB.101.081401.

[60] Andreas Gottscholl et al. "Initialization and read-out of intrinsic spin defects in a van der Waals crystal at room temperature". In: *Nature Materials* 19.5 (May 2020), pp. 540–545. ISSN: 1476-1122. DOI: 10.1038/s41563-020-0619-6. URL: https://www.nature.com/articles/s41563-020-0619-6.

[61] AJ Healey et al. "Quantum microscopy with van der Waals heterostructures". In: *Nature Physics* 19.1 (2023), pp. 87–91. DOI: 10.1038/s41567-022-01815-5. URL: https://www.nature.com/articles/s41567-022-01815-5.

[62] Mengqi Huang et al. "Wide field imaging of van der Waals ferromagnet Fe3GeTe2 by spin defects in hexagonal boron nitride". In: *Nature communications* 13.1 (2022), p. 5369. DOI: 10.1038/s41467-022-33016-2. URL: https://www.nature.com/articles/s41467-022-33016-2.

[63] Xiaodan Lyu et al. "Strain quantum sensing with spin defects in hexagonal boron nitride". In: *Nano Letters* 22.16 (2022), pp. 6553–6559. DOI: 10.1021/acs.nanolett.2c01722. URL: https://pubs.acs.org/doi/10.1021/acs.nanolett.2c01722.

[64] Ruotian Gong et al. "Coherent dynamics of strongly interacting electronic spin defects in hexagonal boron nitride". In: *Nature Communications* 14.1 (2023), p. 3299. DOI: 10.1038/s41467-023-39115-y. URL: https://www.nature.com/articles/s41467-023-39115-y.

[65] Fadis F Murzakhanov et al. "Electron–nuclear coherent coupling and nuclear spin readout through optically polarized VB- spin states in hBN". In: *Nano Letters* 22.7 (2022), pp. 2718–2724. DOI: 10.1021/acs.nanolett.1c04610. URL: https://pubs.acs.org/doi/10.1021/acs.nanolett.1c04610.

[66] Roberto Rizzato et al. "Extending the coherence of spin defects in hBN enables advanced qubit control and quantum sensing". In: *Nature Communications* 14.1 (2023), p. 5089. DOI: 10.1038/s41467-023-40473-w. URL: https://www.nature.com/articles/s41467-023-40473-w.

[67] Andrew J Ramsay et al. "Coherence protection of spin qubits in hexagonal boron nitride". In: *Nature Communications* 14.1 (2023), p. 461. DOI: 10.1038/s41467-023-36196-7. URL: https://www.nature.com/articles/s41467-023-36196-7.

[68] Andreas Gottscholl et al. "Spin defects in hBN as promising temperature, pressure and magnetic field quantum sensors". In: *Nature communications* 12.1 (2021), p. 4480. DOI: 10.1038/s41467-021-24725-1. URL: https://www.nature.com/articles/s41467-021-24725-1.

[69] Andreas Gottscholl et al. "Spin defects in hBN as promising temperature, pressure and magnetic field quantum sensors". In: *Nature Communications* 12.1 (July 2021), p. 4480. ISSN: 2041-1723. DOI: 10.1038/s41467-021-24725-1. URL: https://www.nature.com/articles/s41467-021-24725-1.

[70] Nathan Chejanovsky et al. "Single-spin resonance in a van der Waals embedded paramagnetic defect". In: *Nature materials* 20.8 (2021), pp. 1079–1084. DOI: 10.1038/s41563-021-00979-4. URL: https://www.nature.com/articles/s41563-021-00979-4.

[71] Hannah L Stern et al. "Room-temperature optically detected magnetic resonance of single defects in hexagonal boron nitride". In: *Nature communications* 13.1 (2022), p. 618. DOI: 10.1038/s41467-022-28169-z. URL: https://www.nature.com/articles/s41467-022-28169-z.

[72] Nai-Jie Guo et al. "Coherent control of an ultrabright single spin in hexagonal boron nitride at room temperature". In: *Nature Communications* 14.1 (2023), p. 2893. DOI: 10.1038/s41467-023-38672-6. URL: https://www.nature.com/articles/s41467-023-38672-6.

[73] Sam G. Bishop et al. "Room-Temperature Quantum Emitter in Aluminum Nitride". In: *ACS Photonics* 7.7 (July 2020), pp. 1636–1641. ISSN: 2330-4022. DOI: 10.1021/acsphotonics.0c00528. URL: https://pubs.acs.org/doi/10.1021/acsphotonics.0c00528.

[74] Tsung-Ju Lu et al. "Bright High-Purity Quantum Emitters in Aluminum Nitride Integrated Photonics". In: *ACS Photonics* 7.10 (Oct. 2020), pp. 2650–2657. ISSN: 2330-4022. DOI: 10.1021/acsphotonics.0c01259. URL: https://pubs.acs.org/doi/10.1021/acsphotonics.0c01259.

[75] Xiao-Jie Wang et al. "Quantum Emitters with Narrow Band and High Debye–Waller Factor in Aluminum Nitride Written by Femtosecond Laser". In: *Nano Letters* 23.7 (Apr. 2023), pp. 2743–2749. ISSN: 1530-6984. DOI: 10.1021/acs.nanolett.3c00019. URL: https://pubs.acs.org/doi/10.1021/acs.nanolett.3c00019.

[76] Yu Zhou et al. "Room temperature solid-state quantum emitters in the telecom range". In: *Science Advances* 4.3 (Mar. 2018), eaar3580. ISSN: 2375-2548. DOI: 10.1126/sciadv.aar3580. URL: https://www.science.org/doi/10.1126/sciadv.aar3580.

[77] Mehran Kianinia et al. "Resonant excitation of quantum emitters in gallium nitride". In: *Optica* 5.8 (Aug. 2018), p. 932. ISSN: 2334-2536. DOI: 10.1364/OPTICA.5.000932. URL: https://opg.optica.org/abstract.cfm?URI=optica-5-8-932.

[78] Jialun Luo et al. "Room temperature optically detected magnetic resonance of single spins in GaN". In: *Nature Materials* 23.4 (Apr. 2024), pp. 512–518. ISSN: 14764660. DOI: 10.1038/s41563-024-01803-5. URL: https://www.nature.com/articles/s41563-024-01803-5.

[79] Kento Sasaki et al. "Broadband, large-area microwave antenna for optically detected magnetic resonance of nitrogen-vacancy centers in diamond". In: *Review of Scientific Instruments* 87.5 (2016). DOI: 10.1063/1.4952418. URL: https://pubs.aip.org/aip/rsi/article-abstract/87/5/053904/982831/Broadband-large-area-microwave-antenna-for?redirectedFrom=fulltext.

[80] Raj N. Patel et al. "Probing the Optical Dynamics of Quantum Emitters in Hexagonal Boron Nitride". In: *PRX Quantum* 3.3 (Sept. 2022), p. 030331. ISSN: 2691-3399. DOI: 10.1103/PRXQuantum.3.030331. URL: https://link.aps.org/doi/10.1103/PRXQuantum.3.030331.

[81] Shane M. Eaton et al. "Quantum Micro–Nano Devices Fabricated in Diamond by Femtosecond Laser and Ion Irradiation". In: *Advanced Quantum Technologies* 2.5-6 (June 2019). ISSN: 2511-9044. DOI: 10.1002/qute.201900006. URL: https://onlinelibrary.wiley.com/doi/10.1002/qute.201900006.

[82] Rebecca E.K. Fishman et al. "Photon-Emission-Correlation Spectroscopy as an Analytical Tool for Solid-State Quantum Defects". In: *PRX Quantum* 4.1 (Mar. 2023), p. 010202. ISSN: 2691-3399. DOI: 10.1103/PRXQuantum.4.010202. URL: https://link.aps.org/doi/10.1103/PRXQuantum.4.010202.

[83] Lucio Robledo et al. "Spin dynamics in the optical cycle of single nitrogen-vacancy centres in diamond". In: *New Journal of Physics* 13.2 (Feb. 2011), p. 025013. ISSN: 1367-2630. DOI: 10.1088/1367-2630/13/2/025013. URL: https://iopscience.iop.org/article/10.1088/1367-2630/13/2/025013.

[84] Martin Berthel et al. "Photophysics of single nitrogen-vacancy centers in diamond nanocrystals". In: *Physical Review B* 91.3 (Jan. 2015), p. 035308. ISSN: 1098-0121. DOI: 10.1103/PhysRevB.91.035308. URL: https://link.aps.org/doi/10.1103/PhysRevB.91.035308.

[85] Emilie Bourgeois et al. "Photoelectric detection of electron spin resonance of nitrogen-vacancy centres in diamond". In: *Nature Communications* 6.1 (2015), p. 8577. DOI: 10.1038/ncomms9577. URL: https://www.nature.com/articles/ncomms9577.

[86] Lucio Robledo et al. "High-fidelity projective read-out of a solid-state spin quantum register". In: *Nature* 477 (2011), p. 574. DOI: 10.1038/nature10401. URL: https://www.nature.com/articles/nature10401.

[87] Brendan J Shields et al. "Efficient readout of a single spin state in diamond via spin-to-charge conversion". In: *Physical review letters* 114.13 (2015), p. 136402. DOI: 10.1103/PhysRevLett.114.136402. URL: https://link.aps.org/doi/10.1103/PhysRevLett.114.136402.

[88] Dominik M Irber et al. "Robust all-optical single-shot readout of nitrogen-vacancy centers in diamond". In: *Nature Communications* 12.1 (2021), p. 532. DOI: 10.1038/s41467-020-20755-3. URL: https://www.nature.com/articles/s41467-020-20755-3.

[89] Qi Zhang et al. "High-fidelity single-shot readout of single electron spin in diamond with spin-to-charge conversion". In: *Nature communications* 12.1 (2021), p. 1529. DOI: 10.1038/s41467-021-21781-5. URL: https://www.nature.com/articles/s41467-021-21781-5.

[90] Fedor Jelezko et al. "Observation of coherent oscillations in a single electron spin". In: *Physical review letters* 92.7 (2004), p. 076401. DOI: 10.1103/PhysRevLett.92.076401. URL: https://link.aps.org/doi/10.1103/PhysRevLett.92.076401.

[91] B. A. Myers, A. Ariyaratne, and A. C. Bleszynski Jayich. "Double-Quantum Spin-Relaxation Limits to Coherence of Near-Surface Nitrogen-Vacancy Centers". In: *Phys. Rev. Lett.* 118 (19 May 2017), p. 197201. DOI: 10.1103/PhysRevLett.118.197201. URL: https://link.aps.org/doi/10.1103/PhysRevLett.118.197201.

[92] E. L. Hahn. "Spin Echoes". In: *Phys. Rev.* 80 (4 Nov. 1950), pp. 580–594. DOI: 10.1103/PhysRev.80.580. URL: https://link.aps.org/doi/10.1103/PhysRev.80.580.

[93] Zhi-Hui Wang et al. "Comparison of dynamical decoupling protocols for a nitrogen-vacancy center in diamond". In: *Phys. Rev. B* 85 (15 Apr. 2012), p. 155204. DOI: 10.1103/PhysRevB.85.155204. URL: https://link.aps.org/doi/10.1103/PhysRevB.85.155204.

[94] Yanzhao Guo et al. "Laser-written waveguide-integrated coherent spins in diamond". In: *APL Photonics* 9.7 (July 2024), p. 076103. ISSN: 2378-0967. DOI: 10.1063/5.0209294. URL: https://doi.org/10.1063/5.0209294.

[95] Gopalakrishnan Balasubramanian et al. "Ultralong spin coherence time in isotopically engineered diamond". In: *Nature Materials* 8.5 (May 2009), pp. 383–387. ISSN: 1476-1122. DOI: 10.1038/nmat2420. URL: https://www.nature.com/articles/nmat2420.

[96] J. P. Hadden et al. "Strongly enhanced photon collection from diamond defect centers under microfabricated integrated solid immersion lenses". In: *Applied Physics Letters* 97.24 (Dec. 2010). ISSN: 00036951. DOI: 10.1063/1.3519847. URL: https://pubs.aip.org/aip/apl/article-abstract/97/24/241901/122654/Strongly-enhanced-photon-collection-from-diamond?redirectedFrom=fulltext.

[97] Thomas M. Babinec et al. "A diamond nanowire single-photon source". In: *Nature Nanotechnology* 5.3 (Mar. 2010), pp. 195–199. ISSN: 1748-3387. DOI: 10.1038/nnano.2010.6. URL: https://www.nature.com/articles/nnano.2010.6.

[98] Tzu-Yung Huang et al. "A monolithic immersion metalens for imaging solid-state quantum emitters". In: *Nature communications* 10.1 (June 2019), p. 2392. ISSN: 2041-1723. DOI: 10.1038/s41467-019-10238-5. URL: https://www.nature.com/articles/s41467-019-10238-5.

[99] D. Le Sage et al. "Efficient photon detection from color centers in a diamond optical waveguide". In: *Physical Review B* 85.12 (Mar. 2012), p. 121202. ISSN: 1098-0121. DOI: 10.1103/PhysRevB.85.121202. URL: https://link.aps.org/doi/10.1103/PhysRevB.85.121202.

[100] Daniel Riedel et al. "Deterministic Enhancement of Coherent Photon Generation from a Nitrogen-Vacancy Center in Ultrapure Diamond". In: *Physical Review X* 7.3 (Sept. 2017), p. 031040. ISSN: 2160-3308. DOI: 10.1103/PhysRevX.7.031040. URL: https://link.aps.org/doi/10.1103/PhysRevX.7.031040.

[101] Yu-Chen Chen et al. "Laser writing of individual nitrogen-vacancy defects in diamond with near-unity yield". In: *Optica* 6.5 (May 2019), p. 662. ISSN: 2334-2536. DOI: 10.1364/OPTICA.6.000662. URL: https://opg.optica.org/abstract.cfm?URI=optica-6-5-662.

[102] Yan Liu et al. "Fabrication of nitrogen vacancy color centers by femtosecond pulse laser illumination". In: *Optics Express* 21.10 (May 2013), p. 12843. ISSN: 10944087. DOI: 10.1364/oe.21.012843. URL: https://opg.optica.org/oe/fulltext.cfm?uri=oe-21-10-12843&id=253698.

[103] Yu-Chen Chen et al. "Laser writing of coherent colour centres in diamond". In: *Nature Photonics* 11.2 (Feb. 2017), pp. 77–80. ISSN: 1749-4885. DOI: 10.1038/nphoton.2016.234. URL: https://www.nature.com/articles/nphoton.2016.234.

[104] Masanori Fujiwara et al. "Creation of NV centers over a millimeter-sized region by intense single-shot ultrashort laser irradiation". In: *APL Photonics* 8.3 (Mar. 2023). ISSN: 23780967. DOI: 10.1063/5.0137093. URL: https://pubs.aip.org/aip/app/article/8/3/036108/2879024/Creation-of-NV-centers-over-a-millimeter-sized.

[105] Viktoria Yurgens et al. "Low-Charge-Noise Nitrogen-Vacancy Centers in Diamond Created Using Laser Writing with a Solid-Immersion Lens". In: *ACS Photonics* 8.6 (June 2021), pp. 1726–1734. ISSN: 2330-4022. DOI: 10.1021/acsphotonics.1c00274. URL: https://pubs.acs.org/doi/10.1021/acsphotonics.1c00274.

[106] Songyan Hou et al. "Localized emission from laser-irradiated defects in 2D hexagonal boron nitride". In: *2D Materials* 5.1 (Oct. 2017), p. 015010. ISSN: 2053-1583. DOI: 10.1088/2053-1583/aa8e61. URL: https://iopscience.iop.org/article/10.1088/2053-1583/aa8e61.

[107] Xingyu Gao et al. "Femtosecond Laser Writing of Spin Defects in Hexagonal Boron Nitride". In: *ACS Photonics* 8.4 (Apr. 2021), pp. 994–1000. ISSN: 2330-4022. DOI: 10.1021/acsphotonics.0c01847. URL: https://pubs.acs.org/doi/10.1021/acsphotonics.0c01847.

[108] Yuan-Ze Yang et al. "Laser Direct Writing of Visible Spin Defects in Hexagonal Boron Nitride for Applications in Spin-Based Technologies". In: *ACS Applied Nano Materials* 6.7 (Apr. 2023), pp. 6407–6414. ISSN: 2574-0970. DOI: 10.1021/acsanm.3c01047. URL: https://pubs.acs.org/doi/10.1021/acsanm.3c01047.

[109] Yu-Chen Chen et al. "Laser Writing of Scalable Single Color Centers in Silicon Carbide". In: *Nano Letters* 19.4 (Apr. 2019), pp. 2377–2383. ISSN: 1530-6984. DOI: 10.1021/acs.nanolett.8b05070. URL: https://pubs.acs.org/doi/10.1021/acs.nanolett.8b05070.

[110] P. S. Salter et al. "Exploring the depth range for three-dimensional laser machining with aberration correction". In: *Optics Express* 22.15 (July 2014), p. 17644. ISSN: 1094-4087. DOI: 10.1364/OE.22.017644. URL: https://opg.optica.org/oe/abstract.cfm?uri=oe-22-15-17644.

[111] J. P. Hadden et al. "Integrated waveguides and deterministically positioned nitrogen vacancy centers in diamond created by femtosecond laser writing". In: *Optics Letters* 43.15 (Aug. 2018), p. 3586. ISSN: 0146-9592. DOI: 10.1364/OL.43.003586. URL: https://opg.optica.org/abstract.cfm?URI=ol-43-15-3586.

[112] Vibhav Bharadwaj et al. "Femtosecond laser written photonic and microfluidic circuits in diamond". In: *JPhys Photonics* 1.2 (Mar. 2019). ISSN: 25157647. DOI: 10.1088/2515-7647/ab0c4e. URL: https://iopscience.iop.org/article/10.1088/2515-7647/ab0c4e.

[113] Belén Sotillo et al. "Diamond photonics platform enabled by femtosecond laser writing". In: *Scientific Reports* 6.1 (Oct. 2016), p. 35566. ISSN: 2045-2322. DOI: 10.1038/srep35566. URL: https://www.nature.com/articles/srep35566.

[114] M. Sahnawaz Alam et al. "Determining strain components in a diamond waveguide from zero-field optically detected magnetic resonance spectra of negatively charged nitrogen-vacancy-center ensembles". In: *Phys. Rev. Appl.* 22 (2 Aug. 2024), p. 024055. DOI: 10.1103/PhysRevApplied.22.024055. URL: https://link.aps.org/doi/10.1103/PhysRevApplied.22.024055.

[115] C. J. Stephen et al. "Deep Three-Dimensional Solid-State Qubit Arrays with Long-Lived Spin Coherence". In: *Physical Review Applied* 12.6 (Dec. 2019), p. 064005. ISSN: 2331-7019. DOI: 10.1103/PhysRevApplied.12.064005. URL: https://link.aps.org/doi/10.1103/PhysRevApplied.12.064005.

[116] Hannah L. Stern et al. "A quantum coherent spin in hexagonal boron nitride at ambient conditions". In: *Nature Materials* (May 2024). ISSN: 1476-1122. DOI: 10.1038/s41563-024-01887-z. URL: https://www.nature.com/articles/s41563-024-01887-z.

[117] Marcelo Davanço et al. "Multiple time scale blinking in InAs quantum dot single-photon sources". In: *Physical Review B* 89.16 (Apr. 2014), p. 161303. ISSN: 1098-0121. DOI: 10.1103/PhysRevB.89.161303. URL: https://link.aps.org/doi/10.1103/PhysRevB.89.161303.

[118] Antoine Hilberer et al. "Enabling quantum sensing under extreme pressure: Nitrogen-vacancy magnetometry up to 130 GPa". In: *Physical Review B* 107.22 (June 2023). ISSN: 24699969. DOI: 10.1103/PhysRevB.107.L220102. URL: https://journals.aps.org/prb/abstract/10.1103/PhysRevB.107.L220102.

[119] Huijie Zheng et al. "Zero-Field Magnetometry Based on Nitrogen-Vacancy Ensembles in Diamond". In: *Physical Review Applied* 11.6 (June 2019). ISSN: 23317019. DOI: 10.1103/PhysRevApplied.11.064068. URL: https://journals.aps.org/prapplied/abstract/10.1103/PhysRevApplied.11.064068.

[120] Ning Wang et al. "Zero-field magnetometry using hyperfine-biased nitrogen-vacancy centers near diamond surfaces". In: *Physical Review Research* 4.1 (Mar. 2022). ISSN: 26431564. DOI: 10.1103/PhysRevResearch.4.013098. URL: https://journals.aps.org/prresearch/abstract/10.1103/PhysRevResearch.4.013098.

[121] A. Dréau et al. "High-resolution spectroscopy of single NV defects coupled with nearby ^{13}C nuclear spins in diamond". In: *Physical Review B - Condensed Matter and Materials Physics* 85.13 (Apr. 2012). ISSN: 10980121. DOI: 10.1103/PhysRevB.85.134107. URL: https://journals.aps.org/prb/abstract/10.1103/PhysRevB.85.134107.

[122] B. Sotillo et al. "Polarized micro-Raman studies of femtosecond laser written stress-induced optical waveguides in diamond". In: *Applied Physics Letters* 112.3 (Jan. 2018), p. 031109. ISSN: 0003-6951. DOI: 10.1063/1.5017108. URL: https://doi.org/10.1063/1.5017108.

[123] GL Van de Stolpe et al. "Mapping a 50-spin-qubit network through correlated sensing". In: *Nature Communications* 15.1 (2024), p. 2006. DOI: https://doi.org/10.1038/s41467-024-46075-4. URL: https://www.nature.com/articles/s41467-024-46075-4.

[124] Zhi Hui Wang and Susumu Takahashi. "Spin decoherence and electron spin bath noise of a nitrogen-vacancy center in diamond". In: *Physical Review B - Condensed Matter and Materials Physics* 87.11 (Mar. 2013). ISSN: 10980121. DOI: 10.1103/PhysRevB.87.115122. URL: https://journals.aps.org/prb/abstract/10.1103/PhysRevB.87.115122.

[125] Gang Qin Liu et al. "Controllable effects of quantum fluctuations on spin free-induction decay at room temperature". In: *Scientific Reports* 2 (2012). ISSN: 20452322. DOI: 10.1038/srep00432. URL: https://www.nature.com/articles/srep00432.

[126] Luozhou Li et al. "Coherent spin control of a nanocavity-enhanced qubit in diamond". In: *Nature Communications* 6 (Jan. 2015). ISSN: 20411723. DOI: 10.1038/ncomms7173. URL: https://www.nature.com/articles/ncomms7173.

[127] Paolo Andrich et al. "Engineered micro- and nanoscale diamonds as mobile probes for high-resolution sensing in fluid". In: *Nano Letters* 14.9 (Sept. 2014), pp. 4959–4964. ISSN: 15306992. DOI: 10.1021/nl501208s. URL: https://pubs.acs.org/doi/10.1021/nl501208s.

[128] Elke Neu et al. "Photonic nano-structures on (111)-oriented diamond". In: *Applied Physics Letters* 104.15 (Apr. 2014). ISSN: 00036951. DOI: 10.1063/1.4871580. URL: https://pubs.aip.org/aip/apl/article/104/15/153108/131159/Photonic-nano-structures-on-111-oriented-diamond.

[129] Lucio Robledo et al. "High-fidelity projective read-out of a solid-state spin quantum register". In: *Nature* 477.7366 (Sept. 2011), pp. 574–578. ISSN: 00280836. DOI: 10.1038/nature10401. URL: https://www.nature.com/articles/nature10401.

[130] A. Jarmola et al. "Temperature- and magnetic-field-dependent longitudinal spin relaxation in nitrogen-vacancy ensembles in diamond". In: *Physical Review Letters* 108.19 (May 2012). ISSN: 00319007. DOI: 10.1103/PhysRevLett.108.197601. URL: https://journals.aps.org/prl/abstract/10.1103/PhysRevLett.108.197601.

[131] P. L. Stanwix et al. "Coherence of nitrogen-vacancy electronic spin ensembles in diamond". In: *Physical Review B* 82.20 (Nov. 2010), p. 201201. ISSN: 1098-0121. DOI: 10.1103/PhysRevB.82.201201. URL: https://link.aps.org/doi/10.1103/PhysRevB.82.201201.

[132] Zhiyuan Zhao et al. "Sub-nanotesla sensitivity at the nanoscale with a single spin". In: *National Science Review* 10.12 (Apr. 2023), nwad100. ISSN: 2095-5138. DOI: 10.1093/nsr/nwad100. eprint: https://academic.oup.com/nsr/article-pdf/10/12/nwad100/52956802/nwad100.pdf. URL: https://doi.org/10.1093/nsr/nwad100.

[133] Yijin Xie et al. "A hybrid magnetometer towards femtotesla sensitivity under ambient conditions". In: *Science Bulletin* 66.2 (2021), pp. 127–132. ISSN: 2095-9273. DOI: https://doi.org/10.1016/j.scib.2020.08.001. URL: https://www.sciencedirect.com/science/article/pii/S2095927320305223.

[134] Ya-Nan Lu et al. "Observing information backflow from controllable non-Markovian multichannels in diamond". In: *Physical Review Letters* 124.21 (2020), p. 210502. DOI: 10.1103/PhysRevLett.124.210502. URL: https://journals.aps.org/prl/abstract/10.1103/PhysRevLett.124.210502.

[135] MV Gurudev Dutt et al. "Quantum register based on individual electronic and nuclear spin qubits in diamond". In: *Science* 316.5829 (2007), pp. 1312–1316. DOI: 10.1126/science.113983. URL: https://www.science.org/doi/full/10.1126/science.1139831?casa_token=mkZNN5VO3z0AAAAA%3A_vut5sBID8hSMYoDg5AQEWKkvSCmuY5bm-cLvpwFdmGVd_EjjEja1CZ5Dl6P-tkPH-PlcRmGTfiBzg.

[136] P. Neumann et al. "Multipartite Entanglement Among Single Spins in Diamond". In: *Science* 320.5881 (2008), pp. 1326–1329. DOI: 10.1126/science.1157233. eprint: https://www.science.org/doi/pdf/10.1126/science.1157233. URL: https://www.science.org/doi/abs/10.1126/science.1157233.

[137] Mohamed H Abobeih et al. "Fault-tolerant operation of a logical qubit in a diamond quantum processor". In: *Nature* 606.7916 (2022), pp. 884–889. DOI: 10.1038/s41586-022-04819-6. URL: https://www.nature.com/articles/s41586-022-04819-6.

[138] Hannah Clevenson et al. "Broadband magnetometry and temperature sensing with a light-trapping diamond waveguide". In: *Nature Physics* 11.5 (May 2015), pp. 393–397. ISSN: 1745-2473. DOI: 10.1038/nphys3291. URL: https://www.nature.com/articles/nphys3291.

[139] Michael Hoese et al. "Integrated Magnetometry Platform with Stackable Waveguide-Assisted Detection Channels for Sensing Arrays". In: *Physical Review Applied* 15.5 (May 2021), p. 054059. ISSN: 2331-7019. DOI: 10.1103/PhysRevApplied.15.054059. URL: https://link.aps.org/doi/10.1103/PhysRevApplied.15.054059.

[140] BJ Maertz et al. "Vector magnetic field microscopy using nitrogen vacancy centers in diamond". In: *Applied Physics Letters* 96.9 (2010). DOI: 10.1063/1.3337096. URL: https://pubs.aip.org/aip/apl/article/96/9/092504/338885/Vector-magnetic-field-microscopy-using-nitrogen.

[141] Timo Weggler et al. "Determination of the three-dimensional magnetic field vector orientation with nitrogen vacany centers in diamond". In: *Nano Letters* 20.5 (2020), pp. 2980–2985. DOI: 10.1021/acs.nanolett.9b04725. URL: https://pubs.acs.org/doi/10.1021/acs.nanolett.9b04725.

[142] Bing Chen et al. "Calibration-free vector magnetometry using nitrogen-vacancy center in diamond integrated with optical vortex beam". In: *Nano Letters* 20.11 (2020), pp. 8267–8272. DOI: 10.1021/acs.nanolett.0c03377. URL: https://pubs.acs.org/doi/10.1021/acs.nanolett.0c03377.

[143] Yanzhao Guo et al. "Emission dynamics of optically driven aluminum nitride quantum emitters". In: *Physical Review B* 110.1 (July 2024), p. 014109. ISSN: 2469-9950. DOI: 10.1103/PhysRevB.110.014109. URL: https://link.aps.org/doi/10.1103/PhysRevB.110.014109.

[144] Igor Aharonovich and Milos Toth. "Quantum emitters in two dimensions". In: *Science* 358.6360 (Oct. 2017), pp. 170–171. ISSN: 0036-8075. DOI: 10.1126/science.aao6951. URL: https://www.science.org/doi/10.1126/science.aao6951.

[145] Mete Atatüre et al. "Material platforms for spin-based photonic quantum technologies". In: *Nature Reviews Materials* 3.5 (Apr. 2018), pp. 38–51. ISSN: 2058-8437. DOI: 10.1038/s41578-018-0008-9. URL: https://www.nature.com/articles/s41578-018-0008-9.

[146] Marcus W. Doherty et al. "The nitrogen-vacancy colour centre in diamond". In: *Physics Reports* 528.1 (July 2013), pp. 1–45. ISSN: 03701573. DOI: 10.1016/j.physrep.2013.02.001. URL: https://linkinghub.elsevier.com/retrieve/pii/S0370157313000562.

[147] Stefania Castelletto and Alberto Boretti. "Silicon carbide color centers for quantum applications". In: *Journal of Physics: Photonics* 2.2 (Apr. 2020), p. 022001. ISSN: 2515-7647. DOI: 10.1088/2515-7647/ab77a2. URL: https://iopscience.iop.org/article/10.1088/2515-7647/ab77a2.

[148] Alexander Senichev et al. "Room-temperature single-photon emitters in silicon nitride". In: *Science Advances* 7.50 (Dec. 2021), p. 627. ISSN: 2375-2548. DOI: 10.1126/sciadv.abj0627. URL: https://www.science.org/doi/10.1126/sciadv.abj0627.

[149] S G Bishop et al. "Evanescent-field assisted photon collection from quantum emitters under a solid immersion lens". In: *New Journal of Physics* 24.10 (Oct. 2022), p. 103027. ISSN: 1367-2630. DOI: 10.1088/1367-2630/ac9697. URL: https://iopscience.iop.org/article/10.1088/1367-2630/ac9697.

[150] Nai-Jie Guo et al. "Coherent control of an ultrabright single spin in hexagonal boron nitride at room temperature". In: *Nature communications* 14.1 (May 2023), p. 2893. ISSN: 2041-1723. DOI: 10.1038/s41467-023-38672-6. URL: https://www.nature.com/articles/s41467-023-38672-6.

[151] A Sajid, Michael J Ford, and Jeffrey R Reimers. "Single-photon emitters in hexagonal boron nitride: a review of progress". In: *Reports on Progress in Physics* 83.4 (Apr. 2020), p. 044501. ISSN: 0034-4885. DOI: 10.1088/1361-6633/ab6310. URL: https://iopscience.iop.org/article/10.1088/1361-6633/ab6310.

[152] Igor Aharonovich, Dirk Englund, and Milos Toth. "Solid-state single-photon emitters". In: *Nature Photonics* 10.10 (Oct. 2016), pp. 631–641. ISSN: 1749-4885. DOI: 10.1038/nphoton.2016.186. URL: https://www.nature.com/articles/nphoton.2016.186.

[153] Hannah L. Stern et al. "Room-temperature optically detected magnetic resonance of single defects in hexagonal boron nitride". In: *Nature Communications* 13.1 (Feb. 2022), p. 618. ISSN: 2041-1723. DOI: 10.1038/s41467-022-28169-z. URL: https://www.nature.com/articles/s41467-022-28169-z.

[154] J. B. Varley, A. Janotti, and C. G. Van de Walle. "Defects in AlN as candidates for solid-state qubits". In: *Physical Review B* 93.16 (Apr. 2016), p. 161201. ISSN: 2469-9950. DOI: 10.1103/PhysRevB.93.161201. URL: https://link.aps.org/doi/10.1103/PhysRevB.93.161201.

[155] Yongzhou Xue et al. "Experimental Optical Properties of Single-Photon Emitters in Aluminum Nitride Films". In: *The Journal of Physical Chemistry C* 125.20 (May 2021), pp. 11043–11047. ISSN: 1932-7447. DOI: 10.1021/acs.jpcc.1c01376. URL: https://pubs.acs.org/doi/10.1021/acs.jpcc.1c01376.

[156] Kyu Young Han et al. "Metastable dark states enable ground state depletion microscopy of nitrogen vacancy centers in diamond with diffraction-unlimited resolution". In: *Nano Letters* 10.8 (Aug. 2010), pp. 3199–3203. ISSN: 15306984. DOI: 10.1021/nl102156m. URL: https://pubs.acs.org/doi/10.1021/nl102156m.

[157] K Y Han et al. "Dark state photophysics of nitrogen–vacancy centres in diamond". In: *New Journal of Physics* 14.12 (Dec. 2012), p. 123002. ISSN: 1367-2630. DOI: 10.1088/1367-2630/14/12/123002. URL: https://iopscience.iop.org/article/10.1088/1367-2630/14/12/123002.

[158] Mehran Kianinia et al. "All-optical control and super-resolution imaging of quantum emitters in layered materials". In: *Nature communications* 9.1 (Feb. 2018), p. 874. ISSN: 2041-1723. DOI: 10.1038/s41467-018-03290-0. URL: https://www.nature.com/articles/s41467-018-03290-0.

[159] Nathan Chejanovsky et al. "Single-spin resonance in a van der Waals embedded paramagnetic defect". In: *Nature Materials* 20.8 (Aug. 2021), pp. 1079–1084. ISSN: 14764660. DOI: 10.1038/s41563-021-00979-4. URL: https://www.nature.com/articles/s41563-021-00979-4.

[160] Alexander L. Efros and David J. Nesbitt. "Origin and control of blinking in quantum dots". In: *Nature Nanotechnology* 11.8 (Aug. 2016), pp. 661–671. ISSN: 1748-3387. DOI: 10.1038/nnano.2016.140. URL: https://www.nature.com/articles/nnano.2016.140.

[161] Pavel Frantsuzov et al. "Universal emission intermittency in quantum dots, nanorods and nanowires". In: *Nature Physics* 4.7 (2008), pp. 519–522. ISSN: 17452481. DOI: 10.1038/nphys1001. URL: https://www.nature.com/articles/nphys1001.

[162] Prince Khatri et al. "Optical Gating of Photoluminescence from Color Centers in Hexagonal Boron Nitride". In: *Nano Letters* 20.6 (June 2020), pp. 4256–4263. ISSN: 1530-6984. DOI: 10.1021/acs.nanolett.0c00751. URL: https://pubs.acs.org/doi/10.1021/acs.nanolett.0c00751.

[163] Raj N. Patel et al. "Room Temperature Dynamics of an Optically Addressable Single Spin in Hexagonal Boron Nitride". In: *Nano Letters* 24.25 (2024). PMID: 38860722, pp. 7623–7628. DOI: 10.1021/acs.nanolett.4c01333. eprint: https://doi.org/10.1021/acs.nanolett.4c01333. URL: https://doi.org/10.1021/acs.nanolett.4c01333.

[164] Luke Hacquebard and Lilian Childress. "Charge-state dynamics during excitation and depletion of the nitrogen-vacancy center in diamond". In: *Physical Review A* 97.6 (June 2018), p. 063408. ISSN: 2469-9926. DOI: 10.1103/PhysRevA.97.063408. URL: https://link.aps.org/doi/10.1103/PhysRevA.97.063408.

[165] D. Wirtitsch et al. "Exploiting ionization dynamics in the nitrogen vacancy center for rapid, high-contrast spin, and charge state initialization". In: *Physical Review Research* 5.1 (Jan. 2023), p. 013014. ISSN: 2643-1564. DOI: 10.1103/PhysRevResearch.5.013014. URL: https://link.aps.org/doi/10.1103/PhysRevResearch.5.013014.

[166] Jiangbo Tian et al. "Review of recent progresses on gallium nitride transistor in power conversion application". In: *International Journal of Sustainable Energy* 39.1 (Jan. 2020), pp. 88–100. ISSN: 1478646X. DOI: 10.1080/14786451.2019.1657866. URL: https://www.tandfonline.com/doi/abs/10.1080/14786451.2019.1657866.

[167] Kevin Matocha, T. Paul Chow, and Ronald J. Gutmann. "High-voltage normally off GaN MOSFETs on sapphire substrates". In: *IEEE Transactions on Electron Devices* 52.1 (Jan. 2005), pp. 6–10. ISSN: 00189383. DOI: 10.1109/TED.2004.841355. URL: https://ieeexplore.ieee.org/abstract/document/1372701.

[168] Steven P. Denbaars et al. "Development of gallium-nitride-based light-emitting diodes (LEDs) and laser diodes for energy-efficient lighting and displays". In: *Acta Materialia* 61.3 (Feb. 2013), pp. 945–951. ISSN: 13596454. DOI: 10.1016/j.actamat.2012.10.042. URL: https://www.sciencedirect.com/science/article/abs/pii/S1359645412007896.

[169] H. Morkoç and S. N. Mohammad. "High-Luminosity Blue and Blue-Green Gallium Nitride Light-Emitting Diodes". In: *Science* 267.5194 (Jan. 1995), pp. 51–55. ISSN: 0036-8075. DOI: 10.1126/science.267.5194.51. URL: https://www.science.org/doi/10.1126/science.267.5194.51.

[170] Hisashi Masui et al. "Nonpolar and Semipolar III-Nitride Light-Emitting Diodes: Achievements and Challenges". In: *IEEE Transactions on Electron Devices* 57.1 (Jan. 2010), pp. 88–100. ISSN: 0018-9383. DOI: 10.1109/TED.2009.2033773. URL: http://ieeexplore.ieee.org/document/5332357/.

[171] X. Chen et al. "High-Quality Ultra-Fine GaN Nanowires Synthesized Via Chemical Vapor Deposition". In: *Advanced Materials* 15.5 (Mar. 2003), pp. 419–421. ISSN: 0935-9648. DOI: 10.1002/adma.200390097. URL: https://onlinelibrary.wiley.com/doi/10.1002/adma.200390097.

[172] Minh Anh Phan Nguyen et al. "Site control of quantum emitters in gallium nitride by polarity". In: *Applied Physics Letters* 118.2 (Jan. 2021), p. 021103. ISSN: 0003-6951. DOI: 10.1063/5.0036293. URL: https://pubs.aip.org/apl/article/118/2/021103/1022478/Site-control-of-quantum-emitters-in-gallium.

[173] Ming-Lun Lee et al. "Light-emitting diodes with surface gallium nitride p–n homojunction structure formed by selective area regrowth". In: *Scientific Reports* 9.1 (Mar. 2019), p. 3243. ISSN: 2045-2322. DOI: 10.1038/s41598-019-40095-7. URL: https://www.nature.com/articles/s41598-019-40095-7.

[174] Stefania Castelletto and Alberto Boretti. "Gallium Nitride Nanomaterials and Color Centers for Quantum Technologies". In: *ACS Applied Nano Materials* 7.6 (Mar. 2024), pp. 5862–5877. ISSN: 2574-0970. DOI: 10.1021/acsanm.3c05304. URL: https://pubs.acs.org/doi/10.1021/acsanm.3c05304.

[175] S. G. Bishop et al. "Enhanced light collection from a gallium nitride color center using a near index-matched solid immersion lens". In: *Applied Physics Letters* 120.11 (Mar. 2022), p. 114001. ISSN: 00036951. DOI: 10.1063/5.0085257. URL: https://pubs.aip.org/aip/apl/article/120/11/114001/2833354/Enhanced-light-collection-from-a-gallium-nitride.

[176] Hideki Matsubara et al. "GaN Photonic-Crystal Surface-Emitting Laser at Blue-Violet Wavelengths". In: *Science* 319.5862 (Jan. 2008), pp. 445–447. ISSN: 0036-8075. DOI: 10.1126/science.1150413. URL: https://www.science.org/doi/10.1126/science.1150413.

[177] Haoran Zhang et al. "Metropolitan quantum key distribution using a GaN-based room-temperature telecommunication single-photon source". In: *arXiv preprint arXiv:2409.18502* (2024). URL: https://arxiv.org/pdf/2409.18502.

[178] Minh Nguyen et al. "Effects of microstructure and growth conditions on quantum emitters in gallium nitride". In: *APL Materials* 7.8 (Aug. 2019), p. 081106. ISSN: 2166-532X. DOI: 10.1063/1.5098794. URL: https://pubs.aip.org/apm/article/7/8/081106/123136/Effects-of-microstructure-and-growth-conditions-on.

[179] Amanuel M. Berhane et al. "Photophysics of GaN single-photon emitters in the visible spectral range". In: *Physical Review B* 97.16 (Apr. 2018), p. 165202. ISSN: 2469-9950. DOI: 10.1103/PhysRevB.97.165202. URL: https://link.aps.org/doi/10.1103/PhysRevB.97.165202.

[180] Hiroshi Harima. "Properties of GaN and related compounds studied by means of Raman scattering". In: *Journal of Physics: Condensed Matter* 14.38 (Sept. 2002), R967. DOI: 10.1088/0953-8984/14/38/201. URL: https://dx.doi.org/10.1088/0953-8984/14/38/201.

[181] Yi Peng et al. "Formation of β-Be_3N_2 nanocrystallites in Be-implanted GaN". In: *Materials Research Express* 8.3 (Mar. 2021), p. 035003. ISSN: 2053-1591. DOI: 10.1088/2053-1591/abea59. URL: https://iopscience.iop.org/article/10.1088/2053-1591/abea59.

[182] Ali W. Elshaari et al. "Hybrid integrated quantum photonic circuits". In: *Nature Photonics* 14.5 (May 2020), pp. 285–298. ISSN: 1749-4885. DOI: 10.1038/s41566-020-0609-x. URL: https://www.nature.com/articles/s41566-020-0609-x.

[183] Umar Saleem et al. "Light emission from localised point defects induced in GaN crystal by a femtosecond-pulsed laser". In: *Opt. Mater. Express* 8.9 (Sept. 2018), pp. 2703–2712. DOI: 10.1364/OME.8.002703. URL: https://opg.optica.org/ome/abstract.cfm?URI=ome-8-9-2703.

[184] Stefania Castelletto et al. "Color Centers Enabled by Direct Femto-Second Laser Writing in Wide Bandgap Semiconductors". In: *Nanomaterials* 11.1 (Dec. 2020), p. 72. ISSN: 2079-4991. DOI: 10.3390/nano11010072. URL: https://www.mdpi.com/2079-4991/11/1/72.

[185] Christian Degen. "Microscopy with single spins". In: *Nature nanotechnology* 3.11 (2008), pp. 643–644. URL: https://www.nature.com/articles/nnano.2008.328.